

Report DTIC HL 90-1

AD-A225 834

THE PHYSICS OF TURBULENT BOUNDARY LAYER STRUCTURES
AND EFFECTS DUE TO MANIPULATION

by

Choon L. Gan and David G. Bogard

The University of Texas at Austin

Austin, Texas 78712

June 1990

Final Report for August 1, 1986 to July 31, 1989

Submitted to

Office of Naval Research
800 North Quincy Street
Arlington, Virginia 22217-5000

DTIC
ELECTE
AUG 28 1990
S B D
Co

DECLASSIFICATION STATEMENT A
Approved for public release
Distribution Unlimited

00 03 21 023

REPORT DOCUMENTATION PAGE				Form Approved OMB No. 0704-0188	
1. REPORT SECURITY CLASSIFICATION Unclassified			1b. RESTRICTIVE MARKINGS		
2. SECURITY CLASSIFICATION AUTHORITY			3. DISTRIBUTION/AVAILABILITY OF REPORT Approved for public release; distribution unlimited		
7d. DECLASSIFICATION/DOWNGRADING SCHEDULE					
4. PERFORMING ORGANIZATION REPORT NUMBER(S) TTCRL 90-1			5. MONITORING ORGANIZATION REPORT NUMBER(S)		
6a. NAME OF PERFORMING ORGANIZATION University of Texas		6b. OFFICE SYMBOL (if applicable)	7a. NAME OF MONITORING ORGANIZATION Office of Naval Research		
6c. ADDRESS (City, State, and ZIP Code) Department of Mechanical Engineering The University of Texas at Austin Austin, Texas 78712-1063			7b. ADDRESS (City, State, and ZIP Code) Fluid Mechanics, Code 1132F Arlington, VA 22217-5000		
8a. NAME OF FUNDING/SPONSORING ORGANIZATION		8b. OFFICE SYMBOL (if applicable)	9. PROCUREMENT INSTRUMENT IDENTIFICATION NUMBER N00014-86-K-0657		
8c. ADDRESS (City, State, and ZIP Code)			10. SOURCE OF FUNDING NUMBERS		
			PROGRAM ELEMENT NO.	PROJECT NO.	TASK NO.
			WORK UNIT ACCESSION NO.		
11. TITLE (Include Security Classification) The Physics of Turbulent Boundary Layer Structures and Effects Due to Manipulation (Unclassified)					
12. PERSONAL AUTHOR(S) Can, Choon Lim and Bogard, David Guy					
13a. TYPE OF REPORT Final		13b. TIME COVERED FROM 860801 TO 890731		14. DATE OF REPORT (Year, Month, Day) 900614	
15. PAGE COUNT 165					
16. SUPPLEMENTARY NOTATION					
17. COSATI CODES			18. SUBJECT TERMS (Continue on reverse if necessary and identify by block number)		
FIELD	GROUP	SUB-GROUP	Scanning laser Doppler velocimeter, bursts, sweeps, vortical structures, conditional sampling.		
19. ABSTRACT (Continue on reverse if necessary and identify by block number) A summary of work conducted on a scanning LDV system, three dimensional mapping of bursts and sweeps, and LEBU effects on ejections and bursts is presented. This is followed by an in depth report on the three dimensional mapping of the burst structure. This study was conducted using an X-film probe to detect the burst and a three-component LDV to map the velocity field. Conditional sampling analysis showed a streamwise vortical structure with the downstream end inclined up from the wall.					
20. DISTRIBUTION/AVAILABILITY OF ABSTRACT <input checked="" type="checkbox"/> UNCLASSIFIED/UNLIMITED <input type="checkbox"/> SAME AS RPT <input type="checkbox"/> DTIC USERS			21. ABSTRACT SECURITY CLASSIFICATION Unclassified		
22a. NAME OF RESPONSIBLE INDIVIDUAL Dr. M.M. Reischman			22b. TELEPHONE (Include Area Code) (202) 626-4406		22c. OFFICE SYMBOL N00014

TABLE OF CONTENTS

LIST OF TABLES	iv
LIST OF FIGURES	v
SUMMARY	xi
CHAPTER 1. INTRODUCTION	1
1.1 Background	1
1.1.1 Streaks	2
1.1.2 Bursts and sweeps	2
1.1.3 Streamwise vortical structures	4
1.2 Significance and objectives of present study	9
CHAPTER 2. EXPERIMENTAL FACILITIES AND PROCEDURES	11
2.1 Water channel facility	11
2.1.1 Flow conditions	15
2.2 Laser Doppler velocimeter system	16
2.3 Hot-film anemometer system	18
2.3.1 uv correlation coefficient from hot-film probe measurements	19
2.3.2 Calibration of hot-film probe	21
2.3.3 Positioning of the probe	22
2.4 Data acquisition and analysis	23
2.4.1 Data acquisition	23
2.4.2 Data analysis	26
2.5 Burst detection	32
2.5.1 Ejection detection	32
2.5.2 Grouping ejections into bursts	33
2.6 Conditional sampling of flow field	36
CHAPTER 3. RESULTS AND DISCUSSION	38
3.1 Verification of standard turbulent boundary layer	38
3.1.1 Mean and rms velocity profiles and parameters	38
3.1.2 Time between ejections and bursts	42
3.2 Conditional sampling results	46
3.2.1 Results in the y-z plane	47

3.2.2 Determination of convection velocity	65
3.2.3 Results in the x-y plane	70
3.2.4 Results in the x-z plane	75
3.3 Results at a higher ejection detection threshold	78
3.4 Conditional sampling with phase alignment at the mapping point	89
3.5 Reynolds number dependence of the size of the vortical structure	101
3.6 Probability distribution of w velocity near the wall	104
CHAPTER 4. CONCLUSIONS	109
4.1 Summary and conclusions	109
4.2 Recommendations for future work	110
APPENDIX A. FIBEROPTIC LDV DEVELOPMENT AND LDV SETUP	112
A.1 Fiberoptic LDV development	112
A.2 LDV setup	113
APPENDIX B. CALIBRATION OF HOT-FILM PROBE	116
B.1 Procedure	116
B.2 Calibration curve and yaw constant	117
B.3 Look-up table calibration method	122
APPENDIX C. DETERMINATION OF MINIMUM LDV DATA RATE	124
APPENDIX D. CHARACTERISTICS OF THE FLOW FIELD AT DIFFERENT CONVECTION VELOCITIES	127
APPENDIX E. UNCERTAINTY ANALYSIS	134
E.1 LDV velocity measurements	135
E.2 Hot-film velocity measurements	136
E.2.1 Bias error from the calibration	136
E.2.2 Uncertainty in U and V due to uncertainty of k	137
E.3 Ensemble averaged conditional samples	139
NOMENCLATURE	143
REFERENCES	145

INDEX OF REPORTS	149
INDEX OF PUBLICATIONS	149
DISTRIBUTION LIST	150

Accession For	
NTIS GRA&I	<input checked="checked" type="checkbox"/>
DTIC TAB	<input type="checkbox"/>
Unannounced	<input type="checkbox"/>
Justification _____	
By _____	
Distribution/ _____	
Availability Codes	
Dist	Avail and/or Special
A-1	



LIST OF TABLES

E.1	Peak values of u , v , w and uv signals for different ensemble averaged conditional sample sizes.	142
-----	---	-----

LIST OF FIGURES

1.1	Model of the counter-rotating vortices and the low speed streak. Figure from Blackwelder & Kaplan (1979).	5
1.2	Reynolds number dependence of the size of the vortical structure. Taken from Guezennec et al. (1987).	8
2.1	Schematic of water channel facility.	12
2.2	Schematic of upstream stilling tank.	14
2.3	Schematic of downstream stilling tank.	14
2.4	Position of measuring probes.	17
2.5	Variation of uv correlation coefficient with distance from the wall.	20
2.6	Locating the wall with the hot-film probe.	23
2.7	Velocity measurement locations.	24
2.8	Comparison of LDV data before and after bin-averaging.	27
2.9	Comparison of hot-film data before and after bin-averaging.	28
2.10	Comparison of bin-averaged LDV data before and after smoothing.	30
2.11	Comparison between LDV and hot-film velocity signals. The LDV was $5 y^+$ above and $17 x^+$ upstream of the hot-film probe.	31
2.12	Histogram of the distribution of time between ejections for ejections from the same and from different bursts. Figure from Bogard & Tiederman (1986).	34

2.13	Cumulative probability distribution of $T > T_e$. Based on 22804 ejections.	34
2.14	Representative ensemble averaged conditional sample of the flow field phase-aligned with maximum $ (uv)_2 $ at the burst detection point. This location at $y^+ = 35, z^+ = 0$.	37
3.1	Clauser fit to determine the shear velocity, u_τ .	40
3.2	Comparison of skin friction coefficients.	40
3.3	Mean velocity profile normalized with u_τ from Clauser fit.	41
3.4	Comparison of streamwise rms velocity profiles.	43
3.5	Variation of v'/u' with distance from the wall.	44
3.6	Variation of uv correlation coefficient.	44
3.7	Mean times between ejections and bursts.	45
3.8(a)	v-w velocity vectors at $t^+ = -20$.	48
3.8(b)	v-w velocity vectors at $t^+ = -10$.	49
3.8(c)	v-w velocity vectors at $t^+ = -5$.	50
3.8(d)	v-w velocity vectors at $t^+ = -2$.	51
3.8(e)	v-w velocity vectors at $t^+ = 0$	52
3.8(f)	v-w velocity vectors at $t^+ = 5$	53
3.8(g)	v-w velocity vectors at $t^+ = 10$.	54
3.9(a)	U^+ velocity contours at $t^+ = -20$.	56
	vi	

3.9(b)	U^+ velocity contours at $t^+ = -10$.	57
3.9(c)	U^+ velocity contours at $t^+ = -5$.	58
3.9(d)	U^+ velocity contours at $t^+ = -2$.	59
3.9(e)	U^+ velocity contours at $t^+ = 0$.	60
3.9(f)	U^+ velocity contours at $t^+ = 5$.	61
3.9(g)	U^+ velocity contours at $t^+ = 10$.	62
3.10	Time sequence of v-w vectors in the y-z plane.	63
3.11	Time sequence of U^+ contours in the y-z plane.	64
3.12	u velocity contours in the y-z plane at $t^+ = -2$, in increments of 0.4.	66
3.13	v velocity contours in the y-z plane at $t^+ = -2$, in increments of 0.2.	67
3.14	uv product contours in the y-z plane at $t^+ = -2$, in increments of 0.6.	68
3.15	u_c -v vectors in x-y plane at $z^+ = 5$, with a convection velocity of $12 u_\tau$.	71
3.16	u_c -v vectors in x-y plane at $z^+ = 5$, with the local mean as the convection velocity.	73
3.17	U^+ velocity contours in the x-y plane at $z^+ = 5$.	73
3.18	u velocity contours in the x-y plane at $z^+ = 5$, in increments of 0.4.	74

3.19	u velocity contours in the x-y plane of Johansson, Alfredsson & Eckelmann (1987).	74
3.20	Ensemble averaged VISA events of Johansson, Alfredsson & Kim (1987) in the x-y plane. (a) u contours in increments of 0.5. (b) v contours in increments of 0.1.	76
3.21	v velocity contours in the x-y plane at $z^+ = 5$, in increments of 0.2.	77
3.22	uv product contours in the x-y plane at $z^+ = 5$, in increments of 0.6.	77
3.23	u_c -w velocity vectors in x-z plane at (a) $y^+ = 20$ and (b) $y^+ = 35$.	79
3.24	u velocity contours in x-z plane at (a) $y^+ = 20$ and (b) $y^+ = 35$. Contour increments of 0.4.	80
3.25	v velocity contours in x-z plane at (a) $y^+ = 20$ and (b) $y^+ = 35$. Contour increments of 0.2.	81
3.26	Ensemble averaged VISA events of Johansson, Alfredsson & Kim (1987) in the x-z plane at $y^+ = 15$. (a) u contours in increments of 0.5. (b) v contours in increments of 0.1.	82
3.27	v-w velocity vectors at $t^+ = -2$, and at different ejection detection thresholds.	84
3.28	u velocity contours at $t^+ = -2$, and at different ejection detection thresholds. Contour increments of 0.4.	85
3.29	v velocity contours at $t^+ = -2$, and at different ejection detection thresholds. Contour increments of 0.2.	86
3.30	v-w velocity vectors and u velocity contours in the y-z plane at $t^+ = -2$, $H = 4$. Contour increments of 0.4.	87

3.31	uv product contours at $t^+ = -2$, and at different ejection detection thresholds. Contour increments of 0.6.	88
3.32	u velocity contours in the x-y plane at $z^+ = 5$, with $H = 4$, in increments of 0.4.	90
3.33	v velocity contours in the x-y plane at $z^+ = 5$, with $H = 4$, in increments of 0.2.	91
3.34	uv product contours in the x-y plane at $z^+ = 5$, with $H = 4$, in increments of 0.6.	91
3.35	u velocity contours in the x-z plane at (a) $y^+ = 20$, and (b) $y^+ = 35$, with $H = 4$. Contour increments of 0.4.	92
3.36	v velocity contours in the x-z plane at (a) $y^+ = 20$, and (b) $y^+ = 35$, with $H = 4$. Contour increments of 0.2.	93
3.37	Dependence of quadrant detections on window size.	95
3.38(a)	Ensemble averaged conditional samples at $y^+ = 10$, $z^+ = 5$.	96
3.38(b)	Ensemble averaged conditional samples at $y^+ = 35$, $z^+ = 5$.	97
3.38(c)	Ensemble averaged conditional samples at $y^+ = 80$, $z^+ = 5$.	98
3.38(d)	Ensemble averaged conditional samples at $y^+ = 35$, $z^+ = 35$.	99
3.38(e)	Ensemble averaged conditional samples at $y^+ = 35$, $z^+ = 80$.	100
3.39(a)	Quadrant detection in the spanwise direction at $y^+ = 35$.	102
3.39(b)	Quadrant detection in the wall-normal direction at $y^+ = 5$.	102

3.40	Variation of ensemble average displacement thickness as a function of spanwise location.	103
3.41	<i>Reynolds number dependence of vortical structure size.</i>	105
3.42	Distribution of w velocities at $y^+ = 10$ for uncorrelated data.	106
3.43	Distribution of w velocities at $y^+ = 10, z^+ = 35$.	108
3.44	Distribution of w velocities at $y^+ = 20, z^+ = 35$.	108
A.1	Schematic of the fiberoptic LDV.	114
B.1	Typical calibration curve for hot-film sensor.	119
B.2	Calculated velocity at different pitch angles for different yaw constants.	120
B.3	Calculated velocity using yaw constants which give the minimum sum of squared residuals.	120
C.1	Distribution of time between data measurements of LDV.	125
D.1	u_c - v velocity vectors in the x - y plane at $z^+ = 5$ at different convection velocities.	128
D.2	u_c - w velocity vectors in the x - z plane at $y^+ = 20$ at different convection velocities.	130
D.3	u_c - w velocity vectors in the x - z plane at $y^+ = 35$ at different convection velocities.	133
E.1	Errors in U and V due to calibration.	138
E.2	Ensemble averages from (a) 50 samples, (b) 100 samples and (c) 200 samples.	140

SUMMARY

This final report covers work conducted under ONR contract N00014-86-K-0657 over the period from August 1, 1986 to July 31, 1989. The primary objective of this research program was to measure the three dimensional structure of a burst in a turbulent boundary layer. The project also involved development of a scanning LDV system which would measure instantaneous velocity profiles which, in turn, would be used to determine the stage of development of the burst event. Additional objectives were to investigate the sweep structure, and to determine the effect of various drag reduction devices on bursts.

All of these objectives were accomplished to some degree. The scanning LDV system was developed and shown to be successful in measuring instantaneous profiles in the near wall region of a turbulent boundary layer, but the system was not developed in time to be used as the burst detector as originally proposed. Mapping of the three dimensional burst structure was completed using an X-film probe to detect the burst. The sweep structure was investigated using single point X-film probe measurements. The effect of a drag reducing LEBU device on burst and ejection frequency was studied in detail, but the effect of the LEBU device on the three dimensional burst structure was not studied.

Major results from each phase of the project are summarized below. This is followed by a detailed report on the mapping of the three-dimensional burst structure.

Scanning LDV System

Development of the scanning LDV system was co-sponsored by General Dynamics Corporation. Details of the development of scanning LDV system and the operational capabilities of the system are given in previous publications¹ and in a thesis to published in the near future². Previous to the start of the ONR contract, a prototype scanning system had been developed using a rotating mirror system. This system was extensively modified to incorporate an oscillating mirror system driven by a stepper motor. Also, a new signal processing system

¹ Ciancarelli, C. R., M.S. Thesis, Univ. of Texas at Austin, 1988.

Ciancarelli, C. R., Bogard, D. G., and Gan, C. L., AIAA paper 88-0501, 1988.

² Bolton, B. L., M.S. Thesis, Univ. of Texas at Austin, 1990.

was developed as part of the system to allow the Doppler frequency to be measured more precisely which would be necessary when scanning at high velocity.

The primary reason for using a stepper motor to drive the oscillating mirror system was to investigate the possibility of moving the probe volume in discrete steps across the range to be scanned. By having short dwell times (~ 1 msec) at discrete intervals the signal processing precision would be greatly improved. However, the vibration caused by the rapid accelerations and decelerations needed for this mode of operation due to much greater errors than the gain in improved signal processing accuracy. Consequently the scanner was operated with a continuous, constant velocity sweep across the range to be scanned.

Most of the subsequent development time spent on the scanner was to identify sources of vibration and to reduce these vibration levels. Vibration remained the major source of error for the final scanning system, but caused a tolerable 3% uncertainty in the instantaneous velocity measurements. The final scanning system scanned a range of $y^+ = 200$ in 12 msec ($T^+ = 1$) with a time between scans of 37 msec ($T^+ = 3$) and an average of 40 points per scan. With these operational parameters continuous time resolved instantaneous velocity profiles were obtained. The only limitation for the system was that measurements could not be made closer than about $y^+ = 40$ (4 mm) from the wall.

The new signal processing system developed for this phase of the project was based on using a high speed analog-to-digital converter (25 MHz) to digitize the complete Doppler signal. Signal processing programs were then developed that could reduce the Doppler frequency with greater precision than standard counter type processors. The final system was capable of acquiring data at a rate of 1600 samples/sec and had a precision five times better than a counter processor.

Three Dimensional Burst Mapping

Since the remainder of this report is a detailed discussion of the three dimensional burst mapping, only a short summary will be given here. The original goal of this phase of the project was to use the scanning LDV system as a burst detector, a fiber optic LDV probe to detect the center of the burst based on zero spanwise velocity, and a two-component X-film probe to map the three-dimensional structure of the burst. Ultimately the experiment was changed by using the X-

film probe as the burst detector rather than the scanning LDV. The fiber optic LDV, which was designed and constructed as part of the project, was combined with a two-component LDV system to form a three-component LDV system. This allowed mapping the full three component velocity field rather than the two components as originally planned, and was done in order to measure the spanwise velocity of the streamwise vortical structure believed to be associated with the burst.

Transverse and streamwise cross-sections of the burst structure were obtained by mapping a normal-spanwise plane extending to $y^+ = 80$ and $z^+ = 80$. Over 100 Mbytes of data were measured at 48 discrete points. Conditional sampling analysis of this data showed a streamwise vortical structure with the downstream end inclined up from the wall. The three dimensional structure deduced from the conditional sampling analysis was very similar to that found from analysis of numerical simulations.

Sweep Detection and Mapping

In the original proposal, correlations between burst and sweep structures and a three dimensional mapping of the sweep structure was to be done. To accomplish this a velocity data base, similar to the one described above, was measured and a conditional sampling analysis was performed based on sweep detections, using a fourth quadrant detection. Subsequent validation of the data base showed that there were significant errors in the synchronization between the X-film probe and the LDV measurements. A second experiment was performed yielding the data base described in the previous section. Because of time limitations, this second data base was not analyzed based on sweep detection. However, conditional sampling analysis based on burst detection, described above, showed a sweep like structure to the side of the ejecting low speed fluid. Further analysis of the existing data base would provide the three dimensional sweep structure and more detail about the correlation between bursts and sweeps.

Effect of a LEBU Device on Ejections and Bursts

The effect of a LEBU device on ejection and burst frequencies was studied during the early phase of this project and a detailed report and

papers¹ were published previously. The essential results of this study were that the LEBU device clearly reduced the ejection frequency the same amount as the wall shear was reduced. Consequently, the ejection frequency was unchanged when scaled with inner variables. The results also indicated that the burst frequency (not scaled) was reduced very little if at all. Therefore the influence of the LEBU device on the wall structure was in terms of reducing the number of ejections within the burst.

The original goal of the project was to also look at the three dimensional structure of the burst at a position where there was significant drag reduction. This phase of the project was not completed due to time limitations.

¹ Coughran, M. T., Ph.D. Dissertation, Univ. of Texas at Austin, 1988.
Bogard, D. G. and Coughran, M. T., Sixth Symposium on Turbulent Shear Flow, 1987.

CHAPTER 1

INTRODUCTION

1.1 Background

Turbulent boundary layers have been widely studied both experimentally and numerically over the past two to three decades. Since most "real world" flows are turbulent the importance of studying turbulent boundary layers is evident, but because of its complex nature the physics of turbulent boundary layers is still not fully understood. Ongoing research will result not only in a better understanding of the physical nature of turbulence from which improved models can be developed, but also in a better understanding of how to control such flows more effectively.

Measurements by Klebanoff (1955) showed that about 50% of the total turbulence production in a boundary layer occurred in the region very near the wall ($y^+ < 30$), and 80% of the total occurred within $y/\delta = 0.2$. A major portion of this turbulence production in the near wall region has been attributed to identifiable coherent structures and events. Four of the main types of coherent structures are streaks, bursts, sweeps and streamwise vortices.

1.1.1 Streaks

Streaks are longitudinal filaments of low speed fluid which originate in the viscous sublayer (Kline et al., 1967). The streaks have a well documented mean spanwise spacing of 100 viscous wall units ($\lambda^+ = 100$), which is independent of Reynolds number (Smith & Metzler, 1983). Robinson et al. (1988) found that the streaks have a width ranging from 20 to 80 viscous units and have streamwise extents of the order of $x^+ = 1000$. As the streaks move downstream they become unstable and oscillate in both the normal and spanwise directions. Eventually they break up and lift vigorously away from the wall.

1.1.2 Bursts and sweeps

The breakup of streaks and the subsequent 'ejections' of the low speed fluid from the wall have been described as part of the 'bursting' process. A burst consists of one or more ejections from the same streak. Bogard & Tiederman (1987) found that bursts accounted for about 80% of second quadrant uv ($u < 0, v > 0$) production even though the bursts occurred only 32% of the time. Since second quadrant uv ($(uv)_2$) constitutes a significant portion of the Reynolds stress produced in the near-wall region, it is evident that bursts are a key component in turbulence production.

Reynolds stress is also produced when high speed fluid rushes in towards the wall. These sweep events are characterized by having a

high u velocity and a negative v velocity (fourth quadrant uv ; $u > 0$, $v < 0$). Wallace et al. (1972) found that sweeps and bursts each accounted for 70% of the local Reynolds stress. The excess percentage over 100% was due to the other two quadrants. Lu & Willmarth (1973) found that sweeps accounted for 55% of the local Reynolds stress while bursts for 77%. Sweeps then are also a significant contributor to turbulence production.

Although sweeps have been studied in conjunction with bursts by several researchers, the spatial and causal relationships between the two is still not fully understood. In a visual study, Nychas et al. (1973) reported that sweeps occur upstream of ejections. Nagib & Guezennec (1986), using the VITA detection technique, concluded that pairs of burst and sweep events occur in rapid succession. More recently, Komori et al. (1989) used two LDV's to simultaneously detect bursts and map the flow field upstream and downstream of the detection point. Using VITA to detect bursts, they found high speed fluid moving towards the wall upstream of the detection point and the burst event extending downstream. From this they concluded that sweeps occur upstream of bursts. Wark (1988) mapped the flow field in several streamwise and spanwise planes, and using quadrant and shear-stress detection techniques found that sweep and burst events generally occur side by side. Robinson et al. (1988), in their analysis of data from a direct Navier-Stokes numerical simulation, also found that sweeps and bursts generally occur side by side. In an earlier numerical study, Kim

(1985) found that the burst event was surrounded by high speed fluid except at the downstream end.

1.1.3 Streamwise vortical structures

The existence of streamwise vortical structures associated with ejections and bursts in the near-wall region has been reported by several researchers. Bakewell & Lumley (1967), using an eigenfunction decomposition of the streamwise fluctuating velocity data in a pipe flow, inferred the presence of large-scale structures consisting of streamwise counter-rotating eddy pairs. Using electrochemical probes flush-mounted with the wall of a pipe, Lee et al. (1974) obtained fluctuating velocity gradient data in the spanwise and streamwise directions. From space-time correlations they also inferred the presence of counter-rotating eddies with a spanwise wavelength on the order of the mean streak spacing. They found that these eddies were associated with intermittent Reynolds stress production and with the occurrence of large negative values of fluctuating streamwise velocity gradient. These characteristics would be associated with bursts. They also found that the eddies occurred 59% of the time.

Blackwelder & Eckelmann (1979) used a pair of flush-mounted wall sensor probes, separated in the spanwise direction, and hot-film probes to obtain their measurements. Using space-time correlations, they found that the centers of the vortices were $50 z^+$ apart and 20 to 30

y^+ above the wall at a Reynolds number based on channel width of 7700. Figure 1.1 shows a schematic of their proposed model of the vortices and low speed streak. The two vortices, which are represented by vortex lines, exist in a region of a high mean velocity gradient. As a consequence, low speed fluid is trapped between them and is pumped away from the wall, creating the low speed streak.

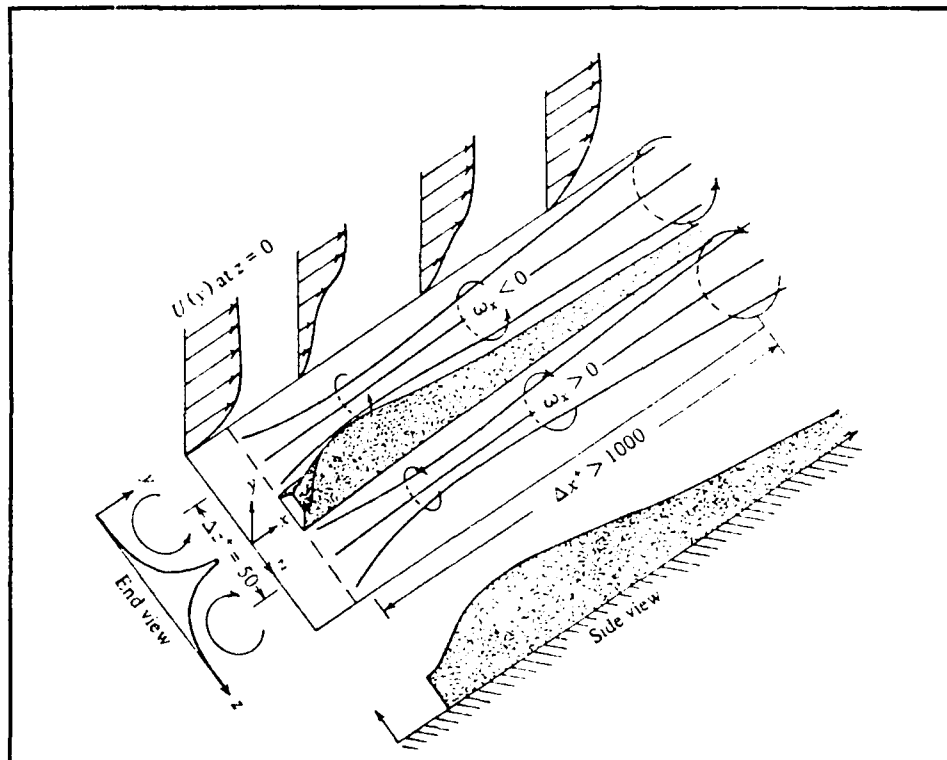


Figure 1.1 Model of the counter-rotating vortices and the low speed streak. Figure from Blackwelder & Eckelmann (1979).

In a study using the same channel facility, Kreplin & Eckelmann (1979) obtained similar results as Blackwelder & Eckelmann. They used space-time correlations of their wall sensor and hot-film sensor measurements, and found that the vortical structures were inclined to the wall at about 5° .

Large-scale rollers with typical spanwise extents of 400 to 600 z^+ were reported by Nagib & Guezennec (1986) and Wark (1988). Their measurements were done in a wind tunnel at a Reynolds number based on momentum thickness (Re_θ) of 4900 to 5200. They used hot-wires and wall shear sensor probes to map the flow field in several streamwise and spanwise planes. The spanwise extent of the vortices in their studies was many times larger than those from the other studies.

Praturi & Brodkey (1978) found streamwise vortices in their stereoscopic visual study. Their study was conducted in water flow at $Re_\theta = 900$ over a flat plate. They reported streamwise vortices with a typical diameter of 50 z^+ and length of 100 x^+ . The axes of these vortices were slightly inclined to the wall and skewed in the spanwise direction. While some of these vortices seemed to be initiated by ejections, most were observed to be the result of the interaction between the high speed flow and low speed flow near the wall.

In another visual study, Smith & Schwartz (1983) reported the presence of pairs of counter-rotating vortices. Using simultaneous top and end view visualization of hydrogen bubbles, they observed an

apparent interdependence of the vortices and low-speed streaks. They observed that the most energetic rotational behavior occurred between $y^+ = 14$ and 25 at Reynolds numbers between 1100 and 1700 based on momentum thickness. In another hydrogen bubble visualization study at a lower Reynolds number ($Re_\theta = 300$) conducted by Kasagi et al. (1986), they also observed counter-rotating vortices, although single vortices were occasionally observed as well. Their vortices had diameters of about $40 z^+$ and were centered at $y^+ = 20$ to 50.

In a large-eddy simulation study conducted by Kim (1985), he showed that there was a pair of counter-rotating vortices in the near-wall region. The distance between centers was between 75 and $120 z^+$ and the distance above the wall was between 25 and $45 y^+$ at a Reynolds number based on channel half-width and centerline velocity of 13800.

Guezennec et al. (1987), using conditional sampling techniques to analyze direct Navier-Stokes simulation data proposed that turbulence producing events were associated with a single dominant vortex rather than a pair of counter-rotating vortices. Suggesting that the counter-rotating vortices were an artifact of ensemble averaging, they applied an asymmetry-preserving averaging scheme to arrive at their result which was at a Reynolds number based on friction velocity and channel half width of 180. They found that the vortical structure had a spanwise extent of about $50 z^+$ and was centered at about $y^+ = 30$. The streamwise extent was over $500 x^+$ and retained its coherence for over $50 t^+$.

To resolve the differences in the size of the vortical structure seen at low Reynolds numbers and at high Reynolds numbers, Guezennec et al. proposed that there was a Reynolds number dependence, as shown in Figure 1.2.

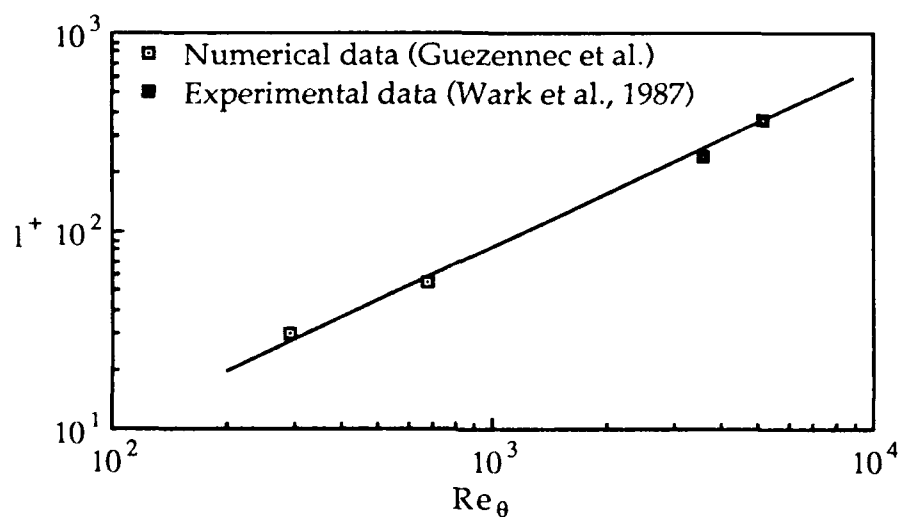


Figure 1.2 Reynolds number dependence of the size of the vortical structure. Figure from Guezennec et al. (1987).

Robinson et al. (1988), using direct Navier-Stokes simulation showed that the streamwise vortices were actually the trailing legs of asymmetric hook-like vortical structures which extend into the outer region of the boundary layer. The legs could be seen without the hook-like neck portion near the wall ($y^+ < 60$) as well as in the wake region.

They noted that true hairpin vortices with two trailing legs were very rare.

1.2 Significance and objectives of present study

Flow visualization studies have shown the existence of both counter-rotating and single vortices in the near-wall region associated with the burst. However, it is difficult to extract much quantitative information from flow visualization studies. Numerical simulations have also shown the association of these vortices with bursts. Most of the experimental studies done so far have only inferred the vortices through space-time correlations. The experimental study that had actually mapped the flow field produced large-scale vortices on the order of the boundary layer thickness. These large-scale vortices are inconsistent with the results from the other studies. A direct experimental measurement of the near-wall vortices has yet to be done.

In this study, a direct mapping was done, in a wall-normal and spanwise plane, of the burst structure and its associated flow field in the near-wall region. While previous studies have measured at most two components of velocity simultaneously, all three velocity components were measured simultaneously in this study. A three-dimensional "picture" of the burst structure and the flow field was

then obtained by using a convection velocity in the streamwise direction.

The primary objectives of the present study were:

- a) To map the burst structure and its associated flow field.
- b) To verify the presence of the near-wall vortical structure.

CHAPTER 2

EXPERIMENTAL FACILITIES AND PROCEDURES

In this chapter, the facilities and equipment used in the experiment are discussed. The procedures for acquiring and analyzing the velocity data are also discussed.

2.1 Water channel facility

The velocity measurements were made in a low speed recirculating water channel facility shown in Figure 2.1. The facility was built and developed by Coughran (1988), and the description that follows is a synopsis of the full description given in his dissertation.

The channel was made of clear acrylic 12.7 mm thick, and consisted of a test section, an upstream stilling tank, and a downstream stilling tank. In addition to the channel, there was a flow circuit consisting of piping, valves and pumps to control the water recirculation, and two 200-gallon water storage tanks.

The test section of the channel was made up of two sections with a combined length of 5 m and was 50 cm wide and 30 cm high. The sidewalls were modified by adding a rib to the top of the sidewalls to

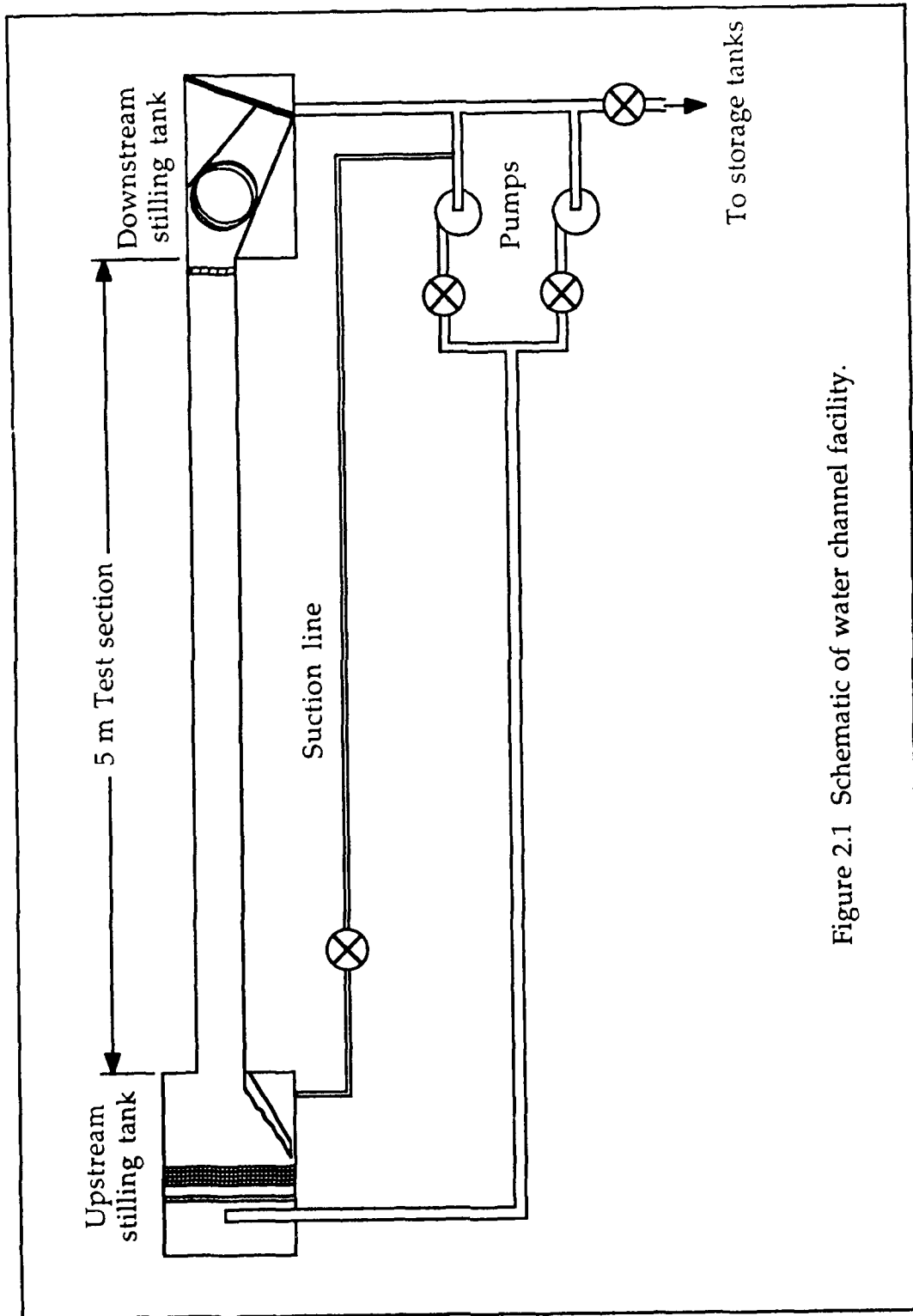
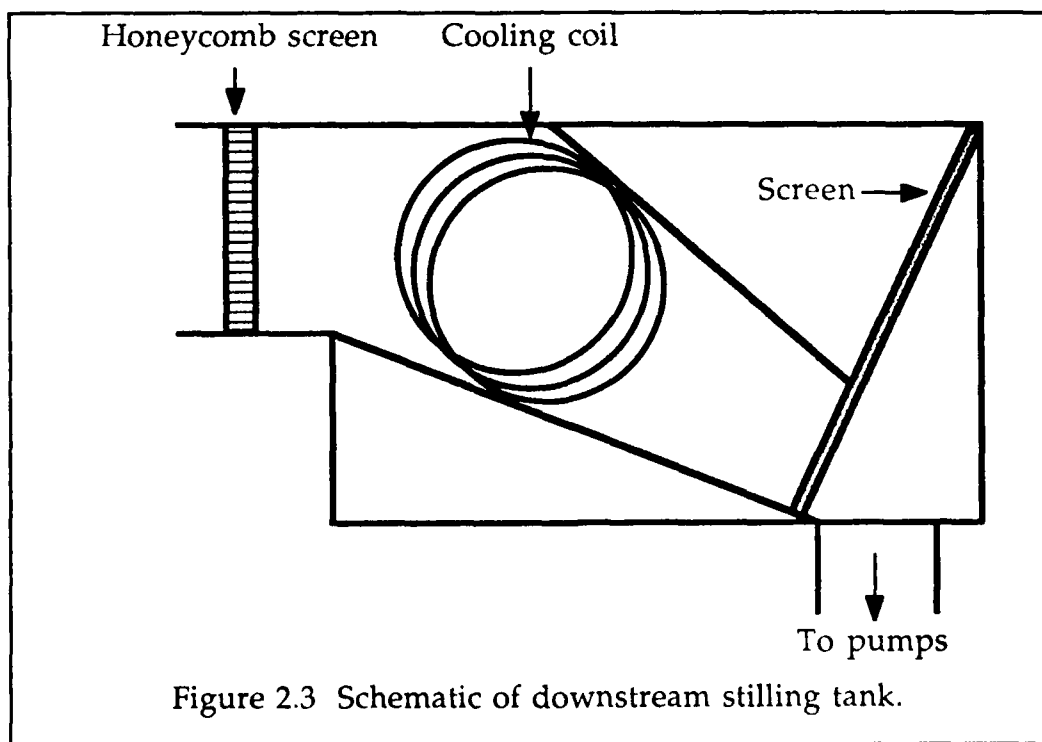
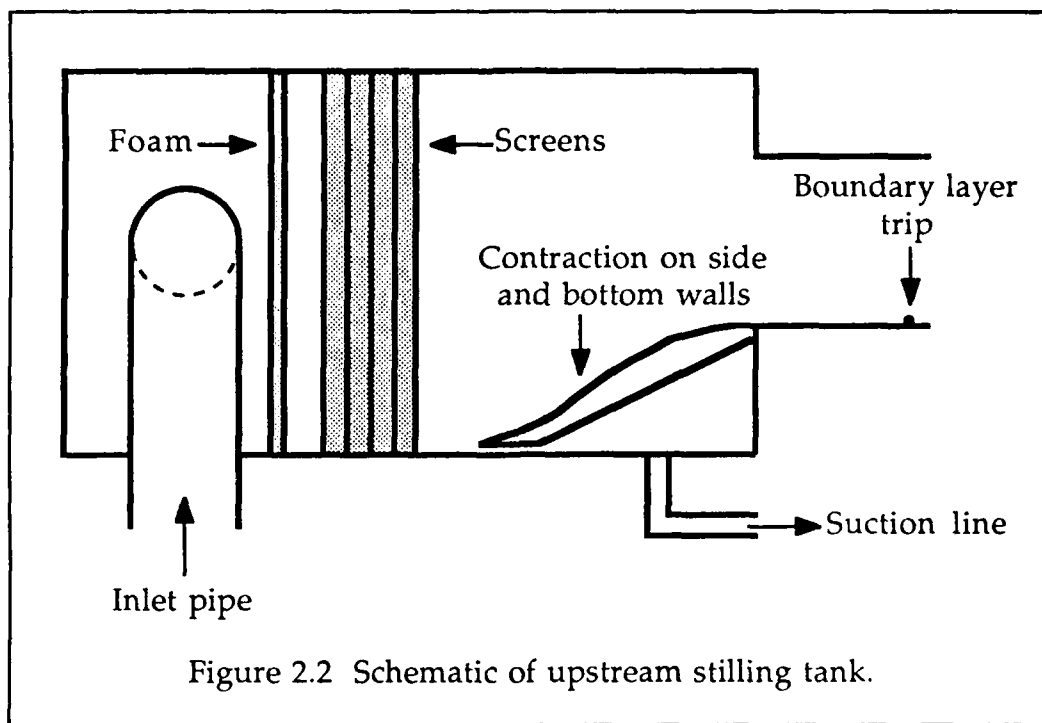


Figure 2.1 Schematic of water channel facility.

stiffen them. A honeycomb section located at the exit was used to dampen disturbances coming from the downstream stilling tank.

Water was fed into the upstream stilling tank by a perforated PVC pipe wrapped with porous foam. This foam was used to dampen any pressure fluctuations and nonuniformities in the flow. A foam sheet covering the entire cross-section of the tank was placed just downstream of the inlet pipe, and was followed by a series of four screens to further dampen the fluctuations and to provide a uniform flow going into the test section, as shown in Figure 2.2. The two upstream screens were of PeCap polyester, mesh size of 33 x 33 per inch with an open area ratio of $\beta = 0.5$. The two downstream screens were vinyl-coated fiberglass insect screen, mesh size of 18 x 16 per inch with $\beta = 0.69$. A 3 to 1 matched cubic contraction was used to guide the flow smoothly into the test section. The bottom of the contraction was raised slightly above the bottom of the tank to create a slot through which suction was applied. This was to further enhance a clean uniform flow going into the test section.

In the downstream stilling tank shown in Figure 2.3, two sloping plates were used to guide the flow smoothly towards the drain. The bottom plate prevented the separation region which would have occurred right after the exit of the test section. A screen was used as a filter to prevent foreign objects getting into the piping. A copper cooling coil in the tank was used to maintain the water temperature in the channel. Cooling was necessary to remove heat added to the water



by the pumps that recirculated the water. By regulating the cooling water flowrate in the coil, the temperature of the water in the channel was maintained to within $\pm 0.05^\circ\text{C}$.

The return piping circuit consisted of 4-inch diameter PVC pipes, valves for controlling the flowrate, and two 2-horsepower centrifugal pumps placed in parallel, producing a flowrate of 450 gpm and a nominal maximum freestream velocity of 0.3 m/s. The two 200-gallon polyethylene tanks were used to store submicron-filtered water. The water was heated to 60°C in the tanks to deaerate it. This was to prevent air coming out of solution on the hot-film sensors during the experiment. Chlorine was also added to the water to retard biological growth.

2.1.1 Flow conditions

The channel was operated with one pump on and with the water at a level of 20 cm. The water level was monitored to ensure that it did not drop because of evaporation and leakages. The freestream velocity in the test section was 18.6 cm/s with a turbulence intensity of about 0.5%. The water temperature was maintained at 21.5°C . At this temperature, the kinematic viscosity of the water was $0.9692 \times 10^{-6} \text{ m}^2/\text{s}$. Reynolds number based on momentum thickness at the measurement location was $Re_\theta = 1530$. The shear velocity was determined by Clauser fit and was $u_\tau = 0.832 \text{ cm/s}$.

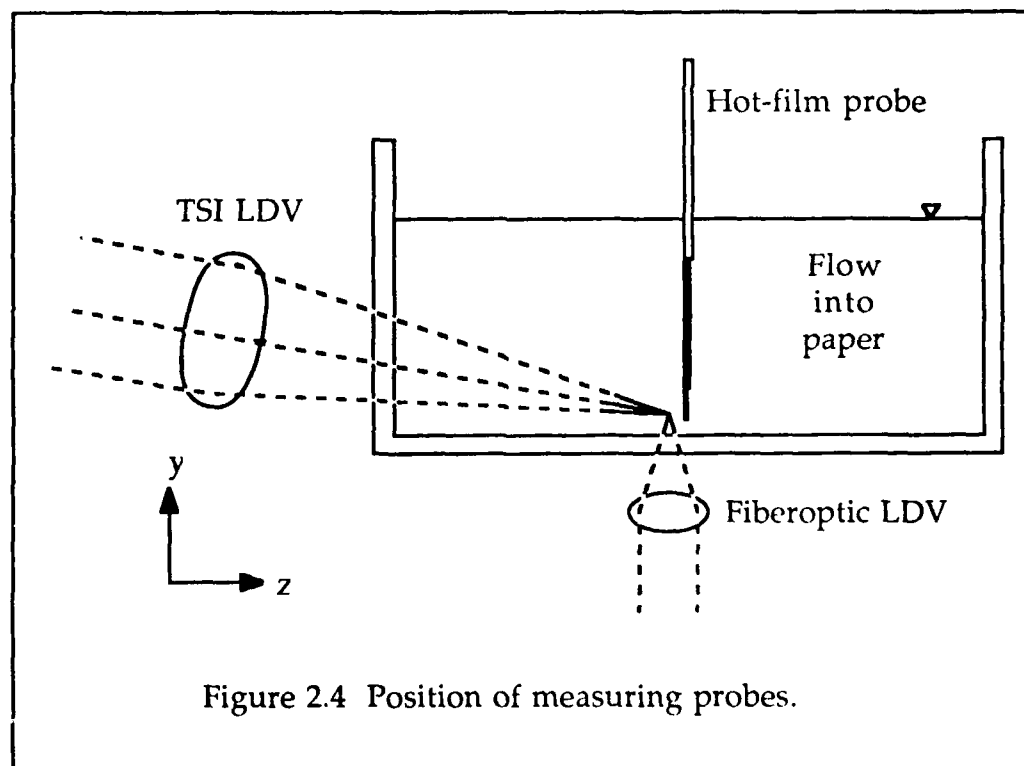
2.2 Laser Doppler velocimeter system

The laser Doppler velocimeter (LDV) system, used to make three-component velocity measurements, actually comprised two independent systems; a TSI 9100-10 system and a fiberoptic system which was constructed by the author.

The TSI 9100-10 LDV was operated as a two-component system. It had a 2 W argon ion laser, frequency shifting optics, and a 3.75X beam expander. Light collection was in the back scatter mode. The signals were processed by TSI model 1990 counter signal processors. Using a 480 mm focal length focusing lens, the size of the probe volume obtained was $70\text{ }\mu\text{m}$ ($d^+ = 0.6$) in diameter and $500\text{ }\mu\text{m}$ ($l^+ \approx 4$) in length. The fringe spacing of the probe volume was determined by direct measurement of the beam angle with an uncertainty of 0.3%. The optics were mounted on a traverse system that had a resolution of $2\text{ }\mu\text{m}$ in the three orthogonal directions.

The fiberoptic LDV was a one-component system that used optical fibers to transmit the laser light to and from the optics. The system had a 2 W argon ion laser and frequency shifting optics. Light collection, signal processing and probe volume dimensions were similar to the TSI system. A traverse system was used to position the optics with a resolution of $1\text{ }\mu\text{m}$ in two orthogonal directions. Details of the development of the fiberoptic system and general LDV setup may be found in Appendix A.

The TSI system was tilted 9° to the vertical so that the probe volume could be placed close to the wall. The system measured the streamwise and wall-normal velocity components (U and V , respectively) from the side of the channel, while the fiberoptic system measured the spanwise component (W) from the bottom of the channel, as shown in Figure 2.4. Because of the tilt, the TSI system was actually measuring the sum of components of V and W 9° to the vertical. The true V component was obtained by subtracting the W component during the data analysis, as discussed in Section 2.4.2.



The position of the probe volumes with respect to the wall were determined by locating the TSI probe volume at the wall by traversing the probe volume until it was visually observed to touch the wall. This procedure for locating the wall was done with a repeatability of better than ± 0.1 mm ($\pm 1 y^+$). Coincidence of the probe volumes of the two systems was determined by collecting signal from the probe volume of one system with the receiving optics of the other system.

The flow was seeded with $1.5 \mu\text{m}$ mean diameter silicon carbide particles. The settling velocity of the seed is 0.2 mm/s. For the flow conditions in this experiment, this seed was small and light enough to follow the smallest scales of motion (Coughran, 1988).

2.3 Hot-film anemometer system

Two-component velocity measurements were made using a TSI 1249-10W subminiature X-type hot-film probe. The sensors were 0.46 mm long and $40 \mu\text{m}$ in diameter ($l^+ \approx 4$ and $d^+ = 0.4$ respectively). The spacing between sensors was 0.6 mm ($z^+ \approx 5$). The probe was mounted to a traverse system which allowed the probe to be traversed normal to the wall with a resolution of 0.1 mm ($y^+ \approx 1$), and in the streamwise and spanwise directions with a resolution of 0.5 mm.

TSI 1050 constant temperature anemometers were used in the non-linear 5:1 bridge output mode with TSI 1056 variable decades connected to the bridges. A bias voltage was applied to the bridge

outputs by TSI 1057 signal conditioners. The resultant outputs were then fed to an Optical Electronics Inc. low-pass filter/amplifier circuit. The filter was set to give a 3 dB roll-off at 200 Hz, and the gain was set at about 3.6 to optimize the signal amplitude going into the Preston Scientific EM313 A/D converter, which had a ± 10 V range and 12-bit resolution. The probe was operated at an overheat ratio of 4% which gave a sensor operating temperature less than the 60°C at which the water was deaerated.

2.3.1 uv correlation coefficient from hot-film probe measurements

The level of the uv correlation coefficient has been well documented as $R_{uv} = -0.45$ across the bulk of a turbulent boundary layer. Thus, the measurement of R_{uv} provides a good check of the accuracy of two-component hot-film measurements.

Coughran (1988) obtained low uv correlation coefficients from his hot-film measurements. In the course of trying to identify and solve this problem, preliminary measurements were made using the same probe Coughran used (model TSI 1248BC-10W), as well as the probe that was used in this experiment (model TSI 1249-10W).

The effect of the proximity of the probe to the wall was investigated first. With either probe, the uv correlation coefficient increased the further away from the wall the probe was, as shown in Figure 2.5. The effect of slight yaw and pitch angles of the probe to the

flow, as well as different overheat ratios were also investigated. In each case, there was no significant effect on R_{uv} .

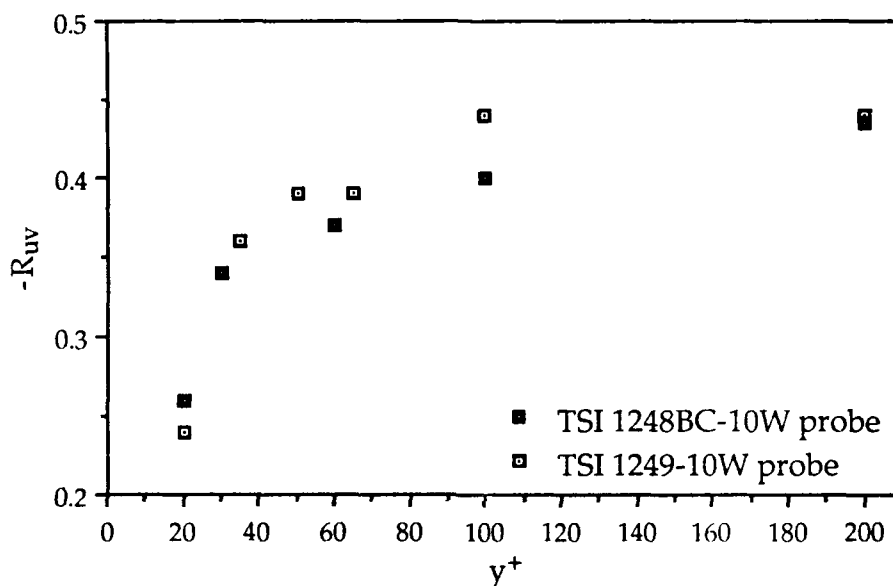


Figure 2.5 Variation of uv correlation coefficient with distance from the wall.

The effect of the calibration method was also investigated. Two different calibration methods were evaluated: the yaw factor method which is similar to the method employed by Coughran, and the look-up table method which was used by Lueptow et al. (1988). In the yaw factor method, a yaw constant k was determined to take into account the inclination of the sensors to the flow direction. In the look-up table

method, a table of sensor voltage pairs and the corresponding velocity/angle pairs was generated for a direct one-to-one conversion.

The two methods did not yield any significant differences in R_{uv} . However, the quality of the calibration regardless of the method used, did effect R_{uv} . Generally, the more precise the calibration, the better was the correlation coefficient across the range of y^+ locations. The yaw factor method was used in this experiment because it was easier and less time consuming to implement. Although the problem has not been fully resolved, Coughran showed that burst detection is not affected by a low R_{uv} .

2.3.2 Calibration of hot-film probe

The probe was calibrated before, once during, and at the end of the experiment. Calibration was performed with the probe in the freestream of the water channel while the freestream velocity was varied over a range that covered the velocities expected to be present in the boundary layer. The probe was also pitched at various angles to the flow at one of the calibration velocities. The range of angles covered those expected to be present in the boundary layer.

Voltage outputs from each sensor of the probe were recorded simultaneously with LDV measurements of the freestream velocity. A calibration curve for each sensor was obtained by fitting a fourth order polynomial relating the square root of the velocity and voltage output

corresponding to that velocity. The curve fits deviated from the calibration velocities by an average 0.4%, but not more than 0.7%. The yaw constant was determined by iteration using the calibration data at the different pitch angles. The yaw constant and calibration constants from the curve fits were then used to convert the sensor voltage pairs to U and V velocities. The calibration procedure is discussed in more detail in Appendix B.

During the experiment, the probe was traversed frequently to the freestream to check for drift in the sensor voltage outputs. The voltages varied less than $\pm 0.4\%$ during the course of the experiment.

2.3.3 Positioning of the probe

The probe position relative to the wall was determined by initially traversing the probe until the probe rested on the wall, as shown in Figure 2.6. At this position, the middle of the sensors was 1.1 mm from the wall. The probe position could then be set to any specified wall-normal location.

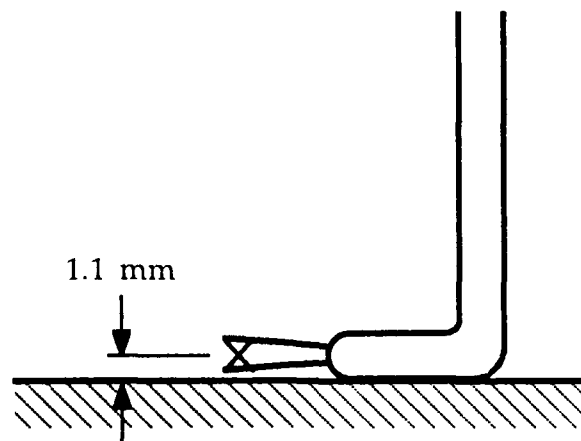


Figure 2.6 Locating the wall with the hot-film probe.

2.4 Data acquisition and analysis

Data were acquired simultaneously from the LDV and hot-film systems with an HP-1000 A700 microcomputer using primarily software that was written by TSI specifically for The University of Texas. Analysis of the data was done on the CDC Dual Cybers mainframe computer using programs which were written and developed by the author.

2.4.1 Data acquisition

Data were taken at 48 locations in a mapping grid that was in the spanwise (z) and wall-normal (y) directions, as shown in Figure 2.7. The range of the grid was from 10 to 80 in the y^+ direction and from 0

to 80 in the z^+ direction. Burst detection was done at $y^+ = 30$ and $z^+ = 5$. The LDV system was used to take coincident three-component velocity data in the grid, while the hot-film anemometer system was used to take two-component data at the burst detection point.

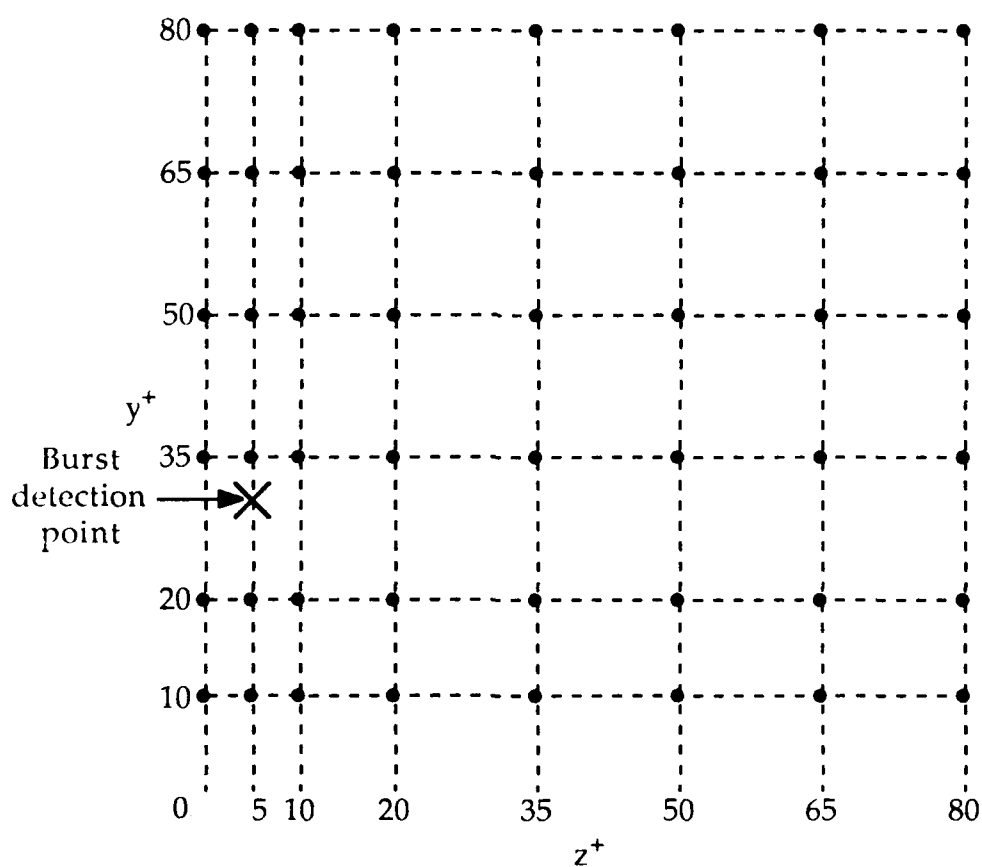


Figure 2.7 Velocity measurement locations.

In positioning the two probes relative to each other, coincidence was determined by placing the LDV probe volume on the sensors of the hot-film probe. This was done by visually observing when the probe volume reflected off of the sensors. Because the sensors are $z^+ \approx 5$ apart and the probe volume length is $l^+ \approx 4$, the uncertainty in positioning the probes relative to each other in the spanwise direction was $z^+ \approx 5$. The results from the conditional sampling, discussed in Chapter 3, indicated that the burst detection point was at $z^+ = 5$ in the grid rather than at $z^+ = 0$.

About 360 seconds ($t^+ \approx 27000$) of data were taken at each location, amounting to a record consisting of about 1.1×10^5 data points for each measurement position. Velocity data from the LDV system were taken at a data rate of about 300 data points per second. The A/D converter was set to sample hot-film data at a rate which approximately matched the data rate of the LDV. This data rate provided an essentially continuous velocity-time history of the flow. At this data rate, an estimated 98% of the times between points was less than $t^+ = 1$. The mean time between points was $t^+ \approx 0.25$ (≈ 3 ms). In comparison, the Kolmogorov time was $\tau^+ \approx 3$ at $y^+ = 10$. The Kolmogorov time was obtained by calculating the turbulence production rate, which is approximately equal to the dissipation rate in the near-wall region. Details of how the minimum acceptable data rate was determined are in Appendix C.

2.4.2 Data analysis

To achieve the data rate of 300 samples/sec a high seed density in the flow was necessary, as well as having to operate the LDV counters at a high gain. Consequently, the LDV signal suffered from noise from the counters (Bogard & Gan, 1987), and from phase noise which results when there are more than one seed particle in the LDV probe volume at a time. To reduce the effects of the noise, the data were processed in two steps:

- 1) Bin-averaging
- 2) Linear three-point smoothing

In the first step, the velocity measurements within a time period of 14 ms ($t^+ = 1$), during which the velocity was essentially constant, were averaged and replaced in the data record with that average. This time window was sequentially applied to the entire data record. Since the errors due to noise were random, averaging the multiple measurements reduced the error by a factor of \sqrt{N} . With a mean data rate of 300/sec, there was an average of four measurements per bin, and thus, the error was reduced by an average of two. Figures 2.8 and 2.9 each show respectively a comparison of an LDV signal and a hot-film signal before and after bin-averaging. As the figures show, the bin-averaging reduced the noise, but still preserved the frequency information of the signals.

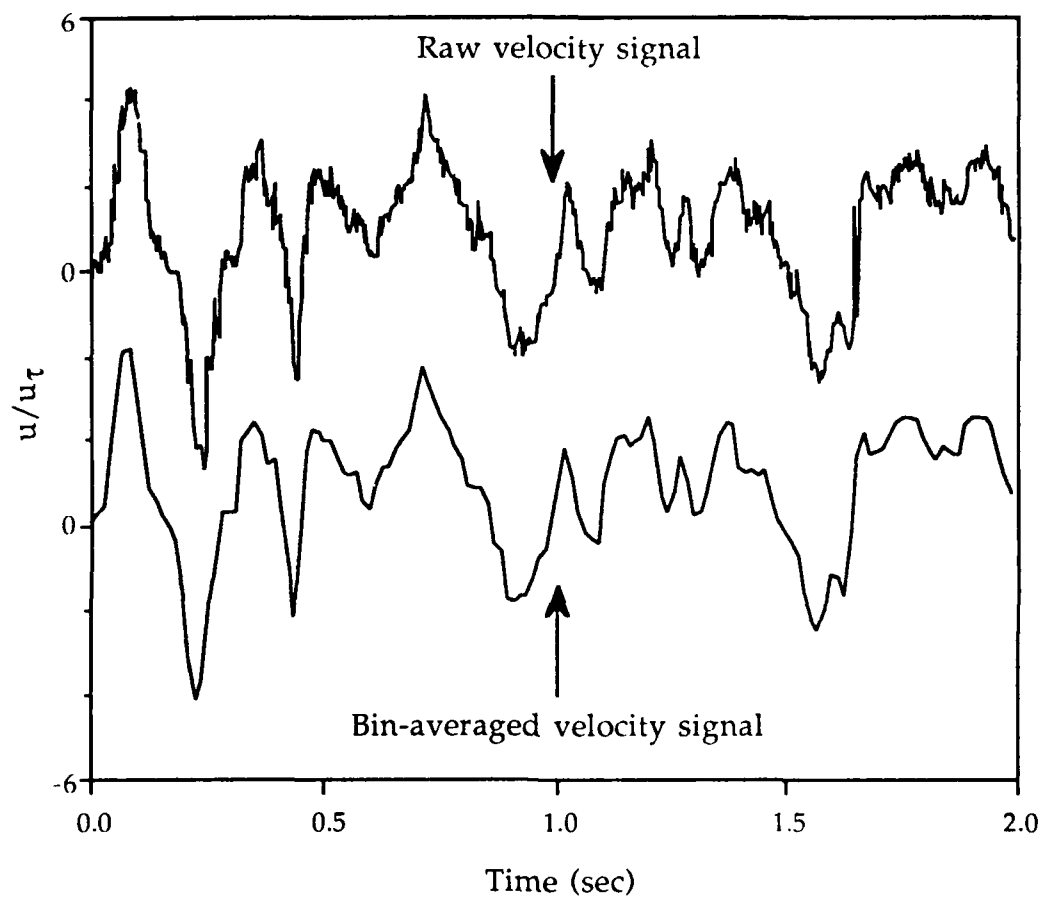


Figure 2.8 Comparison of LDV data before and after bin-averaging.

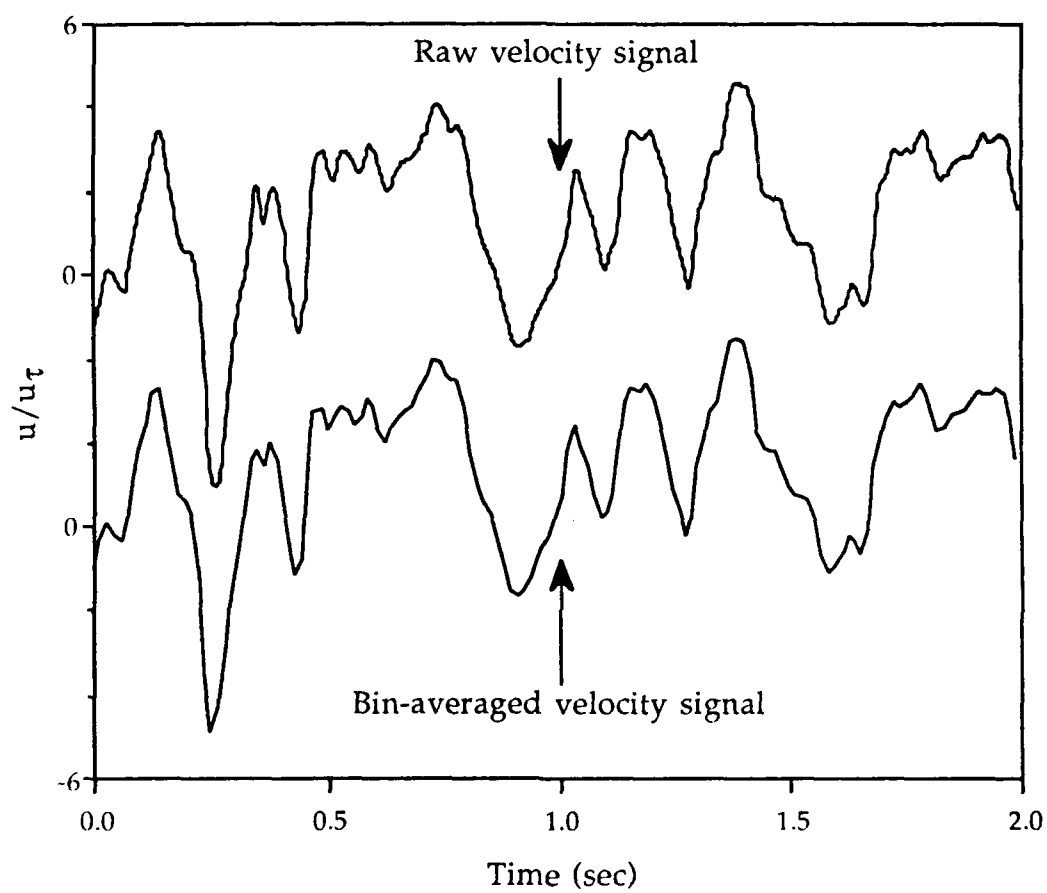


Figure 2.9 Comparison of hot-film data before and after bin-averaging.

In the second step, the data was smoothed by replacing each bin-averaged point with the average of that point and the points before and after it. The smoothing routine was applied to the LDV data only. Smoothing of the hot-film data did not have a significant effect on the data since the data did not suffer from as much noise as the LDV data. Figure 2.10 shows a comparison of the bin-averaged LDV signal before and after smoothing.

After smoothing, the signals from both the LDV and hot-film are very similar. Figure 2.11 shows a comparison between the two. The LDV signal was taken at a position $5 y^+$ above and $17 x^+$ upstream of the hot-film probe so the signals are not expected to be exactly the same.

In addition to smoothing the LDV data, the true V component of velocity had to be resolved from measurements with the LDV system tilted at 9° to the vertical. Based on the measured V component, V_{meas} , and the actual W component, W_{act} , directly measured with the FOLDV, the actual V component was found from the following equation:

$$V_{act} = \frac{V_{meas} - W_{act} \sin 9^\circ}{\cos 9^\circ} \quad (2.1)$$

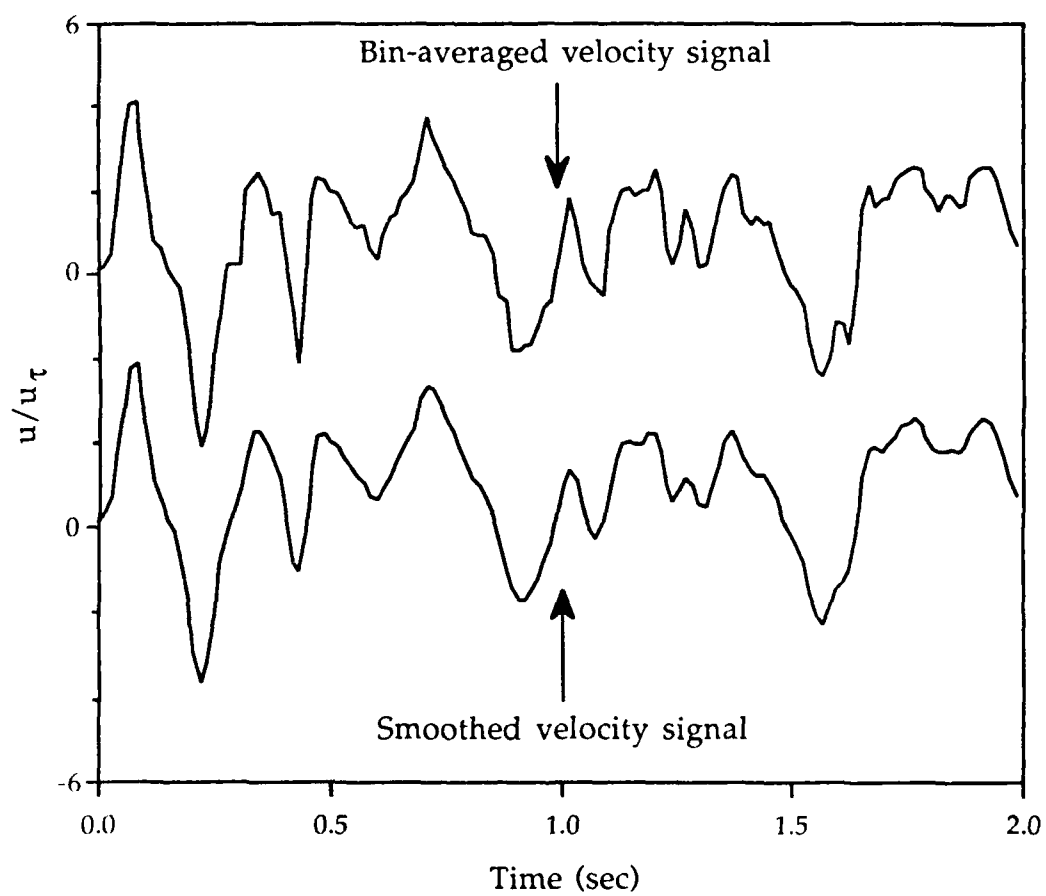


Figure 2.10 Comparison of bin-averaged LDV data before and after smoothing.

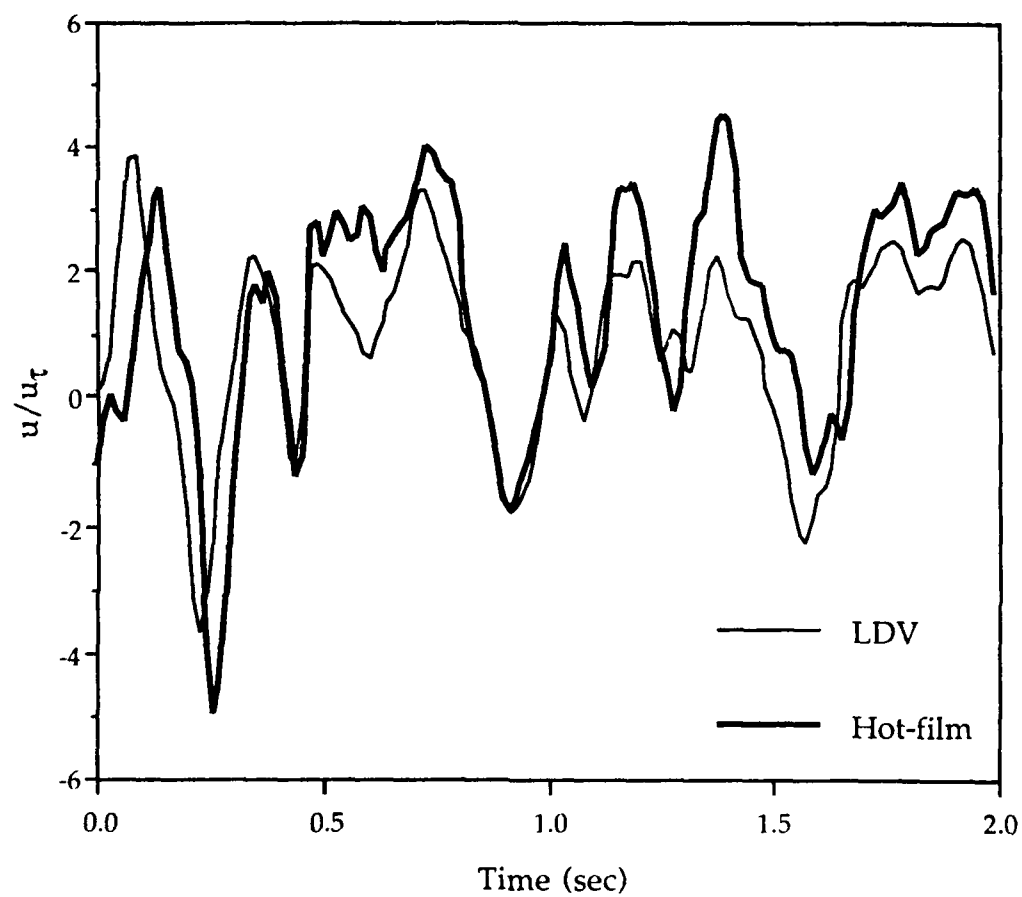


Figure 2.11 Comparison between LDV and hot-film velocity signals. The LDV was $5 y^+$ above and $17 x^+$ upstream of the hot-film probe.

2.5 Burst detection

Burst detection was performed in two parts, firstly by detecting the individual ejections, and secondly grouping the ejections into bursts.

2.5.1 Ejection detection

The Quadrant method was used to detect ejections from the data taken at $y^+ = 30$, $z^+ = 5$. Bogard & Tiederman (1986) determined that this method was the most reliable method for ejection detection in terms of a high percentage of true detections and a low percentage of false detections when compared to visual detections. This method looks at the product of the fluctuating u and v velocity components. Ejections are associated with second quadrant uv , $(uv)_2$ where $u < 0$ and $v > 0$. An ejection is detected whenever the magnitude of the $(uv)_2$ product is greater than a specified value. This value is usually given as $Hu'v'$, where H is the user-specified threshold, u' is the local rms U and v' the local rms V .

The characteristics of ejections such as duration and time between ejections are greatly dependent on the threshold. Comte-Bellot et al. (1978) recommended using the following equation for determining the appropriate threshold:

$$H = \frac{|\bar{u}\bar{v}_2|}{u'v'} \quad (2.2)$$

Using this equation, they found that the threshold was $H \approx 1$ for different types of flows over a wide range of Reynolds numbers. Bogard & Tiederman (1986) also found that the optimum threshold was $H \approx 1$, and gave the best correspondence between detections and visually observed ejections.

Most of the results presented in Chapter 3 were obtained using the mean $(uv)_2$ as the appropriate value of $(uv)_2$ for detecting ejections. This sets the threshold level at $H \approx 1$. Ejection detection was also performed at a higher threshold of $H = 4$. This threshold was recommended by Lu & Willmarth (1973) and is used by many other workers. At this higher threshold only the ejections with the large $(uv)_2$, that is the strong ejections, were detected. Differences, if any, in the characteristics of the flow field between the strong ejections and the weaker ones could then be compared.

2.5.2 Grouping ejections into bursts

Ejections from the same streak may be grouped together into a single burst. Bogard & Tiederman (1986) showed that there were two distinct distributions of time between ejections for ejections from the same burst and from different bursts. This is illustrated in Figure 2.12. A cut-off time, τ_{\max} , represents the maximum time between ejections for grouping into bursts. Thus, ejections separated by times less than τ_{\max} were grouped into the same burst.

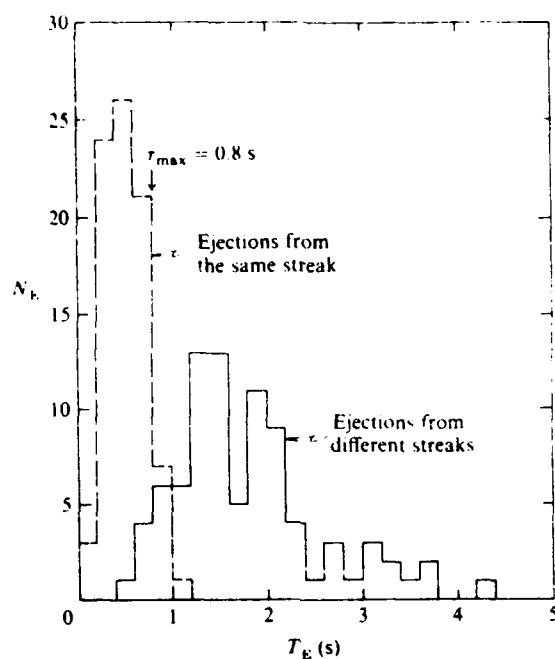


Figure 2.12 Histogram of the distribution of time between ejections for ejections from the same and from different bursts. Figure from Bogard & Tiederman (1986).

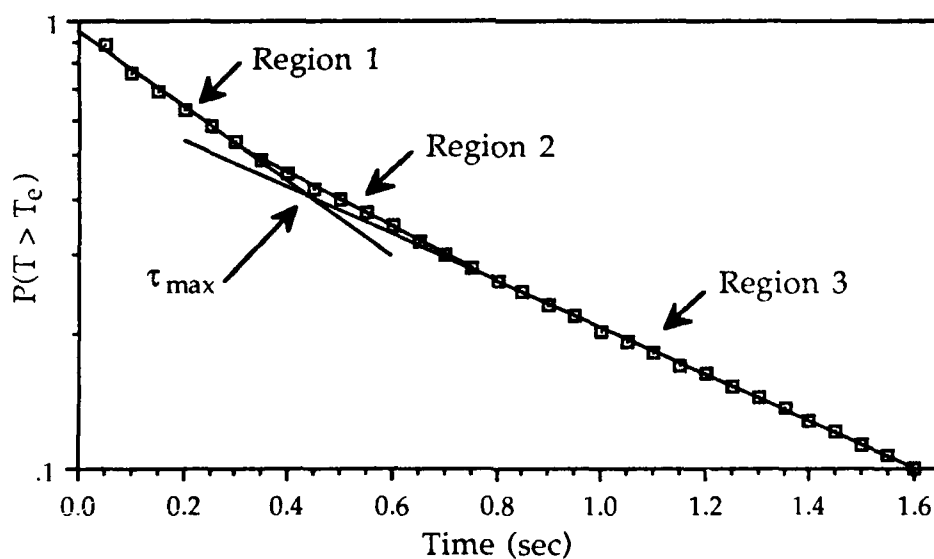


Figure 2.13 Cumulative probability distribution of $T > T_c$. Based on 22804 ejections.

In this study, τ_{\max} was determined by a method introduced by Barlow & Johnston (1985). As shown in Figure 2.13 the cumulative probability of a time greater than a specific time between ejection, $P(T > T_e)$ was plotted in semi-log coordinates against the time between ejections, T_e . Three regions of points with different semi-log linear slopes appear. Regions 1 and 3 are assumed to correspond to the two distributions of time between ejections, region 1 for ejections from the same burst and region 3 for ejections from different bursts. Region 2 represents the overlap region, which is also apparent in Figure 2.12. τ_{\max} lies somewhere within this overlap region. To determine a specific value for τ_{\max} , the lines from regions 1 and 3 were extended until they intersected. τ_{\max} was then taken as the point of intersection. Luchik & Tiederman (1987) used this method on their cumulative probability distribution, which was similar to the one obtained in this study.

The lines in each region were fitted to the data by a least-squares fit. However, as was pointed out by Coughran (1988), there is no definitive way of selecting which points to include at the ends of the regions. The regions were selected by visually looking for the points where there was a definite change in slope. To check the repeatability of this method, τ_{\max} was determined from the cumulative distribution from the entire data set, consisting of 22804 ejections, and from five subsets, consisting of an average of 4560 ejections, of the same data.

τ_{\max} from the entire data set was 0.45 sec, while τ_{\max} from the subsets varied between 0.4 sec to 0.5 sec with a mean of 0.46 sec.

2.6 Conditional sampling of flow field

The signal of the mapping probe was conditionally sampled at each of the measurement locations using the occurrence of bursts at the detection probe as the condition. The conditional sampling was phase-aligned with the maximum magnitude $(uv)_2$ of the detected bursts. The resulting conditionally sampled flow field thus corresponded with the middle of the strongest ejection within the burst. A representative ensemble-averaged conditional sample at one of the measurement locations is shown in Figure 2.14. Conditional sampling was done at both threshold levels.

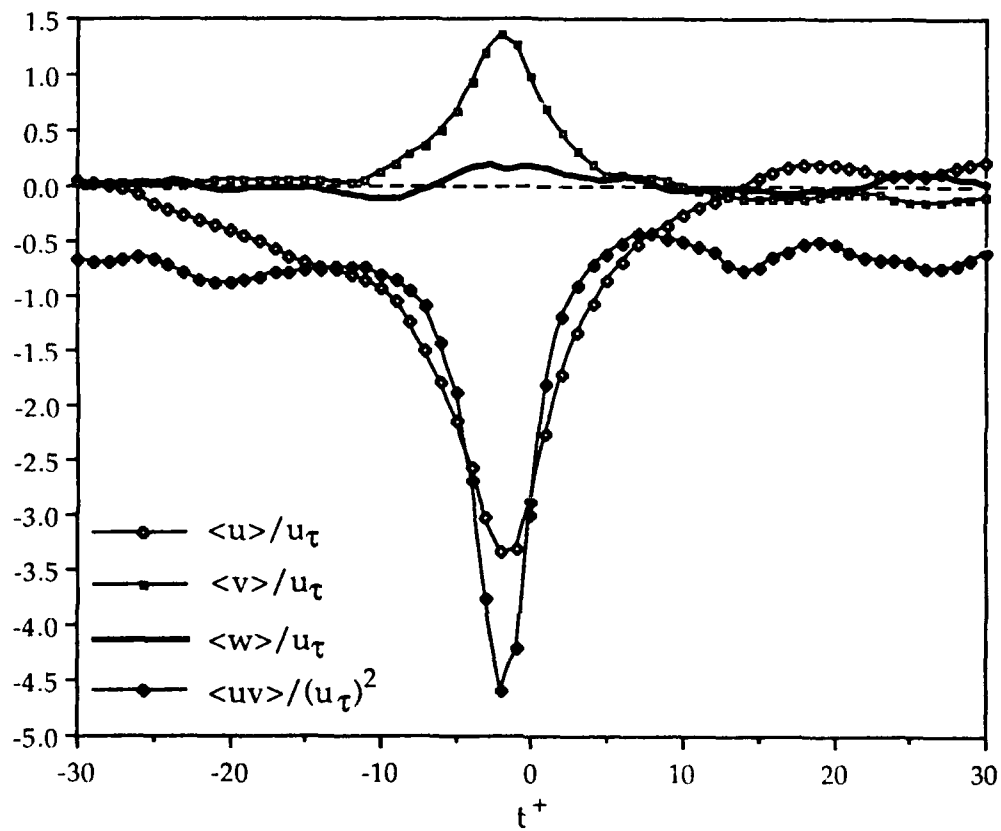


Figure 2.14 Representative ensemble averaged conditional sample of the flow field phase-aligned with maximum $|(uv)_2|$ at the burst detection point. This location at $y^+ = 35, z^+ = 0$.

CHAPTER 3

RESULTS AND DISCUSSION

3.1 Verification of standard turbulent boundary layer

All measurements reported in this thesis were made at a position $x = 3.5$ m downstream of the water channel inlet. The boundary layer was tripped using a 3 mm diameter brass rod positioned on the wall at $x = 0.5$ m. At the measurement location the Reynolds number was $Re_\theta = 1530$.

The existence of a standard turbulent boundary layer in the water channel facility was verified by examining several of the parameters in the boundary layer, including the times between ejections and bursts.

3.1.1 Mean and rms velocity profiles and parameters

The mean velocity profile of the boundary layer was measured at the measurement location prior to taking the conditional sample data. The shear velocity, u_τ , and skin friction coefficient, C_f , were determined by fitting the velocity profile to the law of the wall:

$$\frac{u}{u_\tau} = \frac{1}{\kappa} \ln\left(\frac{yu_\tau}{\nu}\right) + C \quad (3.1)$$

A Clauser fit was done using the procedure employed by Kline et al. (1967). The values of 0.41 for κ and 5.0 for C were used. In the procedure used by Kline et al. u_τ at each y location was determined iteratively using the following relationship:

$$u^+y^+ = \frac{uy}{\nu} = \frac{1}{\kappa}y^+\ln y^+ + Cy^+ \quad (3.2)$$

where $y^+ = \left(\frac{yu_\tau}{\nu}\right)$. The value for u_τ was determined from the log region where u_τ was constant, as shown in Figure 3.1. Having determined u_τ , the skin friction coefficient was obtained from:

$$C_f = 2 \left(\frac{u_\tau}{u_\infty} \right)^2 \quad (3.3)$$

In Figure 3.2, it can be seen that C_f from the Clauser fit agreed well with the data from Coles & Hirst (1969) who also used the same log-law constants. The data point also agreed with the Clauser fit data from Coughran (1988) and Blanton (1986), both of whom used the same channel facility as this experiment.

The mean velocity profile agreed well with the single law of the wall expression of Spalding (1961), as shown in Figure 3.3. However, some deviation was noted close to the wall ($y^+ < 15$). This was probably due to the uncertainty in the wall location. The mean velocity data from the conditional sample database also showed good agreement.

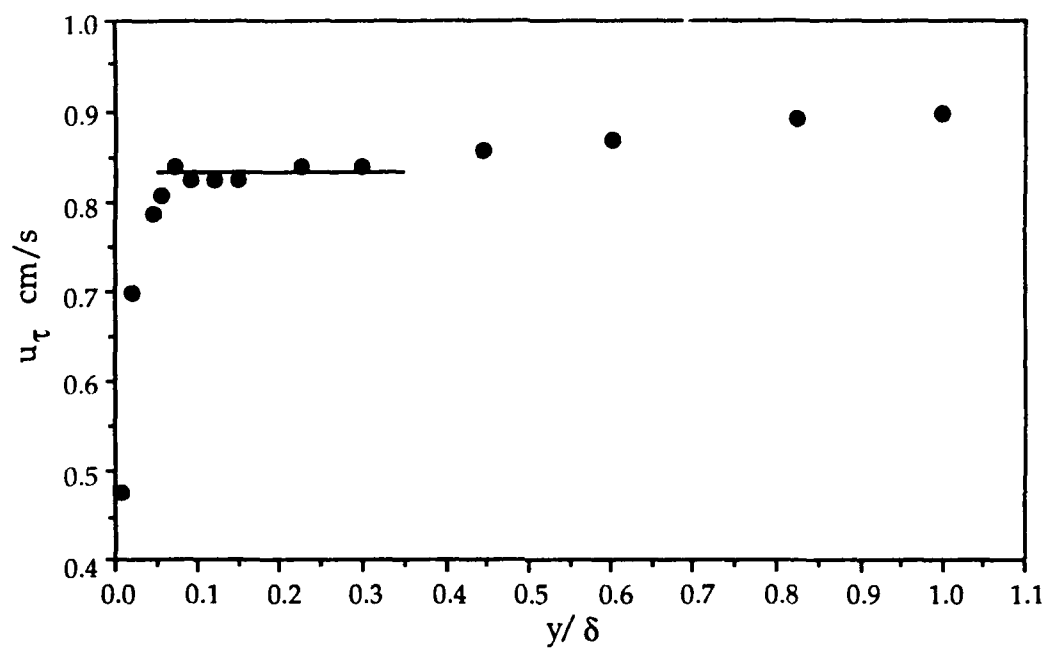


Figure 3.1 Clauser fit to determine the shear velocity, u_τ .

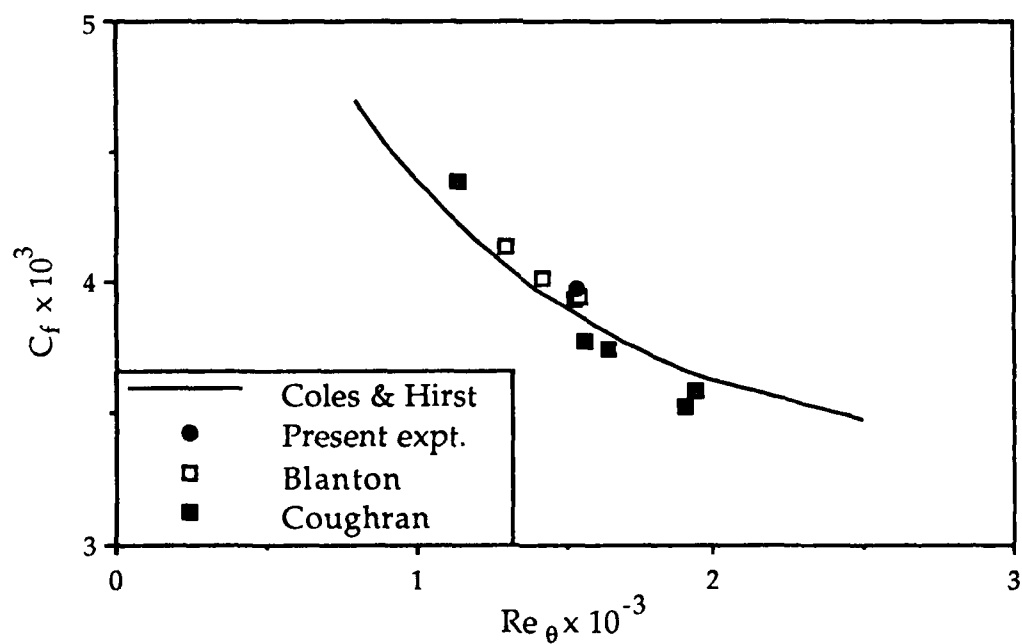


Figure 3.2 Comparison of skin friction coefficients.

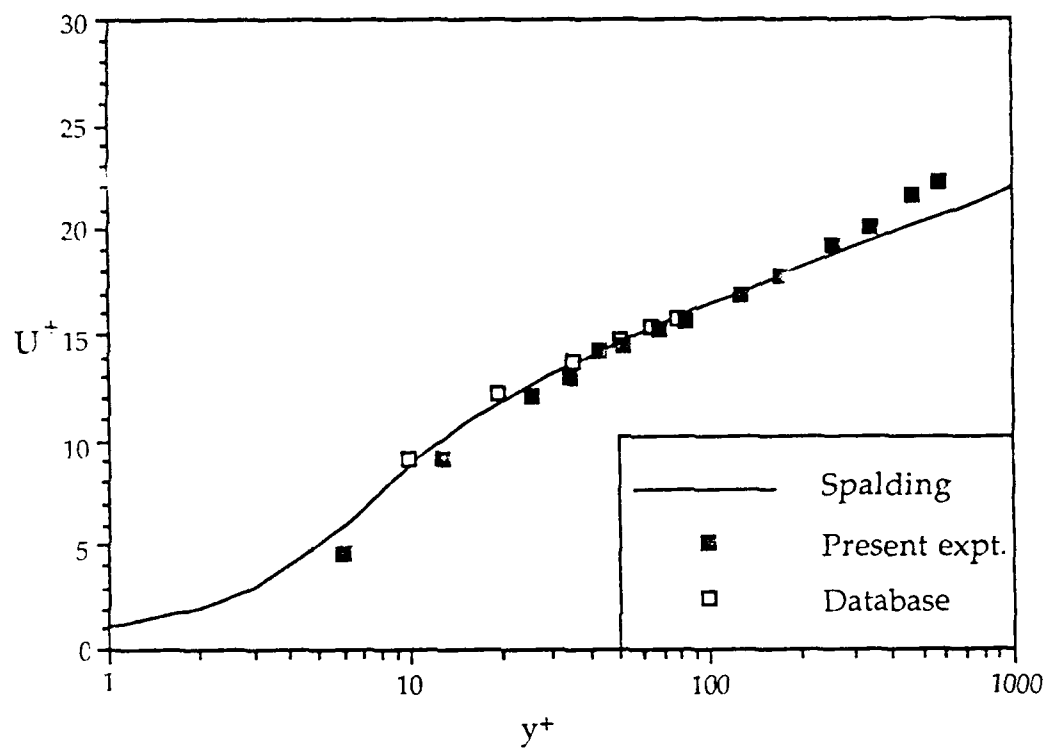


Figure 3.3 Mean velocity profile normalized with u_τ from Clauser fit.

The variation of the streamwise rms velocity, u' , normalized with u_τ is shown in Figure 3.4. The data compared well with data from Purtell et al. (1981) and Blanton (1986) at about the same Re_θ . The data from the database also showed reasonably good agreement. Although the data from the database showed the same trend, the magnitudes were slightly low. Figure 3.5 shows the variation of $\frac{v'}{u'}$ with distance from the wall for data from the database. The data showed good agreement with the expected trend from Barlow & Johnston (1985).

Figure 3.6 shows the uv correlation coefficient, $-R_{uv}$. Except for the hot-film data point, $-R_{uv}$ was in the region of 0.45, which is the expected value. As discussed in Section 2.3.1, Coughran showed that the burst detection from hot-film measurements is not affected by the low $-R_{uv}$.

3.1.2 Time between ejections and bursts

The times between ejections and bursts, normalized with inner variables, are shown in Figure 3.7. The time between ejections, T_e , decreases further away from the wall. This trend can be seen in the data, which falls within the data of Bogard & Tiederman (1986) and Coughran. The T_e at $y^+ = 10$, however, is less than expected.

This low T_e at $y^+ = 10$ is probably due to noise, which results in pseudo events being detected. An increase in the number of events detected will, thus, decrease the time between ejections. Because the

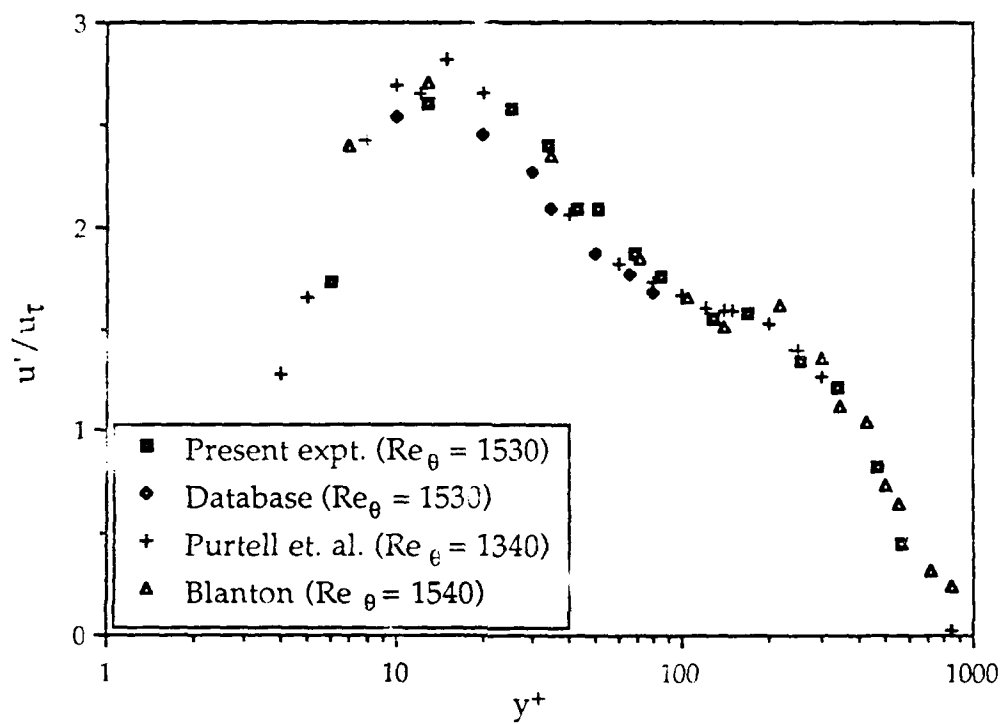


Figure 3.4 Comparison of streamwise rms velocity profiles.

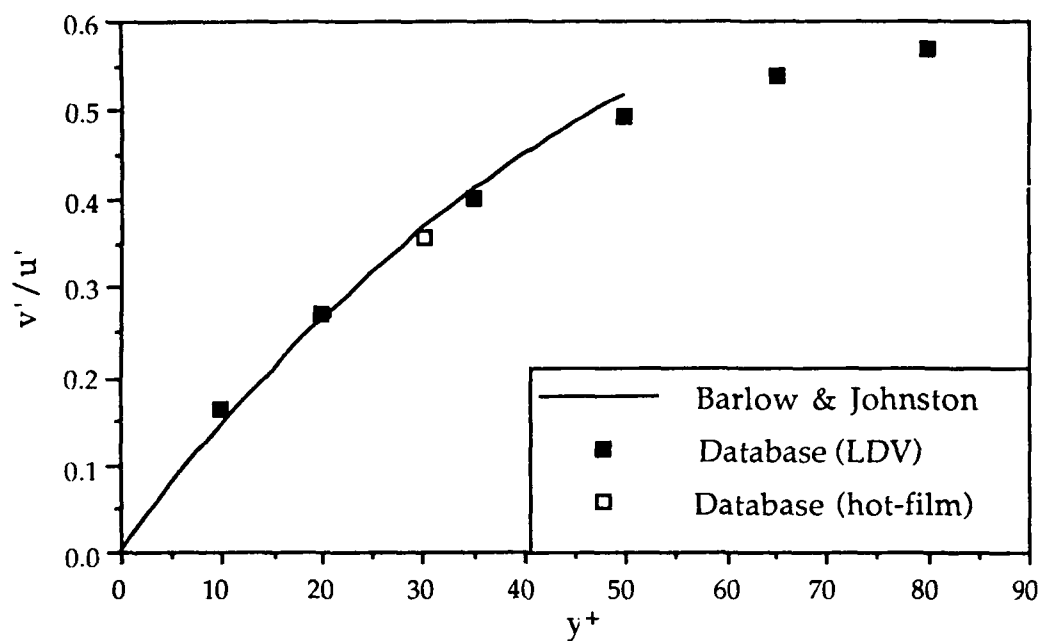


Figure 3.5 Variation of v'/u' with distance from the wall.

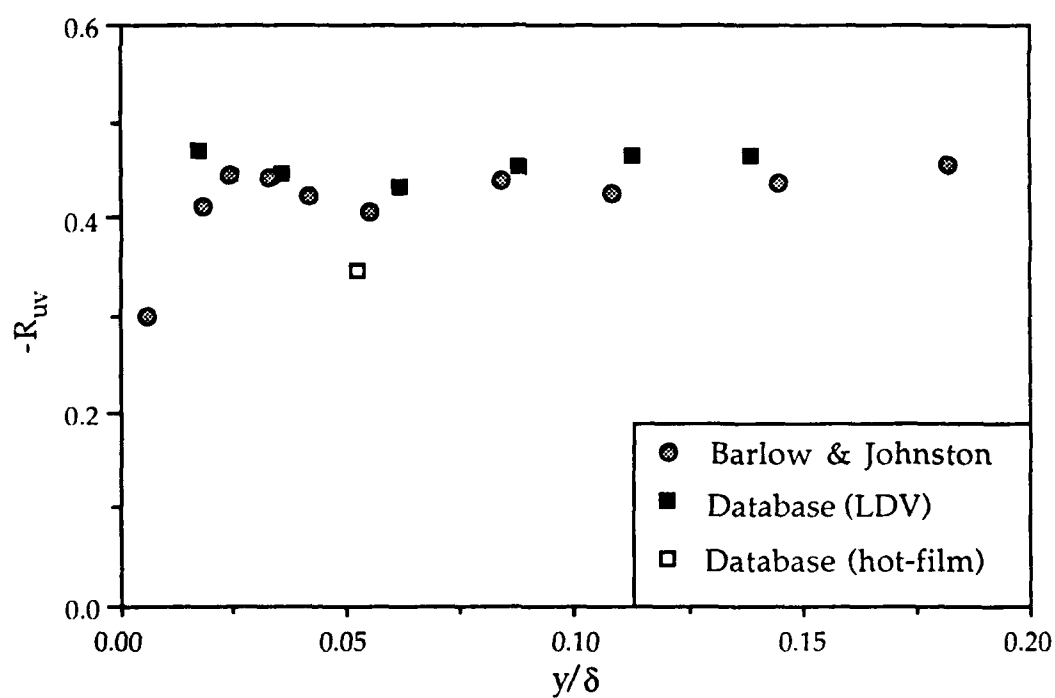


Figure 3.6 Variation of uv correlation coefficient.

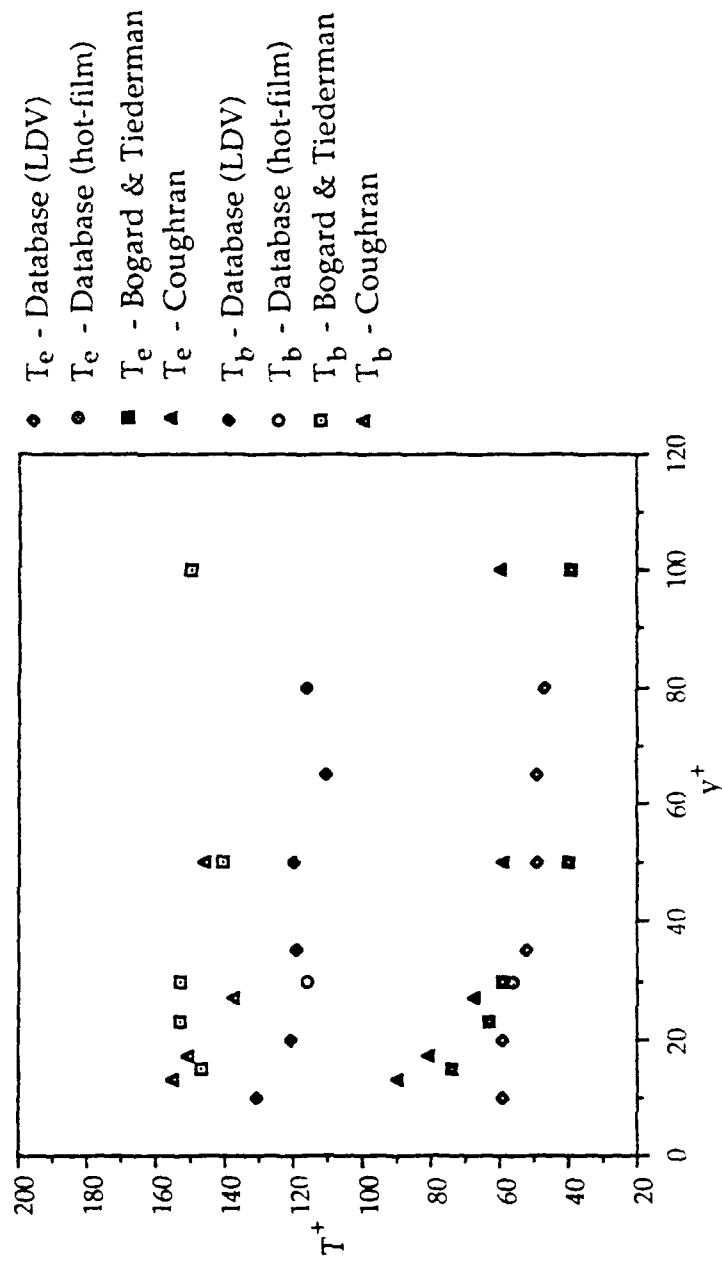


Figure 3.7 Mean times between ejections and bursts.

magnitudes of the v velocity near the wall are less than those further away, any noise in the signal will have a bigger effect on the signal near the wall. This results in a noisier uv signal near the wall than further away. A comparison of the uv signals at $y^+ = 10$ and $y^+ = 20$ indicated that this was the case.

The time between bursts, T_b , was found to be essentially constant, as observed by Bogard & Tiederman.

3.2 Conditional sampling results

The conditionally sampled characteristics of the burst and its associated flow field are presented in this section. Results in the y - z , x - y and x - z planes are presented. As was mentioned in Section 2.6, the conditional samples were phase-aligned with the maximum magnitude $(uv)_2$ within the burst. Bogard & Tiederman (1987) found that within multi-ejection bursts there is one strong ejection which dominates the others, and is usually the first one. This strongest ejection is more distinctive and has larger amplitudes for the u , v and uv signals. Thus, the conditional samples of the flow field were phase-aligned with the strongest ejection within the burst. The conditional samples at each measurement location were based on an average of 200 bursts.

3.2.1 Results in the y-z plane

Figure 3.8(a)-(g) shows the fluctuating v-w velocity vectors normalized with u_τ at different times, from $t^+ = -20$ to $t^+ = 10$. The burst detection is at $t^+ = 0$, but because the mapping grid was upstream of the detector, the grid encountered the event slightly before the detector at $t^+ = -2$.

At $t^+ = -20$ there is no discernable structure, as Figure 3.8(a) shows. At $t^+ = -10$, the vectors above the detection point ($y^+ = 30, z^+ = 5$) have oriented slightly indicating some upward motion. The vectors near the wall indicate motion towards the detector. Although the vectors are still weak, the bottom part of a vortical structure is beginning to emerge. The vortical structure is more evident at $t^+ = -5$ (Figure 3.8(c)). At $t^+ = -2$, which corresponds to the strongest part of the burst, a strong vortical structure can be seen with its center between $y^+ = 35$ and 50 , and between $z^+ = 35$ and 50 . The structure is still very evident at $t^+ = 0$, but by $t^+ = 5$, when the burst has disappeared, only remnants of the top of structure can be seen. By $t^+ = 10$, there is no longer any kind of a structure.

At the negative times, which correspond to the leading edge of the structure downstream of the detector, the vectors at $y^+ = 35$ have a negative w component which becomes positive after $t^+ = 0$. This indicates that the center of the vortical structure has moved closer to the wall as the time increased, and suggests that the structure is

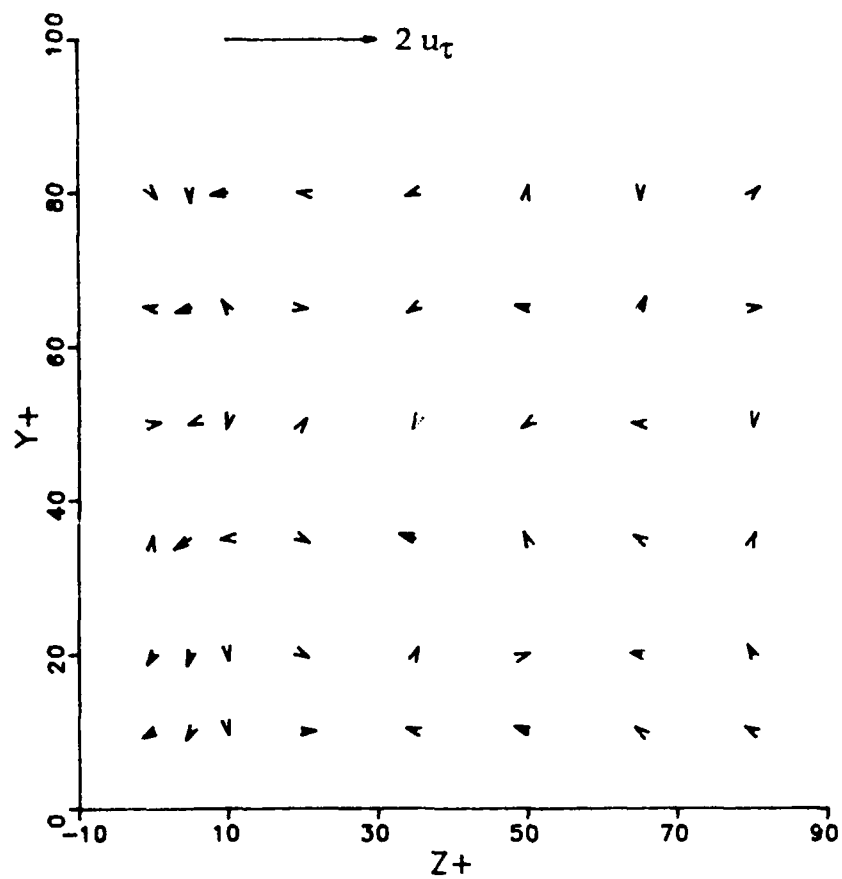


Figure 3.8(a) v-w velocity vectors at $t^+ = -20$.

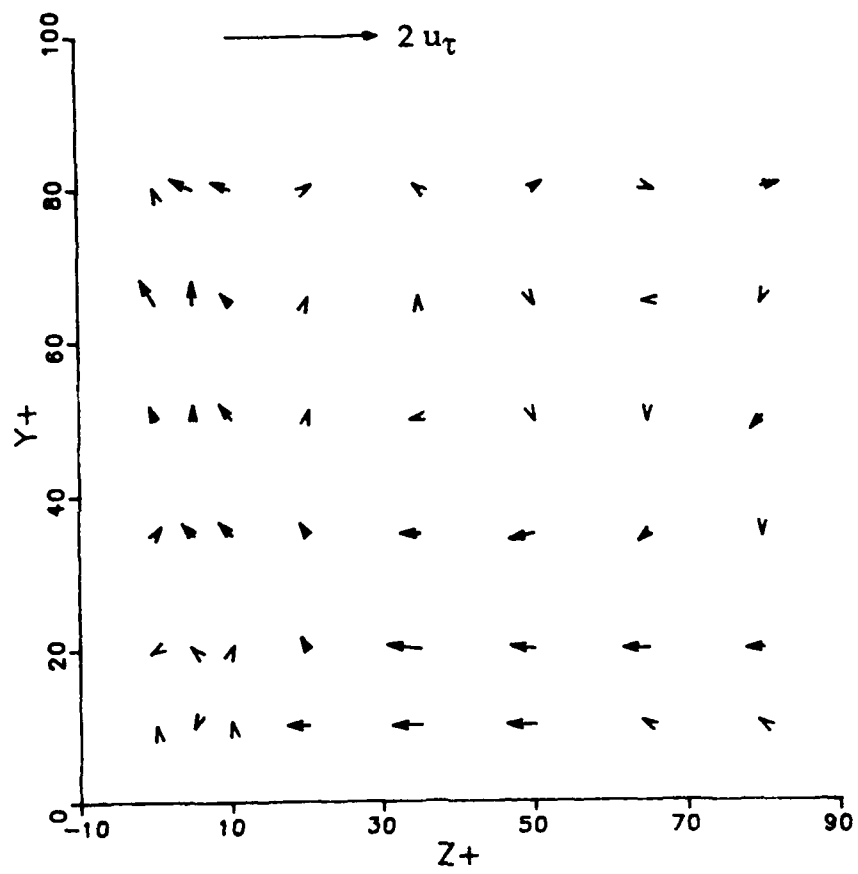


Figure 3.8(b) v-w velocity vectors at $t^+ = -10$.

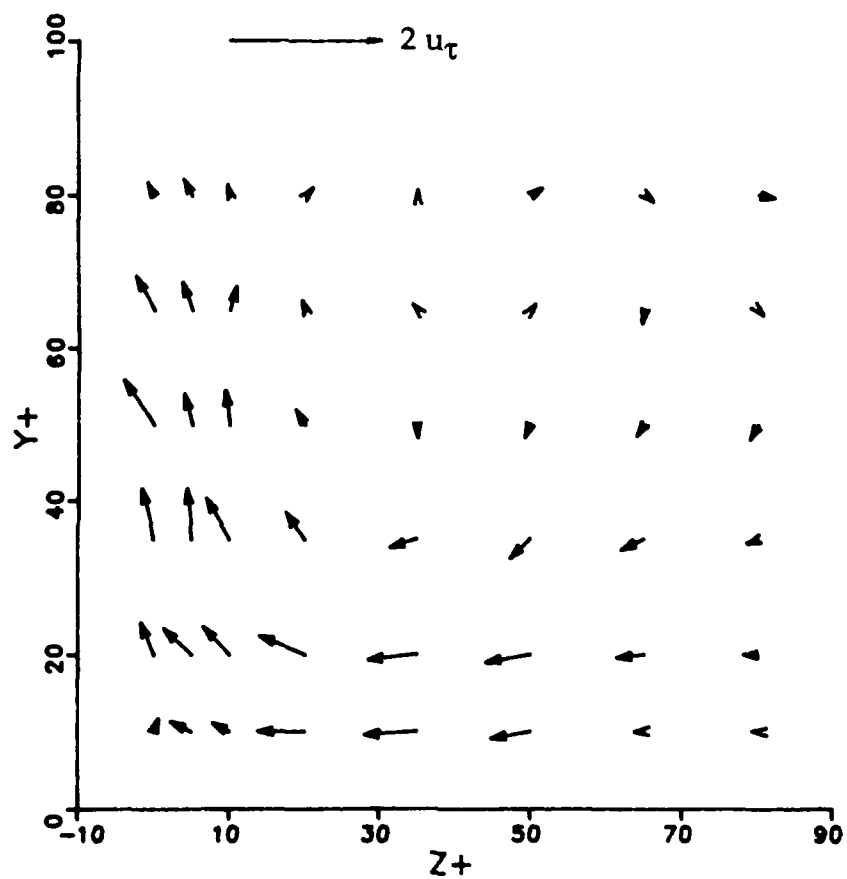


Figure 3.8(c) v - w velocity vectors at $t^+ = -5$.

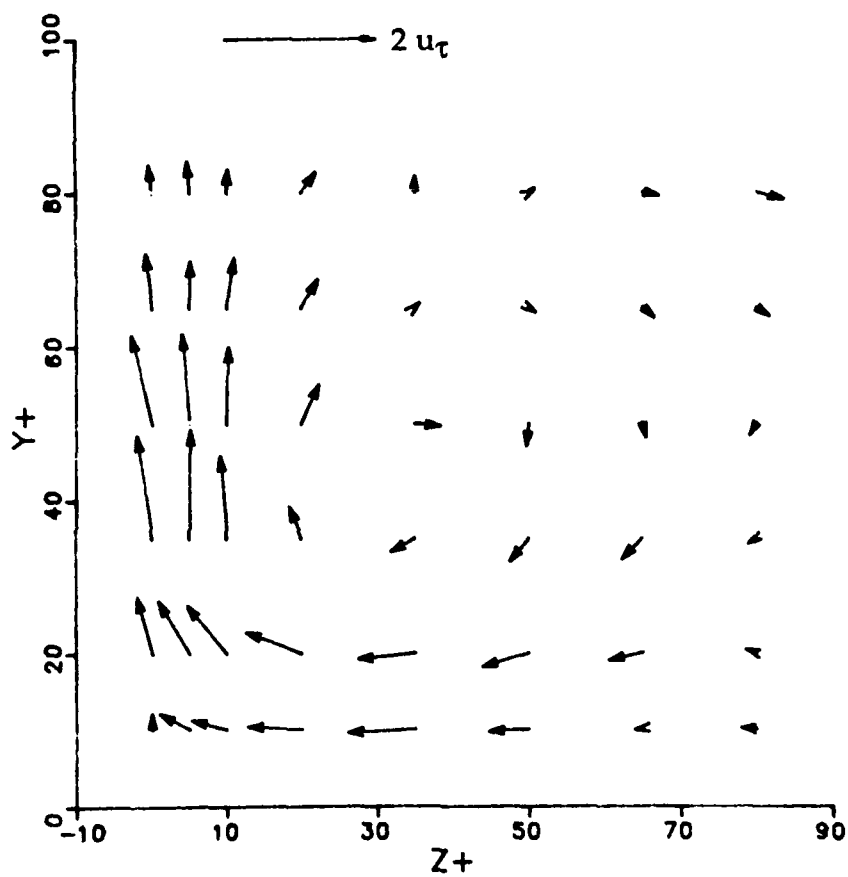


Figure 3.8(d) v-w velocity vectors at $t^+ = -2$.

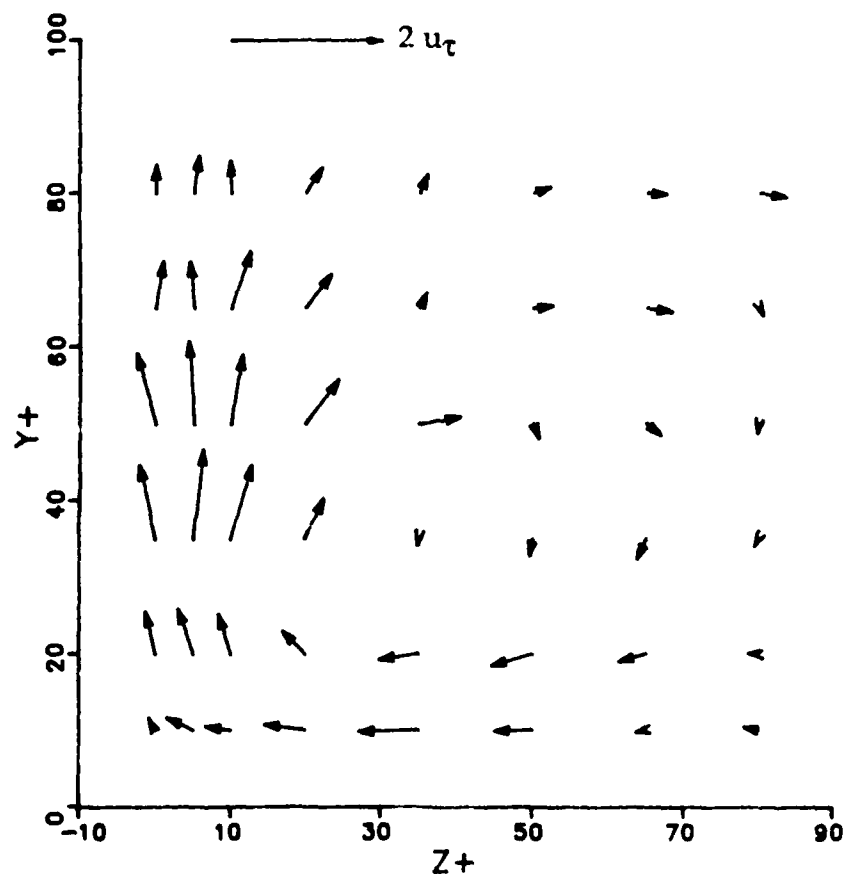


Figure 3.8(e) v - w velocity vectors at $t^+ = 0$.

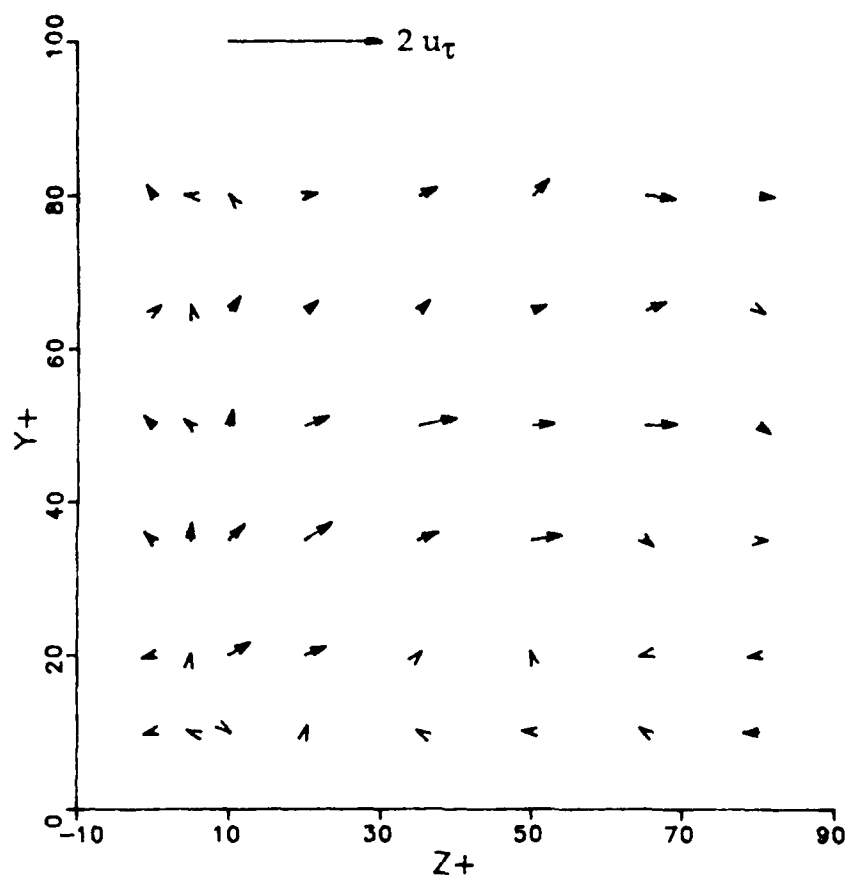


Figure 3.8(f) v-w velocity vectors at $t^+ = 5$.

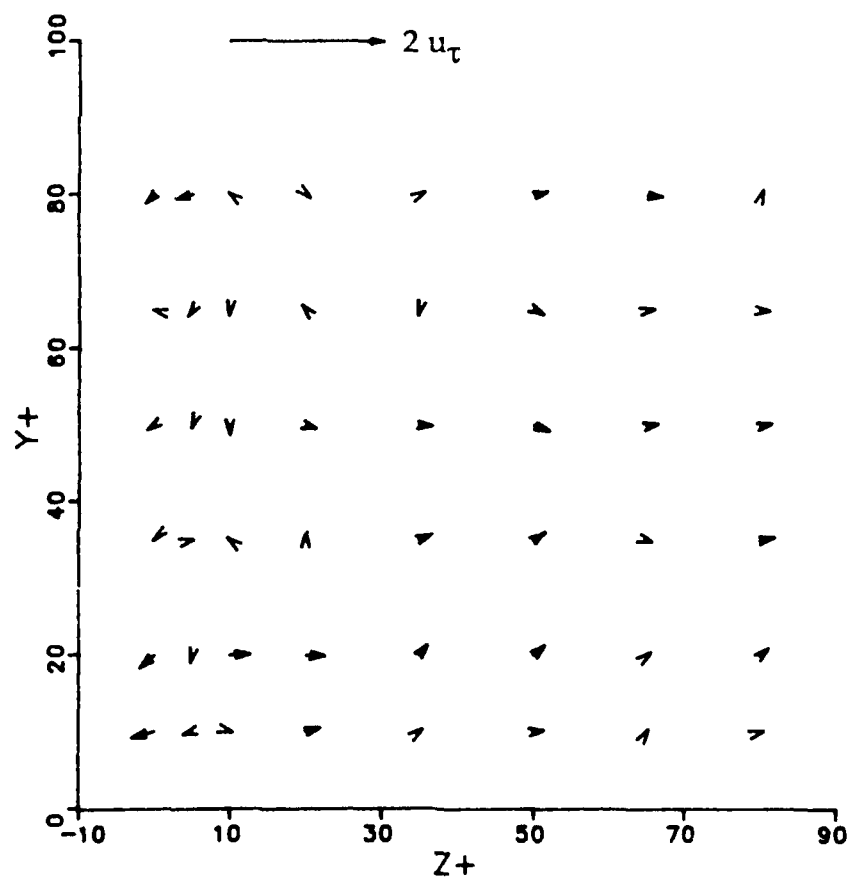


Figure 3.8(g) v-w velocity vectors at $t^+ = 10$.

inclined to the wall with the leading edge above the trailing edge. Inclined vortical structures were also observed in the flow visualization studies by Praturi & Brodkey (1978), and Kreplin & Eckelmann (1979) deduced from space-time correlations that the vortical structures were inclined at about 5° .

The U velocity contours corresponding to the v - w vectors of Figure 3.8 are shown in Figure 3.9(a)-(g). These contours represent the absolute U velocity normalized with u_τ . The broken lines represent the time-averaged local mean velocities. At $t^+ = -20$, the U velocity is close to the local mean velocity, but at $t^+ = -10$ some uplifting of slow speed fluid can be seen in the region around the detector. At $t^+ = -5$ the uplifting is more pronounced while some intruding of high speed fluid can be seen at $60 \leq z^+ \leq 80$. At $t^+ = -2$ and $t^+ = 0$ the effect of intruding fluid extends down to the near-wall region, while the uplifting is at its strongest. The "peaks" of the high speed fluid have moved from $z^+ \approx 70$ to $z^+ \approx 50$ near the wall, while the peaks of the low speed fluid have moved from $z^+ \approx 5$ to $z^+ \approx 10$ further away from the wall. This is likely due to the vortical structure drawing the high and low speed fluid in the direction of the vortical rotation. From $t^+ = 5$ to $t^+ = 10$ the velocity relaxes back to the local mean levels.

The overall time evolution of the burst and the vortical structure is shown in Figures 3.10 and 3.11. A region of high speed fluid may be seen to occur in conjunction with the burst and to its side.

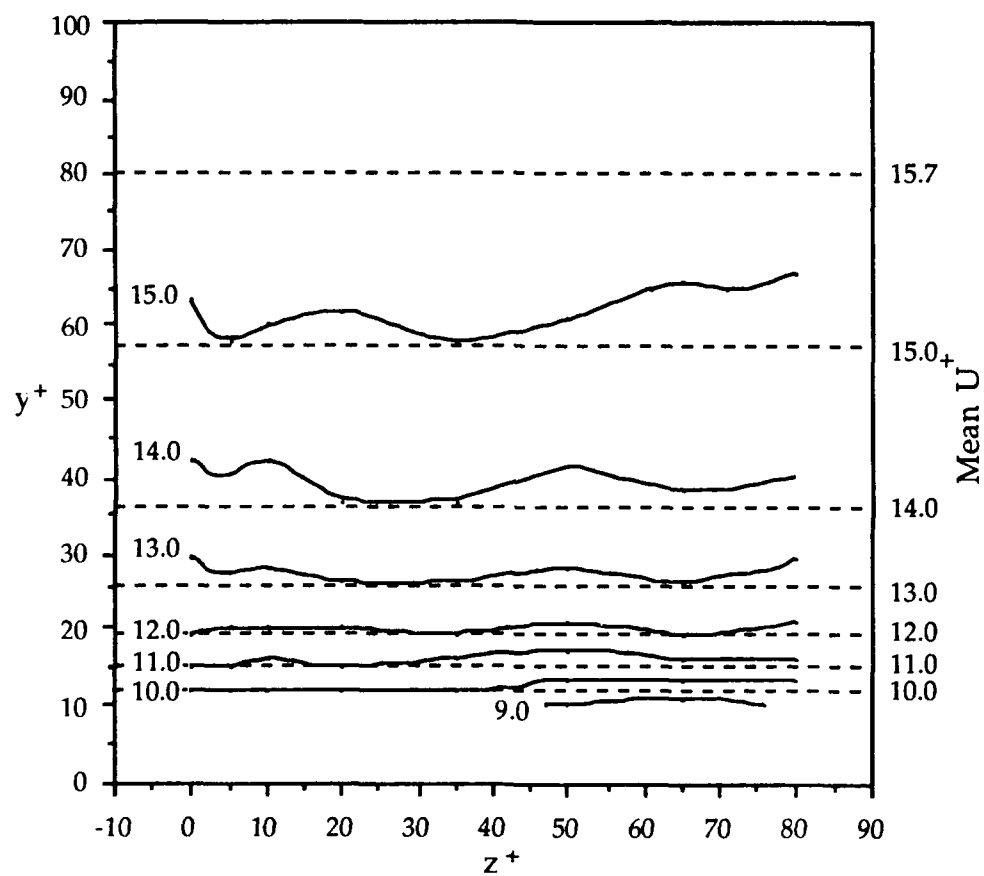


Figure 3.9(a) U^+ velocity contours at $t^+ = -20$.

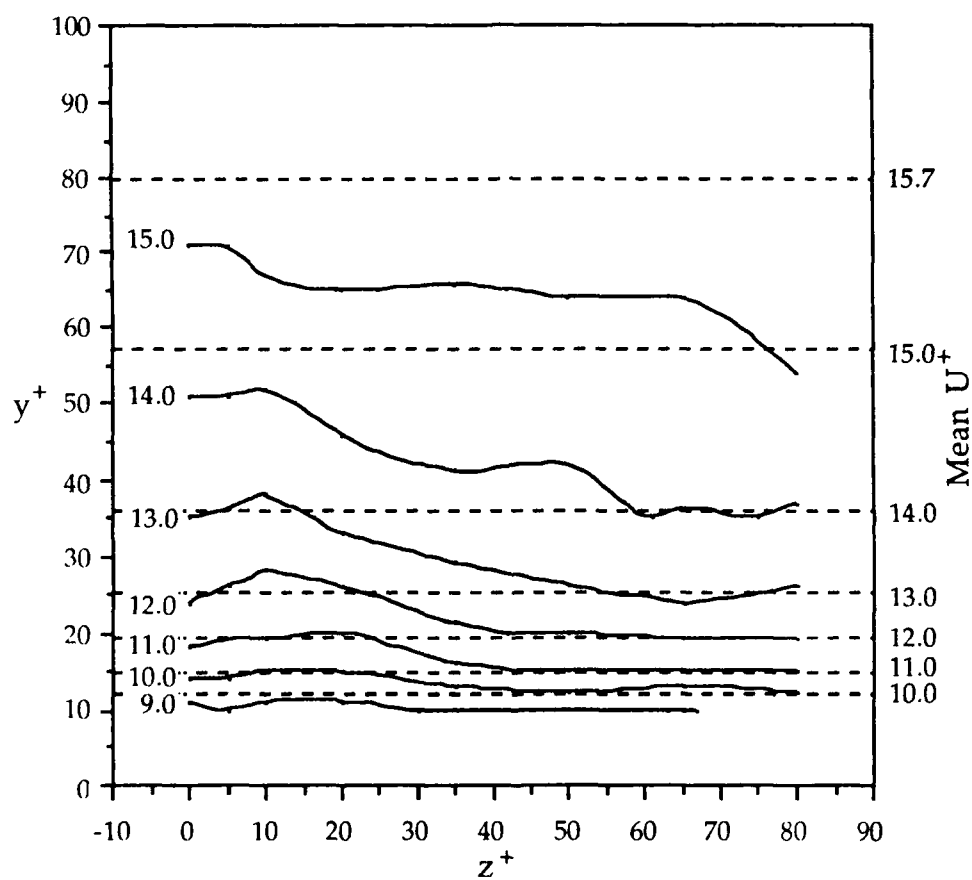


Figure 3.9(b) U^+ velocity contours at $t^+ = -10$.

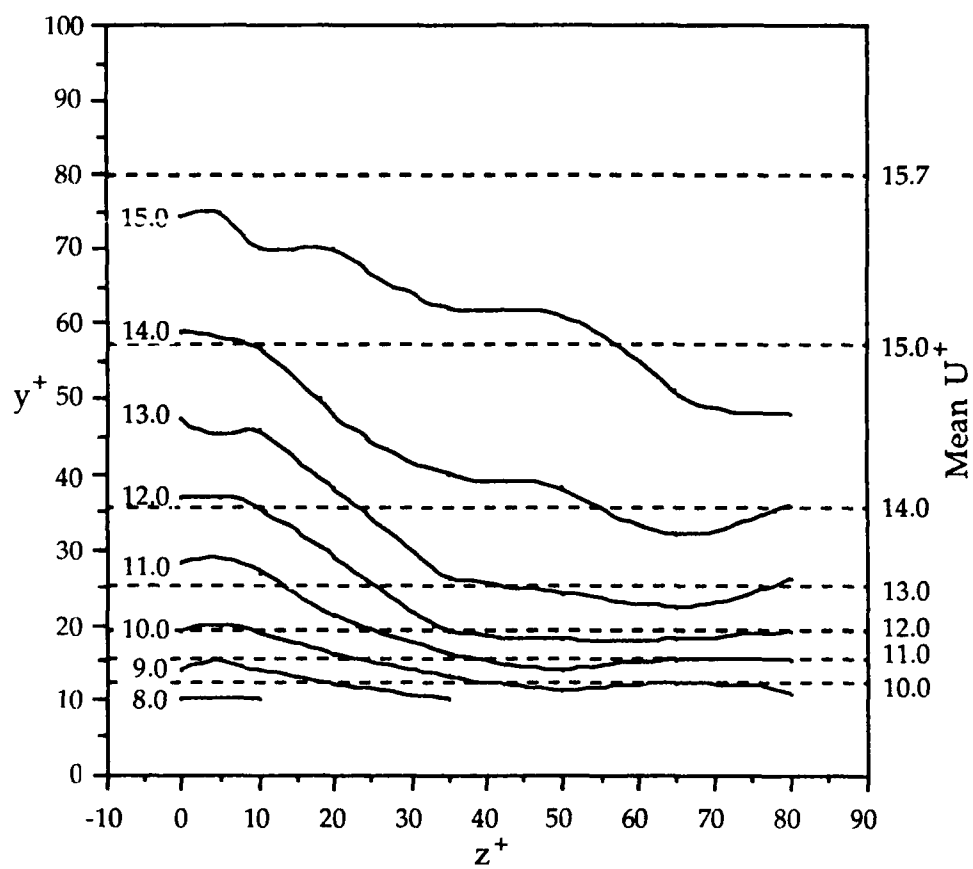


Figure 3.9(c) U^+ velocity contours at $t^+ = -5$.

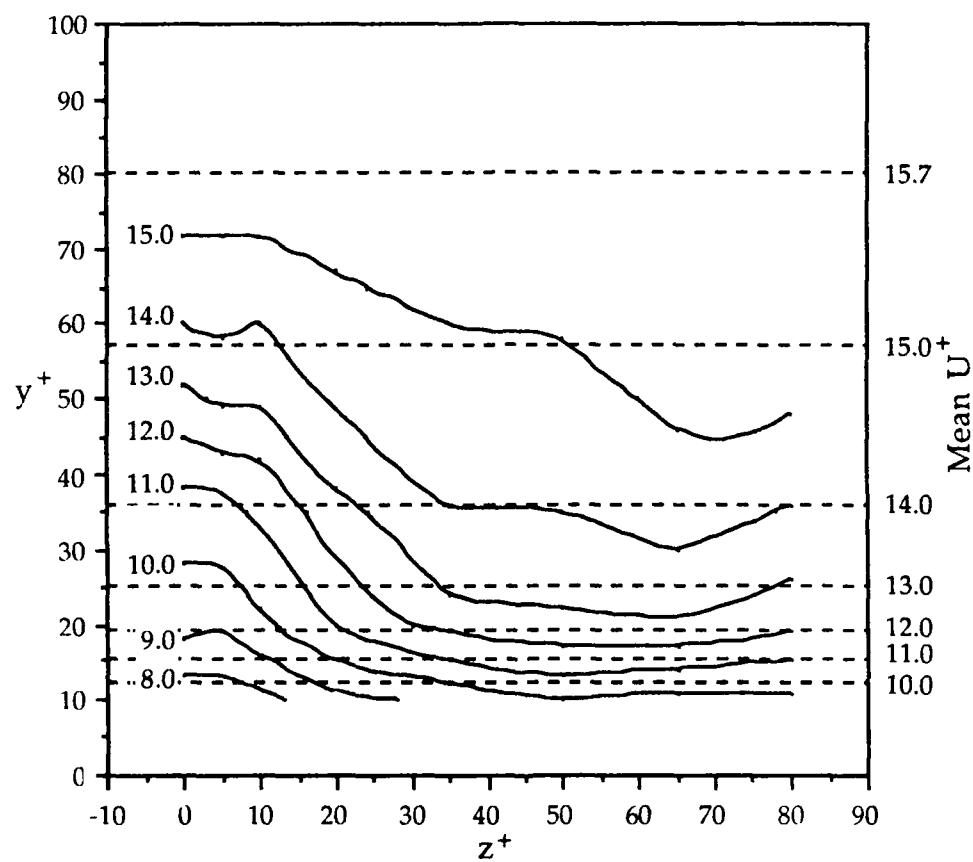


Figure 3.9(d) U^+ velocity contours at $t^+ = -2$.

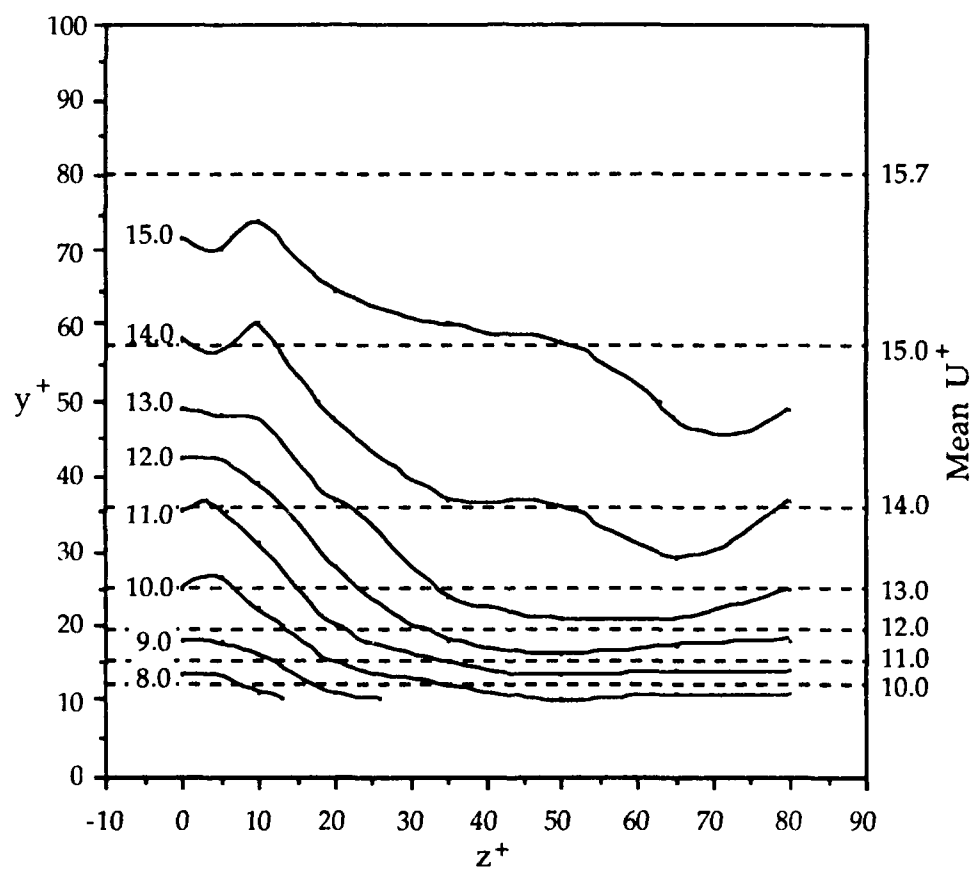


Figure 3.9(e) U^+ velocity contours at $t^+ = 0$.

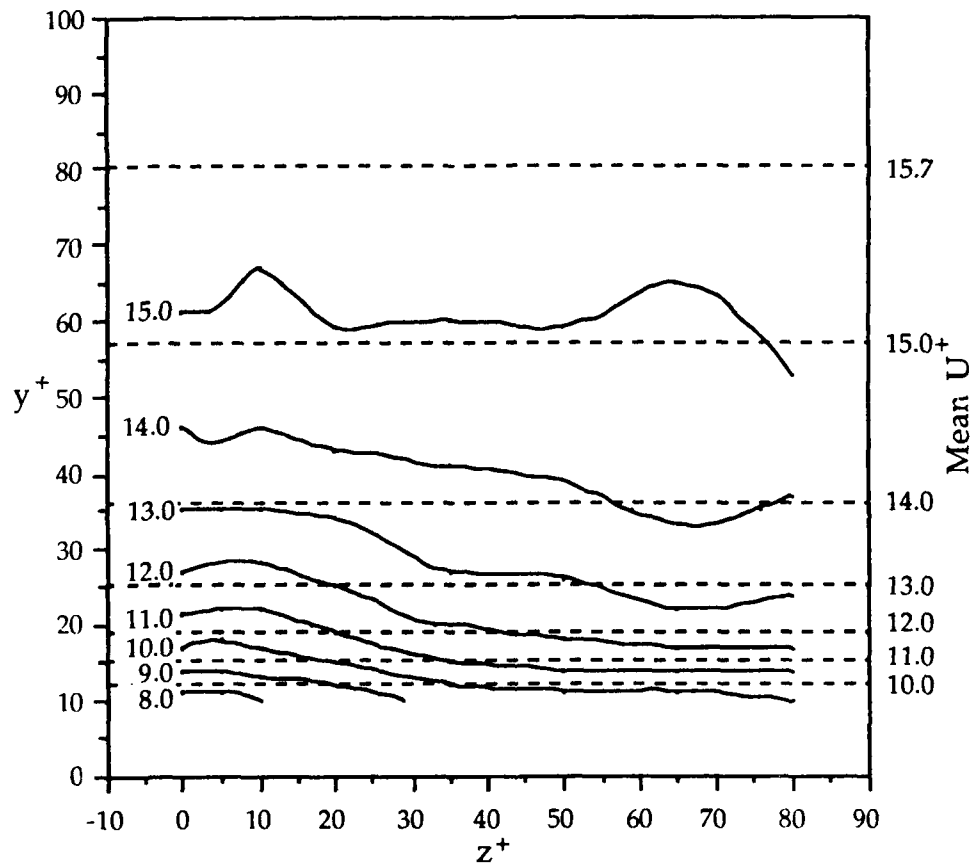


Figure 3.9(f) U^+ velocity contours at $t^+ = 5$.

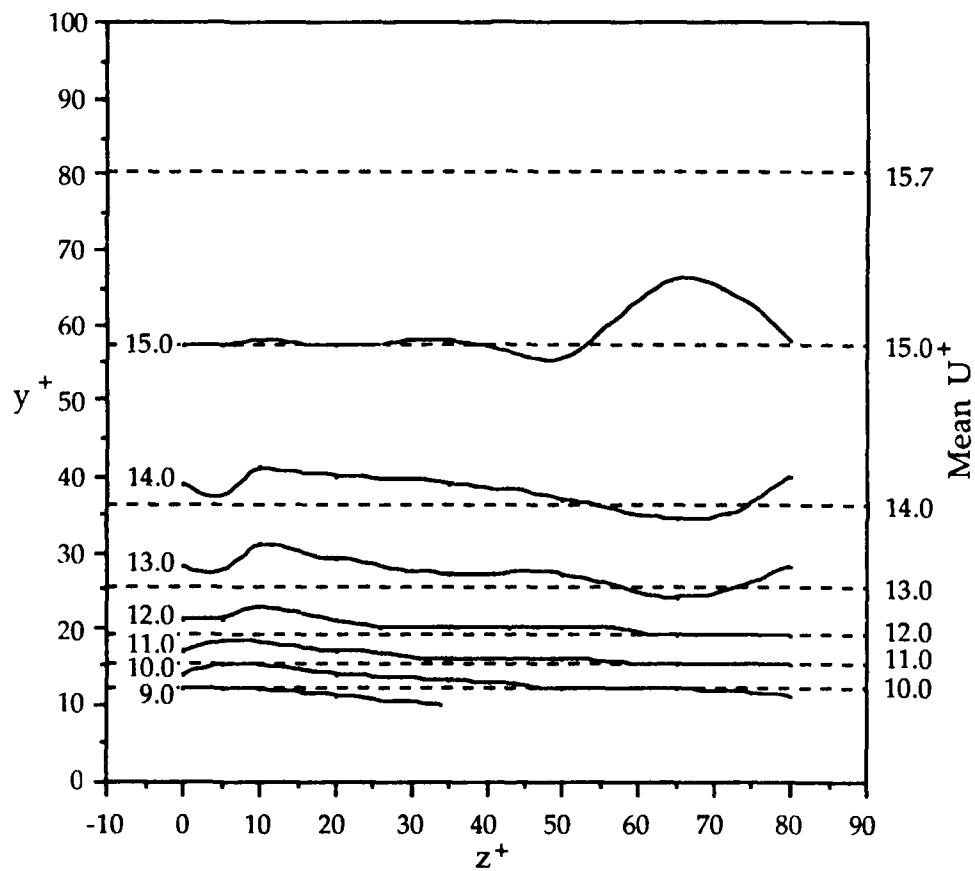


Figure 3.9(g) U^+ velocity contours at $t^+ = 10$.

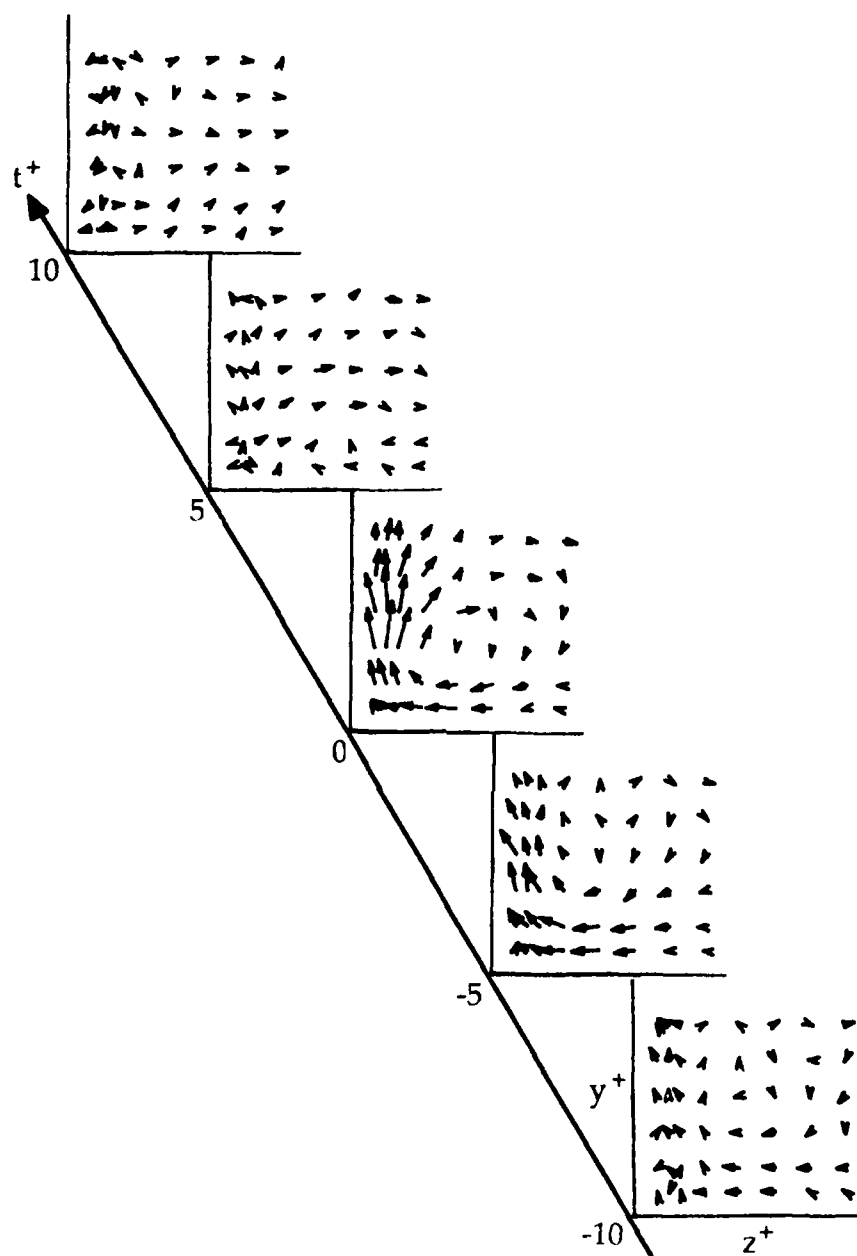


Figure 3.10 Time sequence of v - w vectors in the y - z plane.

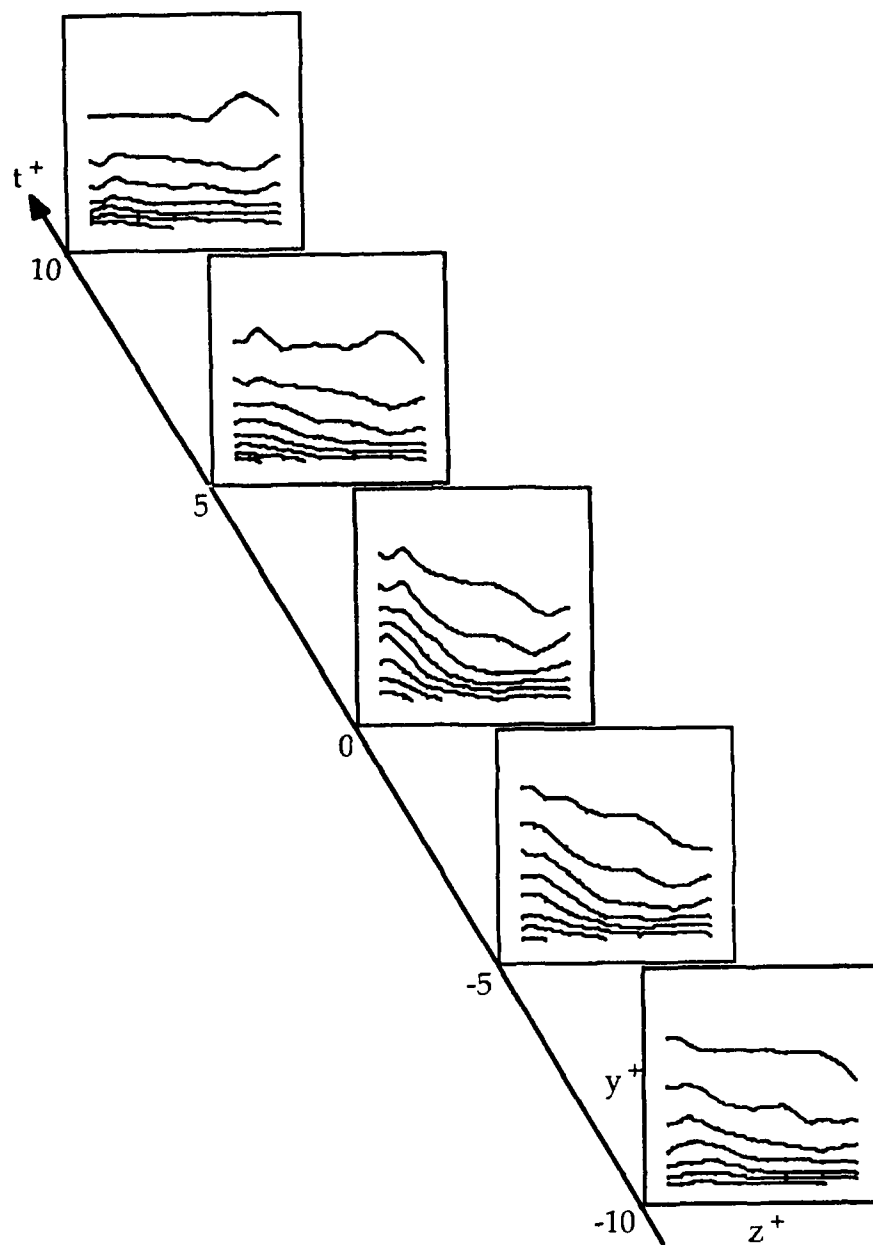


Figure 3.11 Time sequence of U^+ contours in the y - z plane.

Sweeps occurring to the side of bursts were reported by Robinson et al. (1988) and Wark (1988).

The u , v and uv contours normalized with u_τ at $t^+ = -2$ are shown in Figures 3.12 to 3.14. The peaks of the contours are in the region around $(y^+, z^+) = (35, 5)$, which is just above the detection point. The region of high speed fluid is evident to the side of the burst. The u and uv contours show the high speed region angled in the direction of rotation of the vortical structure.

3.2.2 Determination of convection velocity

The mapping of the flow field was done in a plane normal to the direction of flow, as described in Section 2.4.1. Thus, the characteristics of the flow field in the streamwise direction were measured in time. However, it may be more meaningful to study the characteristics in spatial coordinates that would give a better physical sense of the characteristics. A convection velocity is required to convert the time scale to a length scale. Also, by following a structure at its convection velocity an observer may see the interaction of the flow field with that structure.

Several researchers in the past have determined the convection velocity of the burst, and found it to be close to the local mean velocity, U_m . Lu & Willmarth (1973), using the Quadrant detection technique, found the convection velocity to be $0.8 U_m$ at $y^+ \approx 39$.

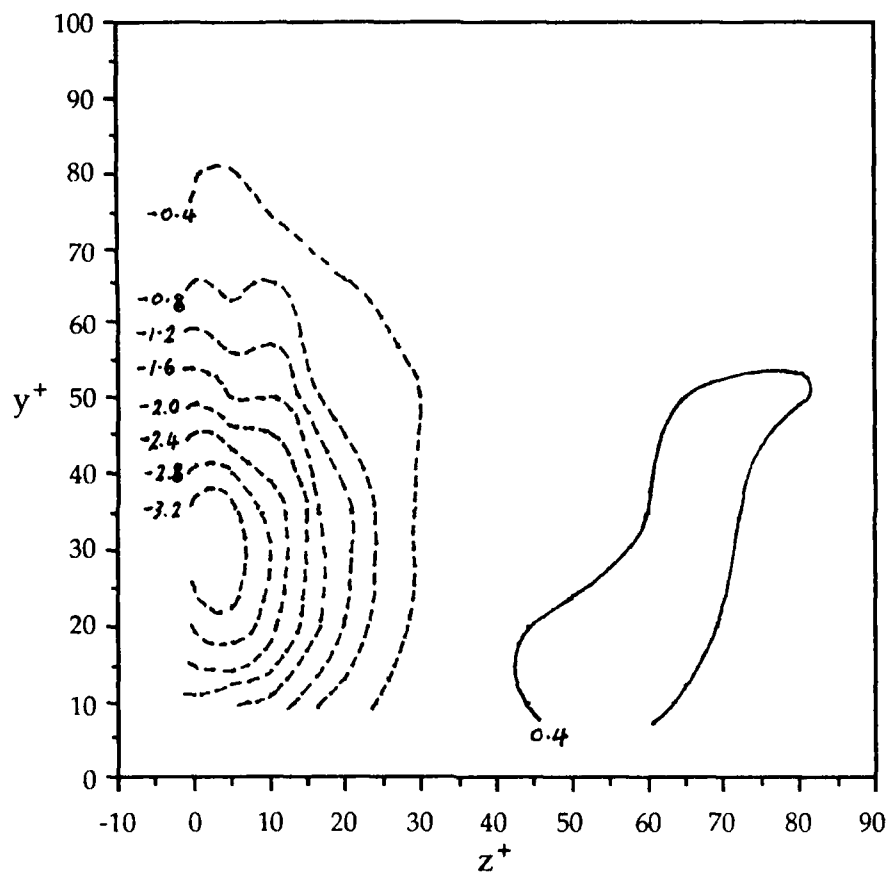


Figure 3.12 u velocity contours in the y - z plane at $t^+ = -2$, in increments of 0.4.

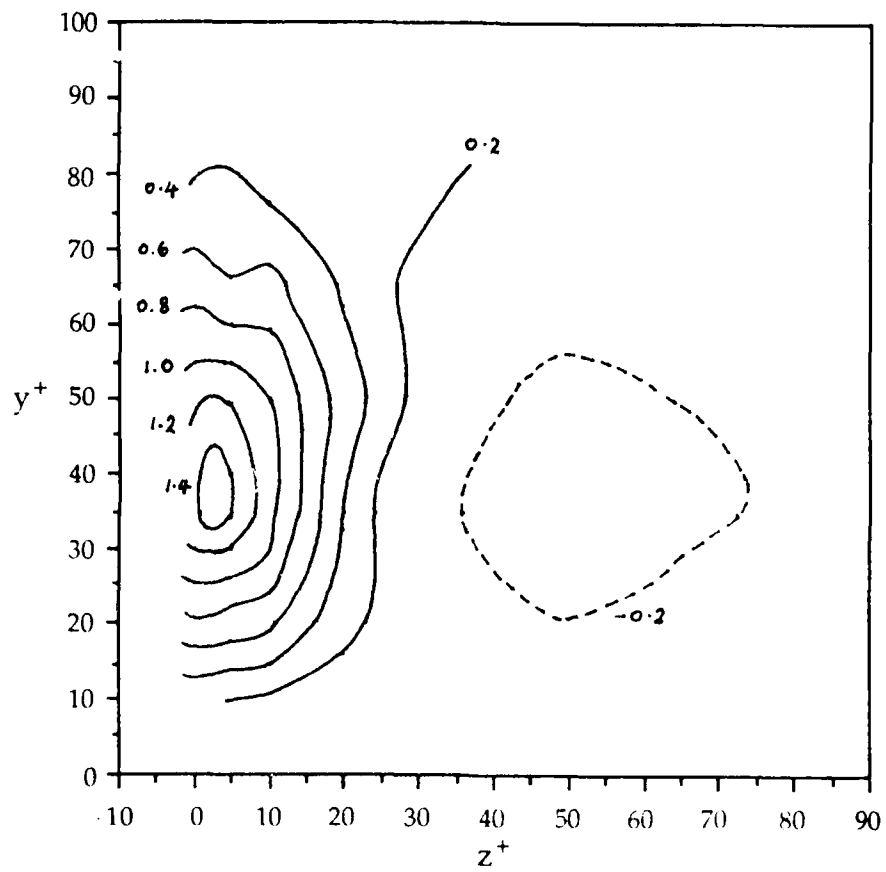


Figure 3.13 v velocity contours in the y - z plane at $t^+ = -2$, in increments of 0.2.

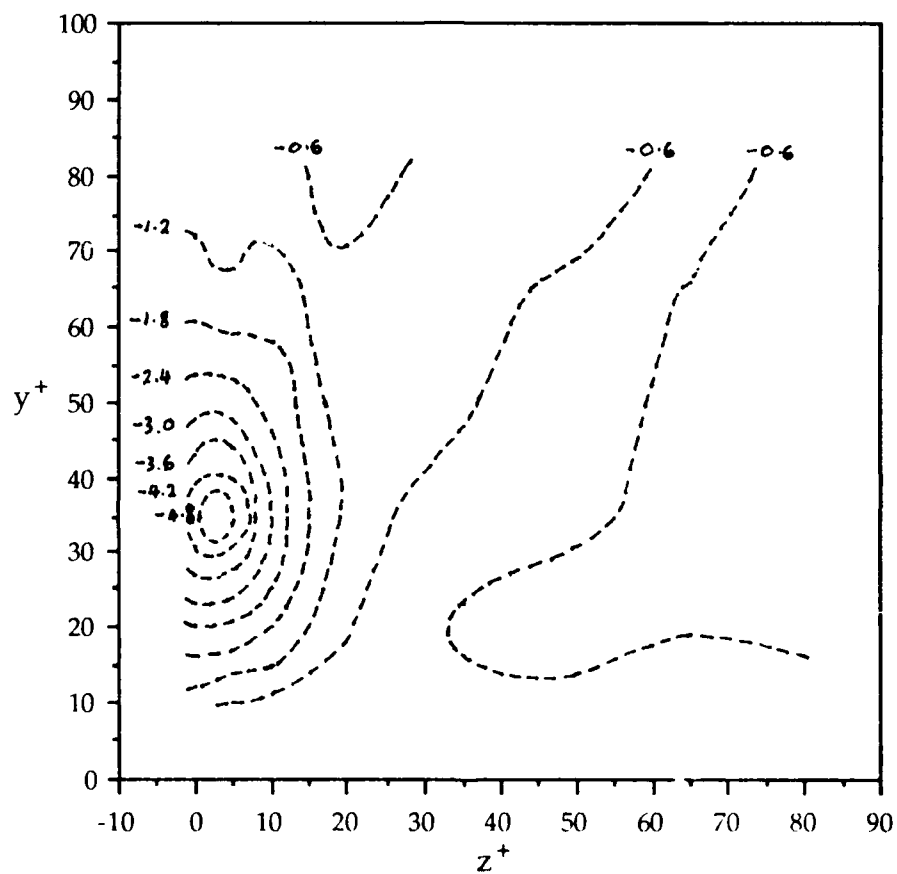


Figure 3.14 uv product contours in the y - z plane at $t^+ = -2$, in increments of 0.6.

Guezennec et al. (1987), also using Quadrant detection in their numerical simulation, reported a convection velocity of $0.98 U_m$ at $y^+ = 12$. Johansson, Alfredsson & Eckelmann (1987) found that their VITA-detected events had a constant convection velocity of $1.1 U_m$ near the wall ($y^+ < 20$) and close to U_m further away. The VITA technique basically detects events by looking within a short time interval for variances which exceed the long-time variance of the flow by some threshold. Thus, VITA essentially detects shear layers where steep velocity gradients have large short-time variances compared to the long-time variance. Johansson, Alfredsson & Kim (1987), using VISA detection, found that the convection velocity was $0.96 U_m$ for $y^+ < 15$. VISA is the spatial equivalent of VITA, and looks at variances over a short distance.

A definitive measure of the convection velocity would be obtained by a two-point correlation at the same y location separated in the streamwise direction. Since the measurement probes were not arranged in this manner for this experiment, the convection velocity could not be determined directly. One choice for the convection velocity would be the local mean velocity. From this viewpoint, an observer is following the flow at its mean velocity. Another appropriate convection velocity would be the mean velocity of the burst structure. To determine this velocity, an area integration of the ensemble averaged u contour levels in the z - x plane was done. An appropriate minimum contour level must be determined since the

convection velocity will depend on it. The minimum contour level was determined by $\frac{2u'}{\sqrt{N}}$ where u' is the rms velocity and N the number of events in the ensemble average. Contour levels below that value will be random noise. The convection velocity was found to be about $1 u_\tau$ less than the local mean U velocity at $y^+ = 20$ and 35 .

3.2.3 Results in the x-y plane

Results in the streamwise vertical plane at $z^+ = 5$ are presented in this section. Figure 3.15 shows the u_c - v velocity vectors in this plane. The vector component u_c is the absolute U velocity minus the convection velocity. From this viewpoint, an observer is following the burst at its convection velocity and sees the characteristics of the flow field relative to the burst. Although the convection velocity of the burst varies with y , an observer following the burst can reasonably be expected to only follow the structure at one convection velocity. As discussed in Appendix D, the characteristics of the structure is not significantly affected by the choice of convection velocity. The convection velocity used in Figure 3.15 was $12 u_\tau$, which is the average of the convection velocities at $y^+ = 20$ and 35 .

It can be seen from the figure that the uplifting of the burst begins gradually near the wall ($y^+ \leq 20$) and becomes stronger further away in the region of $20 \leq y^+ \leq 50$. Above $y^+ = 50$ the burst is swept forward and does not look to go much beyond $y^+ = 80$. A curling

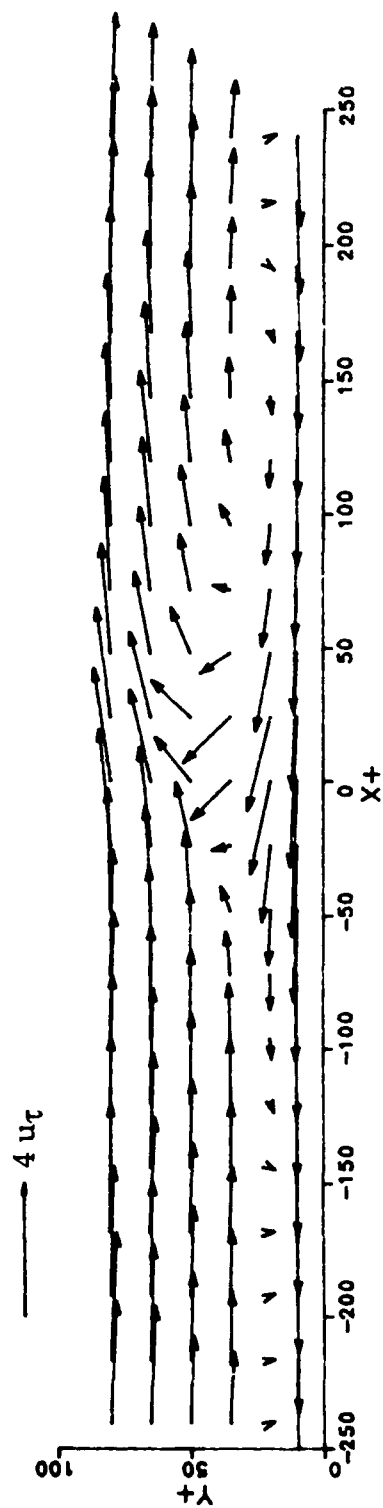


Figure 3.15 u_c-v velocity vectors in the $x-y$ plane at $z^+ = 5$,
with a convection velocity of $12 u_\tau$.

motion of the burst is evident, and may indicate the presence of a transverse vortex. However, this apparent vortical motion may be the result of using a single convection velocity to view the structure. With one convection velocity, there will be higher speed fluid at higher y locations and lower speed fluid near the wall. With a v velocity, this results in a rotational motion.

If a strong transverse vortex does exist, it should also be seen in a plot of the fluctuating velocity component vectors. In this plot, shown in Figure 3.16, the structure represented by the vectors is different from the one in Figure 3.15. A large velocity defect can be seen around the detection point, and the strong uplifting is still evident at $20 \leq y^+ \leq 50$, but the curling motion is not.

Figure 3.17 shows the U velocity contours, normalized with u_τ . The strong uplifting of the event between $y^+ = 20$ and 50 as compared to the near-wall region is again evident. The peaks of the contours can be seen to arc forward in the direction of the flow.

The contours of the fluctuating u velocity, normalized with u_τ , in Figure 3.18 show the structure from a different perspective. The contours show an elongated structure with a steeper velocity gradient at the trailing edge than at the leading edge. This is consistent with the model proposed by Bogard & Tiederman (1987) of high speed fluid impinging on the back of the burst and creating a shear layer with a high velocity gradient.

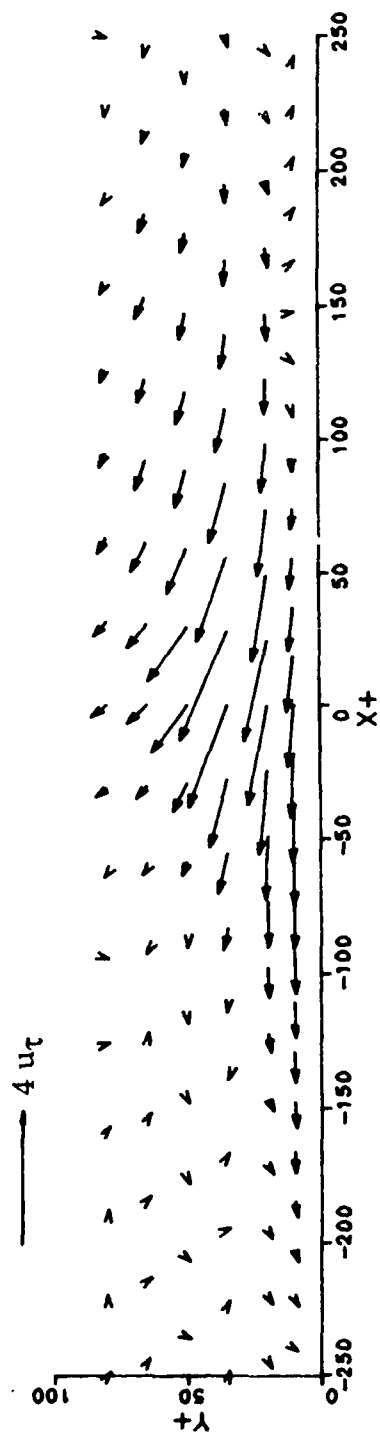


Figure 3.16 u_c-v velocity vectors in the $x-y$ plane at $z^+ = 5$, with the local mean as the convection velocity.

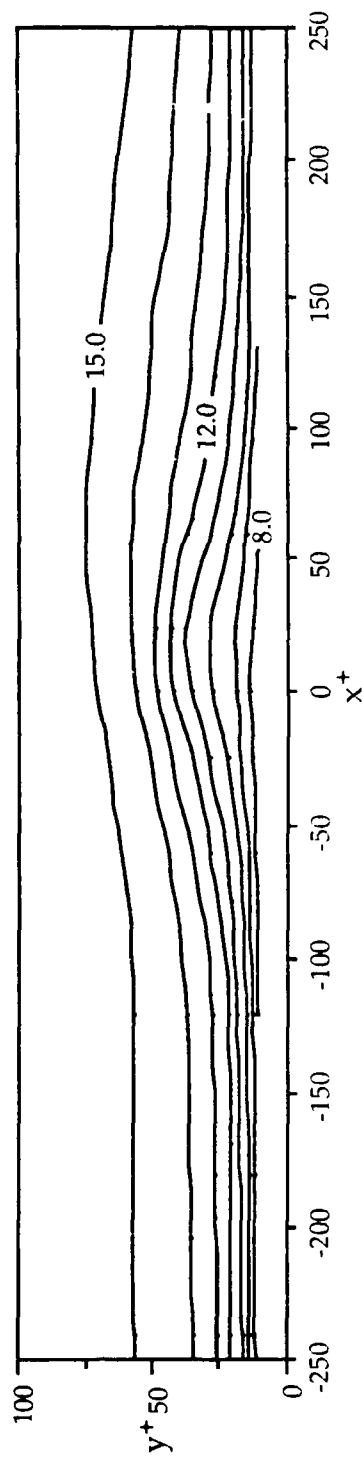


Figure 3.17 U^+ velocity contours in the $x-y$ plane at $z^+ = 5$.

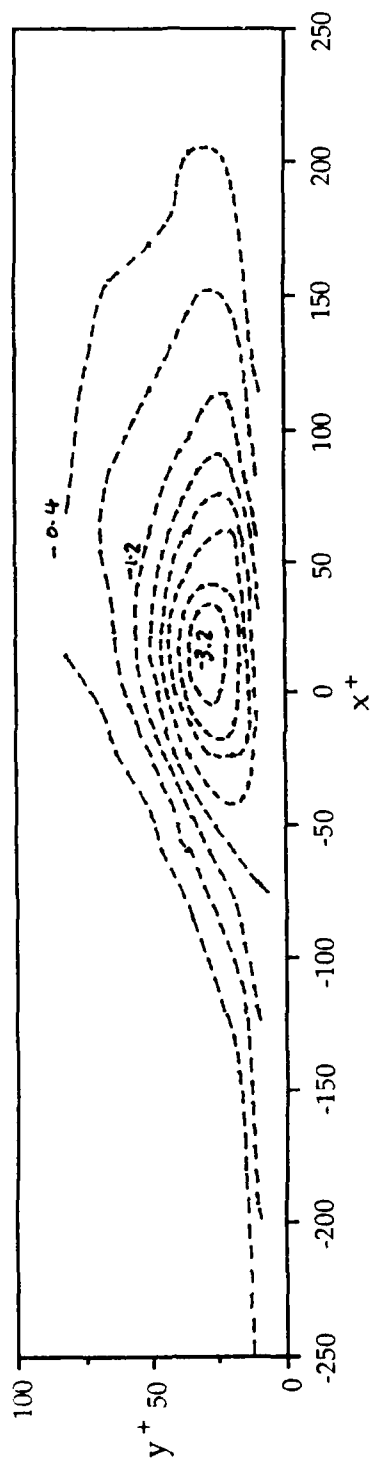


Figure 3.18 u velocity contours in the x - y plane at $z^+ = 5$, in increments of 0.4.

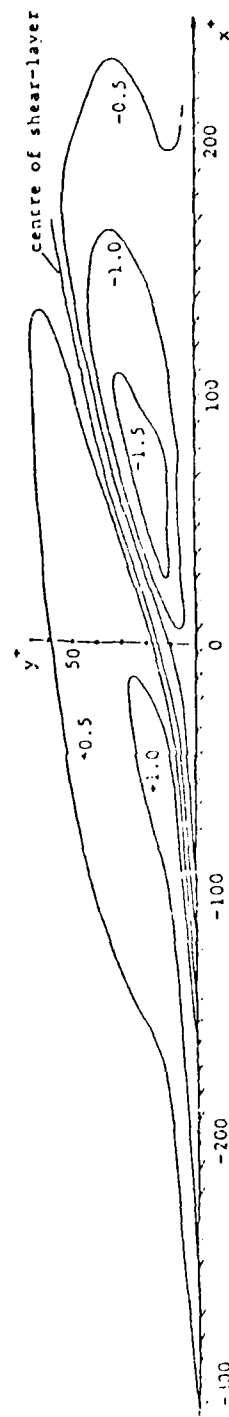


Figure 3.19 u velocity contours in the x - y plane of Johansson, Alfredsson & Eckelmann (1987).

For comparison, Figure 3.19 shows a VITA-detected structure from Johansson, Alfredsson & Eckelmann (1987). The structure in Figure 3.18 may be compared to the low speed structure downstream of the VITA detection shown in Figure 3.19. It should be noted that the contours, which are normalized with the local rms U velocity in Figure 3.19, are similar in magnitude to the contours in Figure 3.18. The characteristics of the structures in terms of the streamwise and vertical extents, and the general shape are very similar.

Johansson, Alfredsson & Kim (1987) used VISA detection in their numerical simulation and obtained a similar negative u velocity structure, as shown in Figure 3.20(a). They normalized the contours with u_{τ} . The characteristics of the positive fluctuating v velocity contours (Figure 3.20(b)) are also similar to those of the v contours in this study, as shown in Figure 3.21. The uv contours in Figure 3.22 show a localized concentration of Reynolds stress in the center of the burst, corresponding to the region where the uplifting is strongest.

3.2.4 Results in the x - z plane

The velocity vector representation of the flow field in the x - z plane using the two convection velocities discussed in Section 3.2.2 showed similar characteristics. However, convection velocities which allow an observer to follow the burst at its lower velocities result in different characteristics, and these are discussed in more detail in

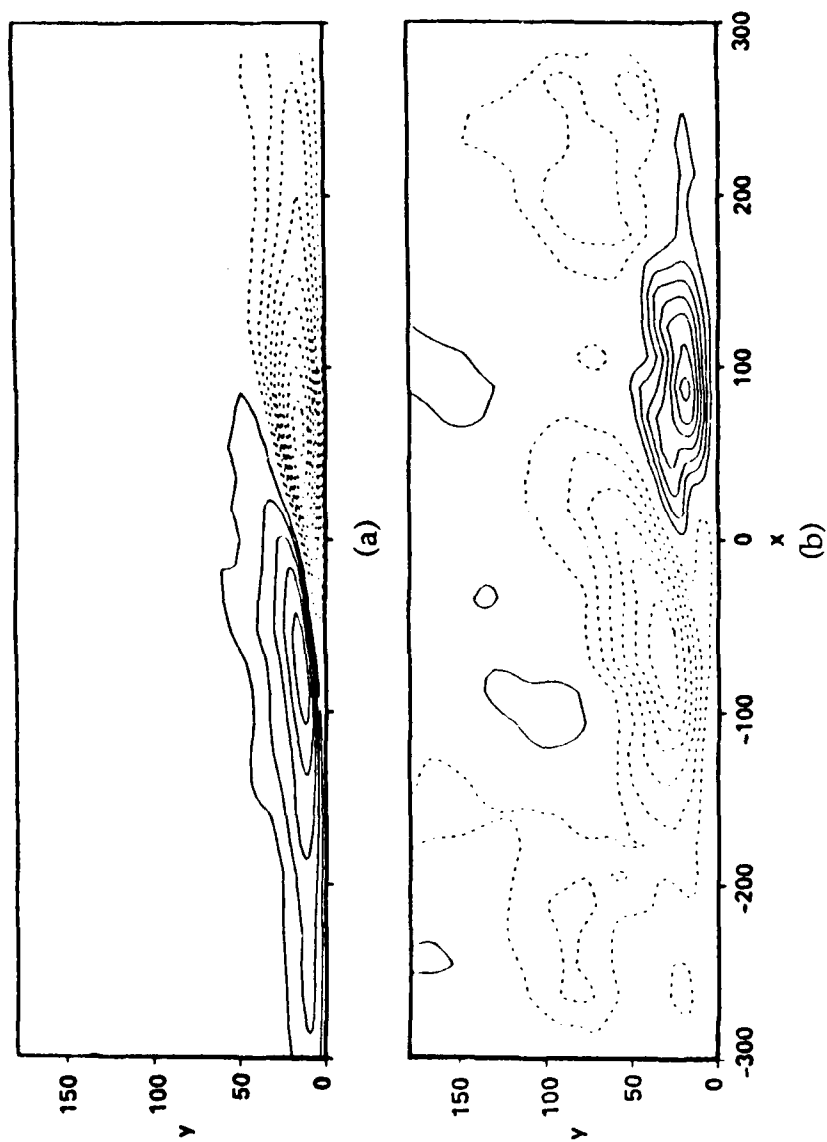


Figure 3.20 Ensemble averaged VISA events of Johansson, Alfredsson & Kim (1987) in the x-y plane. (a) u contours in increments of 0.5. (b) v contours in increments of 0.1.

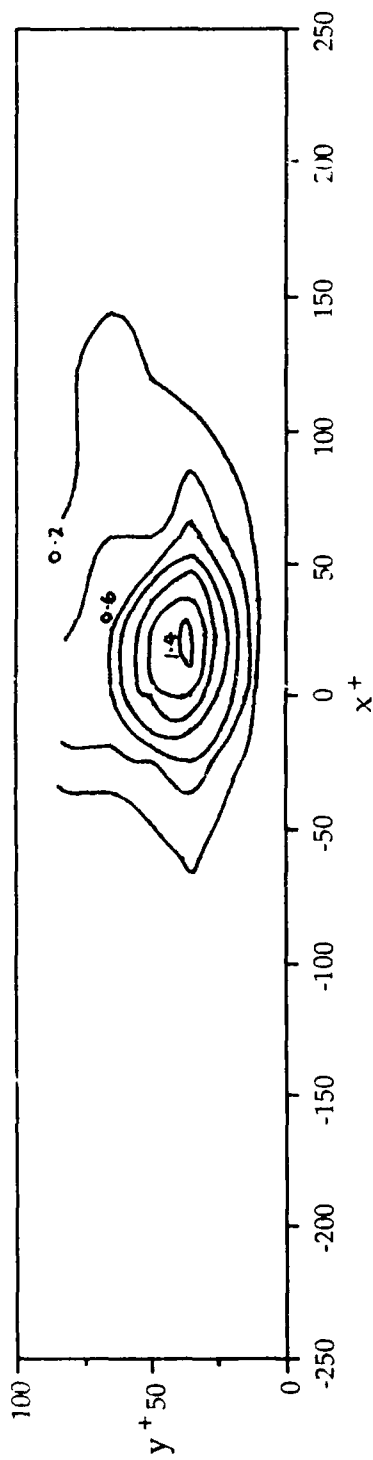


Figure 3.21 v velocity contours in the x - y plane at $z^+ = 5$, in increments of 0.2.

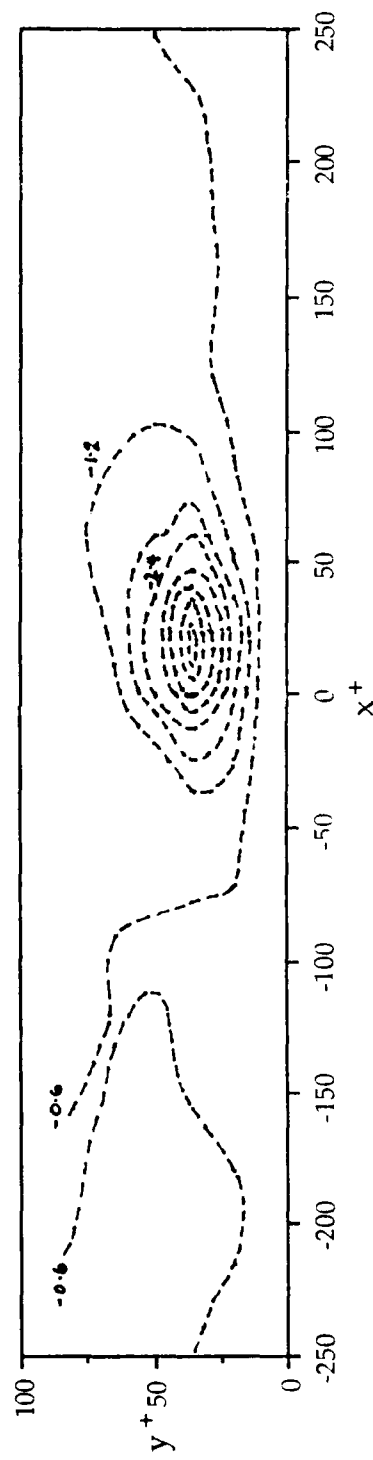


Figure 3.22 uv product contours in the x - y plane at $z^+ = 5$, in increments of 0.6.

Appendix D. In this section, results using the local mean velocity as the convection velocity are presented.

Figure 3.23 shows the u - w velocity vectors in the horizontal planes at $y^+ = 20$ and 35. At both y^+ levels an approximately elliptical vortical structure is evident, with the major axis in the streamwise direction. An elliptical vortical structure would indicate that the vortical structure is inclined to the wall. Furthermore, the center of the vortical structure at $y^+ = 20$ is at $x^+ \approx -50$ while it is at $x^+ \approx 0$ at $y^+ = 35$, which also indicates an inclined structure. Such an inclined structure would be consistent with the movement of the center of the vortical structure discussed in Section 3.2.1.

The contours of the fluctuating u and v velocities are shown in Figures 3.24 and 3.25. The elongated burst structure is evident in the u contours. The high speed fluid moving towards the wall at $y^+ = 35$ may be a sweep structure occurring to the side of the burst. These results are similar to the numerical simulation of Johansson, Alfredsson & Kim (1987) at $y^+ = 15$ (Figure 3.26).

3.3 Results at a higher ejection detection threshold

All the results presented so far have been obtained using an ejection detection threshold of $H \approx 1$. To see what effect threshold has on the characteristics of the structure, conditional sampling was done at a threshold of $H = 4$. As mentioned in Section 2.5.1, $H = 4$ is a value

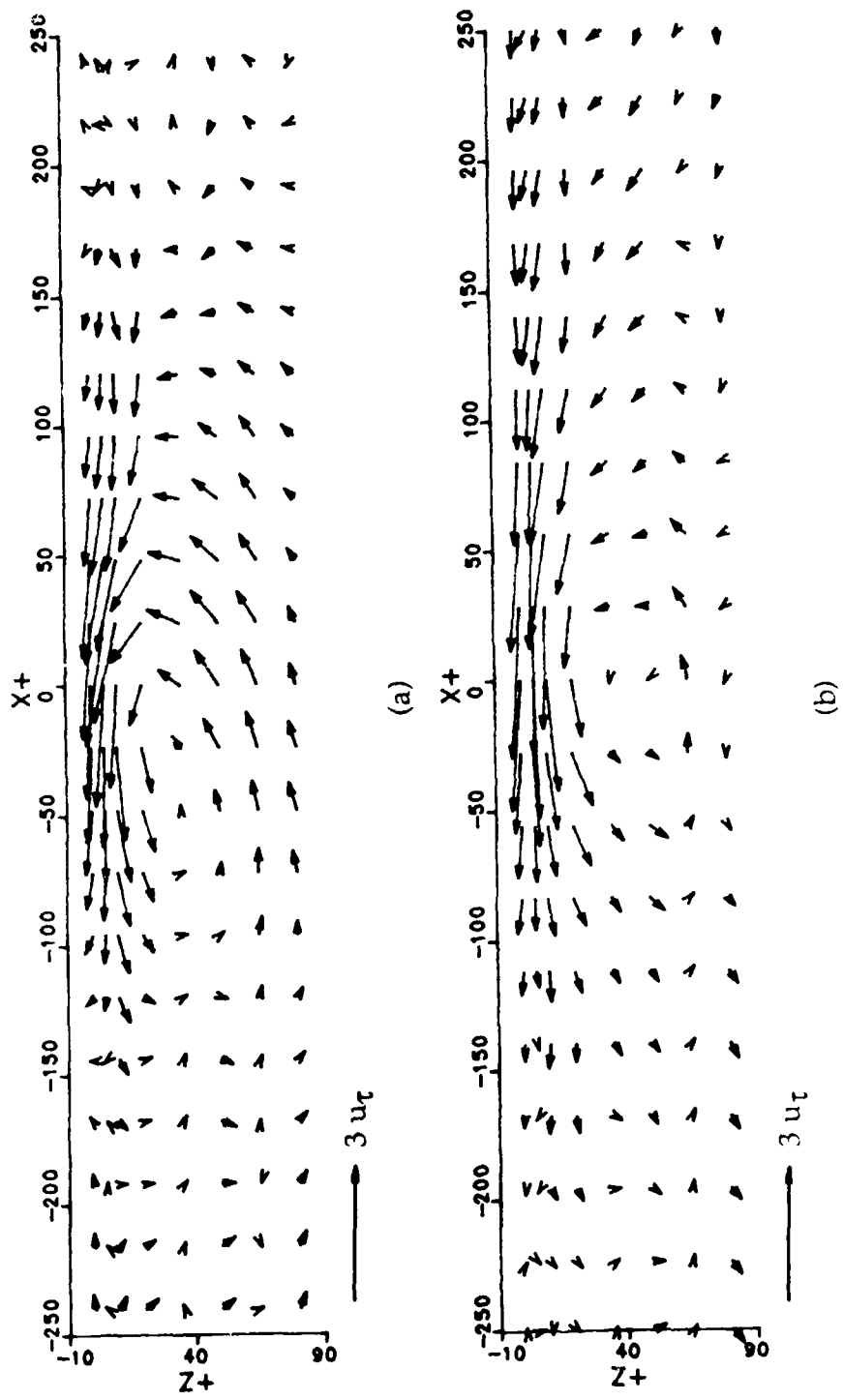


Figure 3.23 u_c - w velocity vectors in x - z plane at (a) $y^+ = 20$ and (b) $y^+ = 35$.

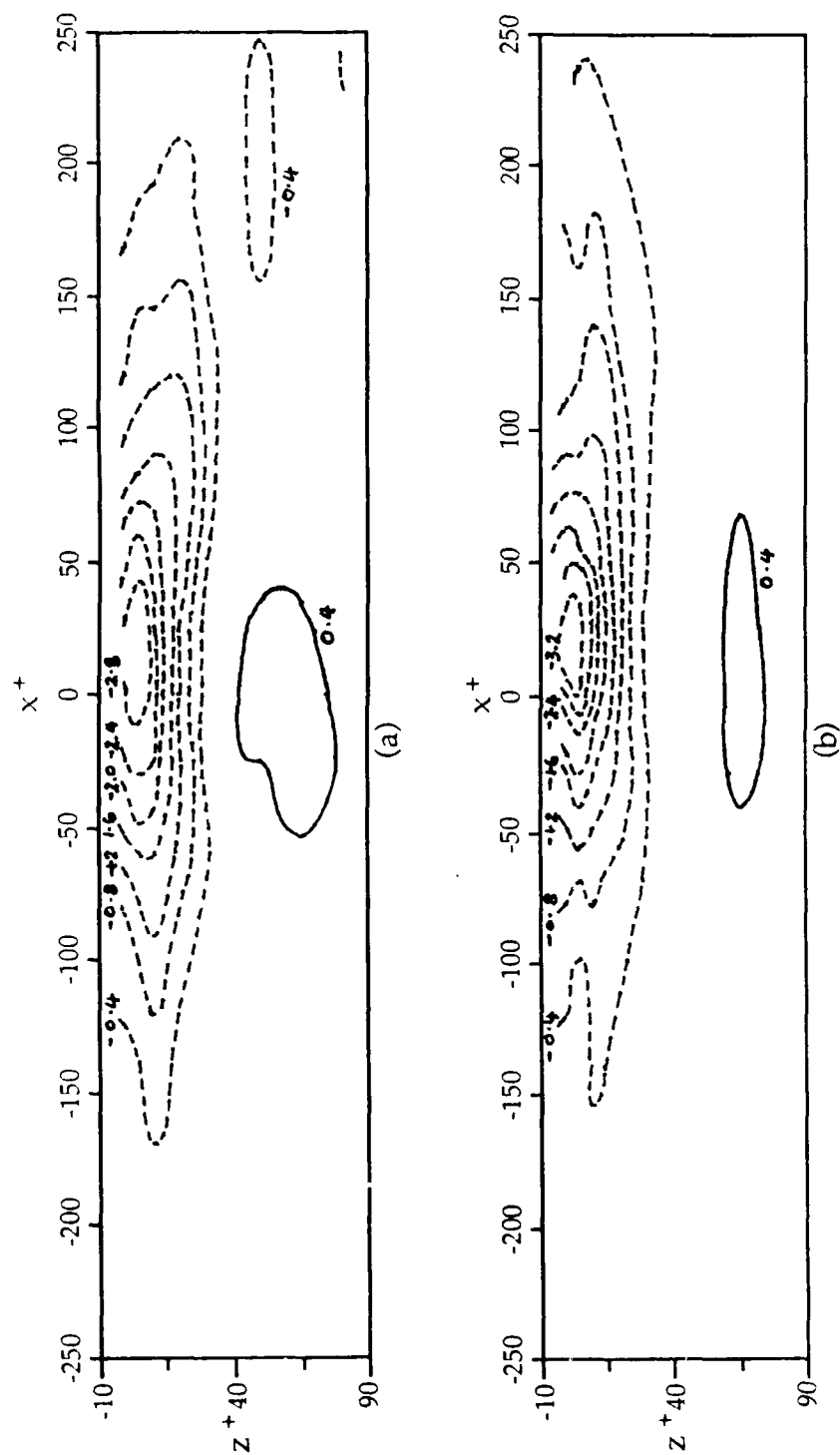


Figure 3.24 u velocity contours in x - z plane at (a) $y^+ = 20$ and (b) $y^+ = 35$. Contour increments of 0.4.

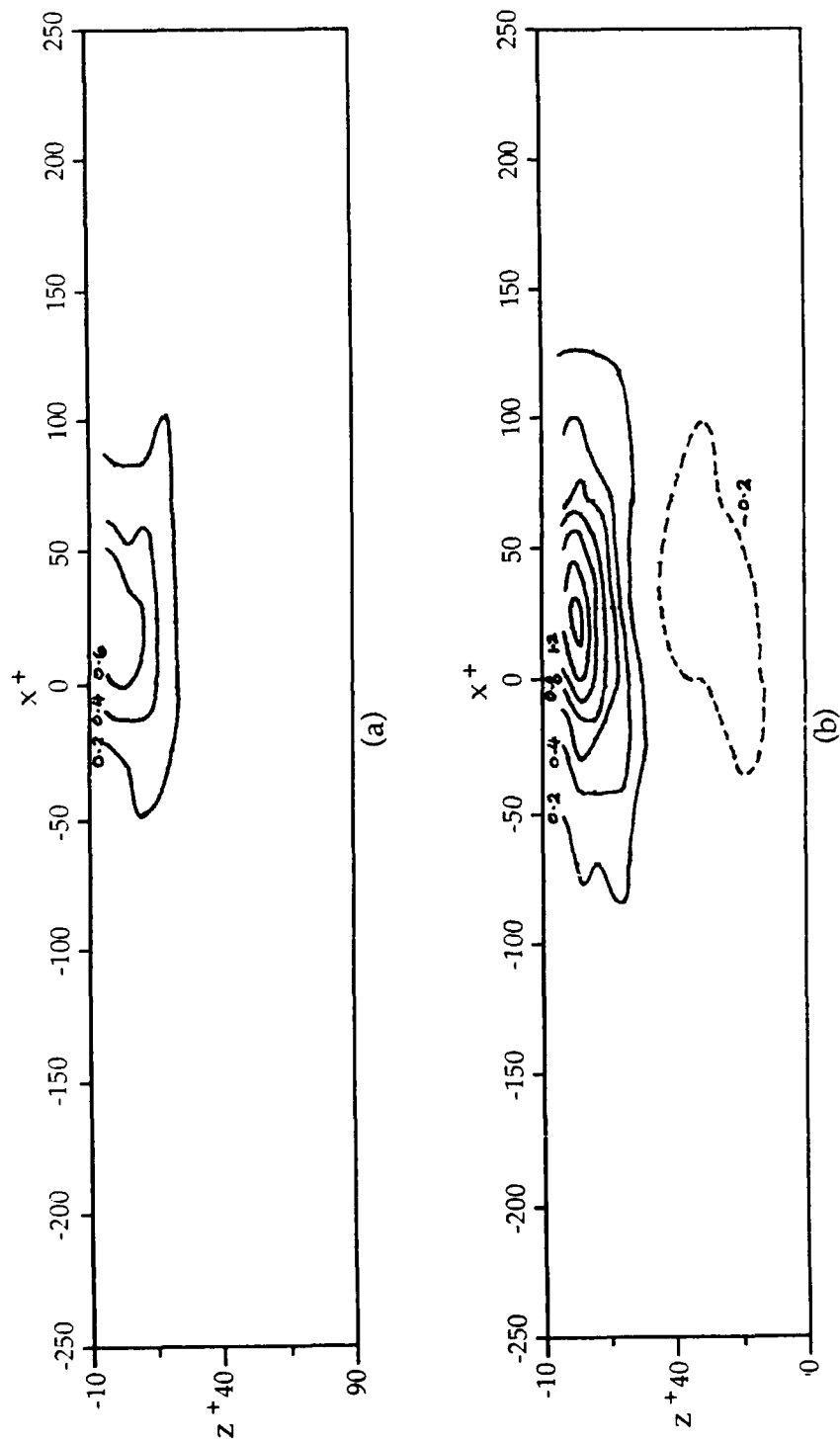


Figure 3.25 v velocity contours in x - z plane at (a) $y^+ = 20$ and (b) $y^+ = 35$. Contour increments of 0.2.

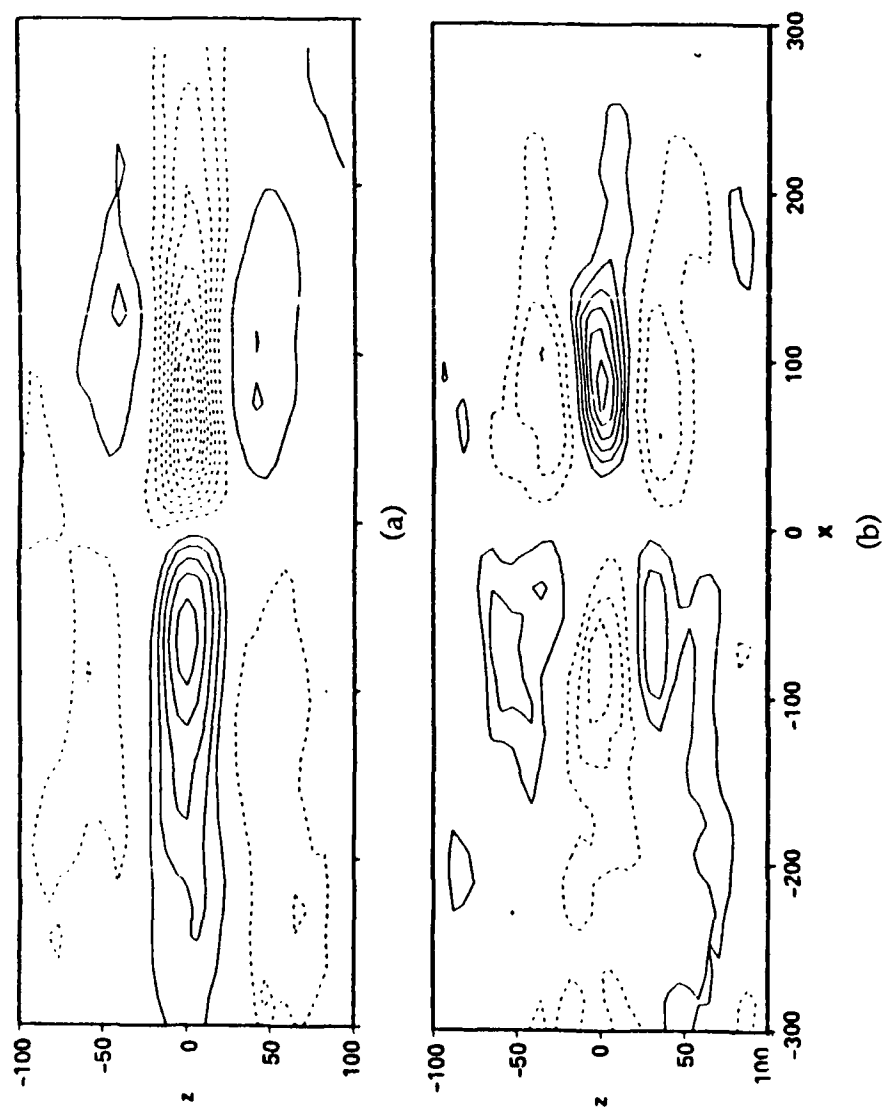


Figure 3.26 Ensemble averaged VISA events of Johansson, Alfredsson & Kim (1987) in the x - z plane at $y^+ = 15$. (a) u contours in increments of 0.5. (b) v contours in increments of 0.1.

more commonly used by other workers. At this threshold, only the strongest bursts were detected. As a consequence of the higher threshold, the average number of conditionally sampled bursts decreased from 200 to 50.

Figure 3.27 shows the v - w vectors from both thresholds at $t^+ = -2$. Although the threshold was increased by a factor of four, the magnitudes of the vectors increased by, at most, 50 percent and the size of the vortical structure is the same. A comparison of the fluctuating u velocity contours in Figure 3.28 also shows that the size of the low speed region associated with the burst is the same, but the magnitudes have increased somewhat with threshold. Both the magnitude and size of the high speed region, however, have increased. The same trend is evident with the fluctuating v velocity contours in Figure 3.29. As Figure 3.30 shows, at the higher threshold, the high speed region appears to be getting under the burst, and may indicate a possible causal relationship where the high speed fluid is displacing the burst by pushing it away from the wall.

Figure 3.31 shows uv product contours at the two thresholds. The maximum magnitude at the higher threshold is about 1.5 to 2 times greater than that at the lower threshold. The size of the structure, however, is the same. The results here indicate that the physical size of the burst and the vortical structure associated with it are independent of the threshold used in the burst detection.

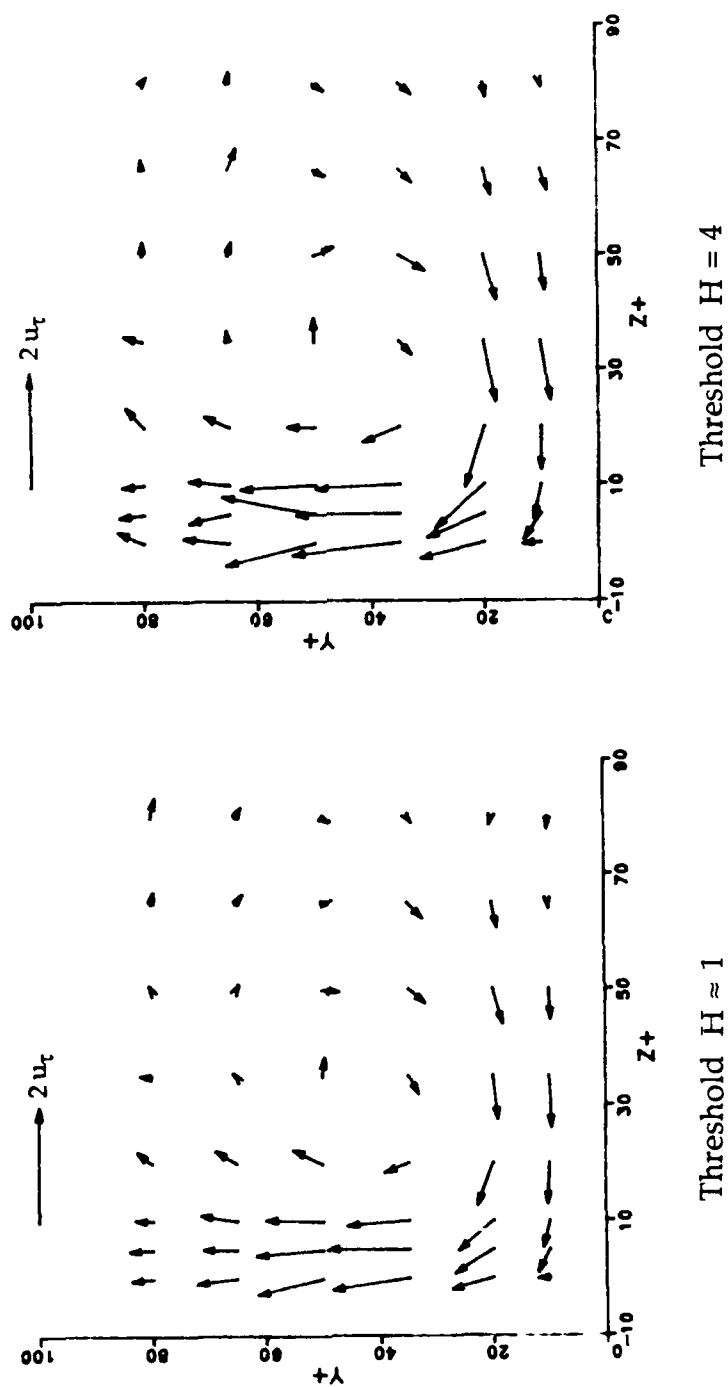


Figure 3.27 v - w velocity vectors at $t^+ = -2$, and at different ejection detection thresholds.

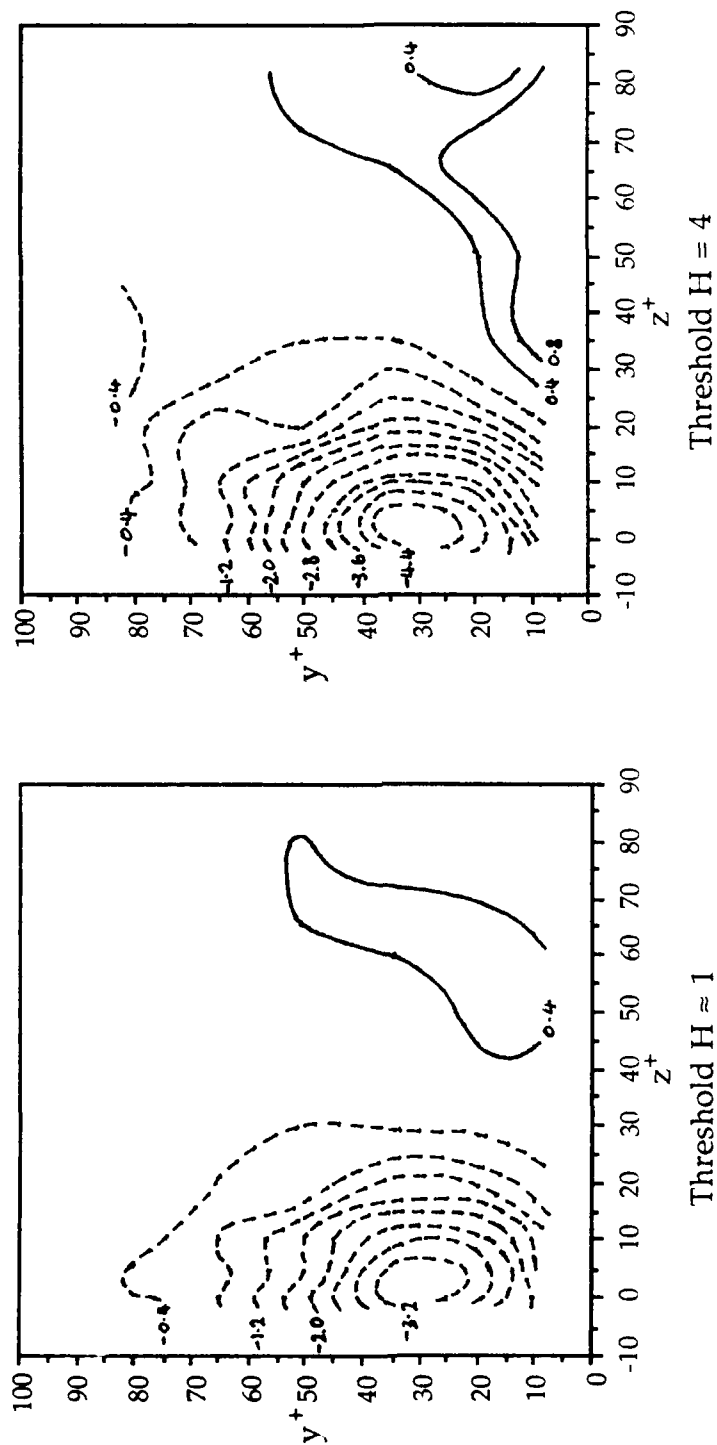


Figure 3.28 u velocity contours at $t^+ = -2$, and at different ejection detection thresholds. Contour increments of 0.4.

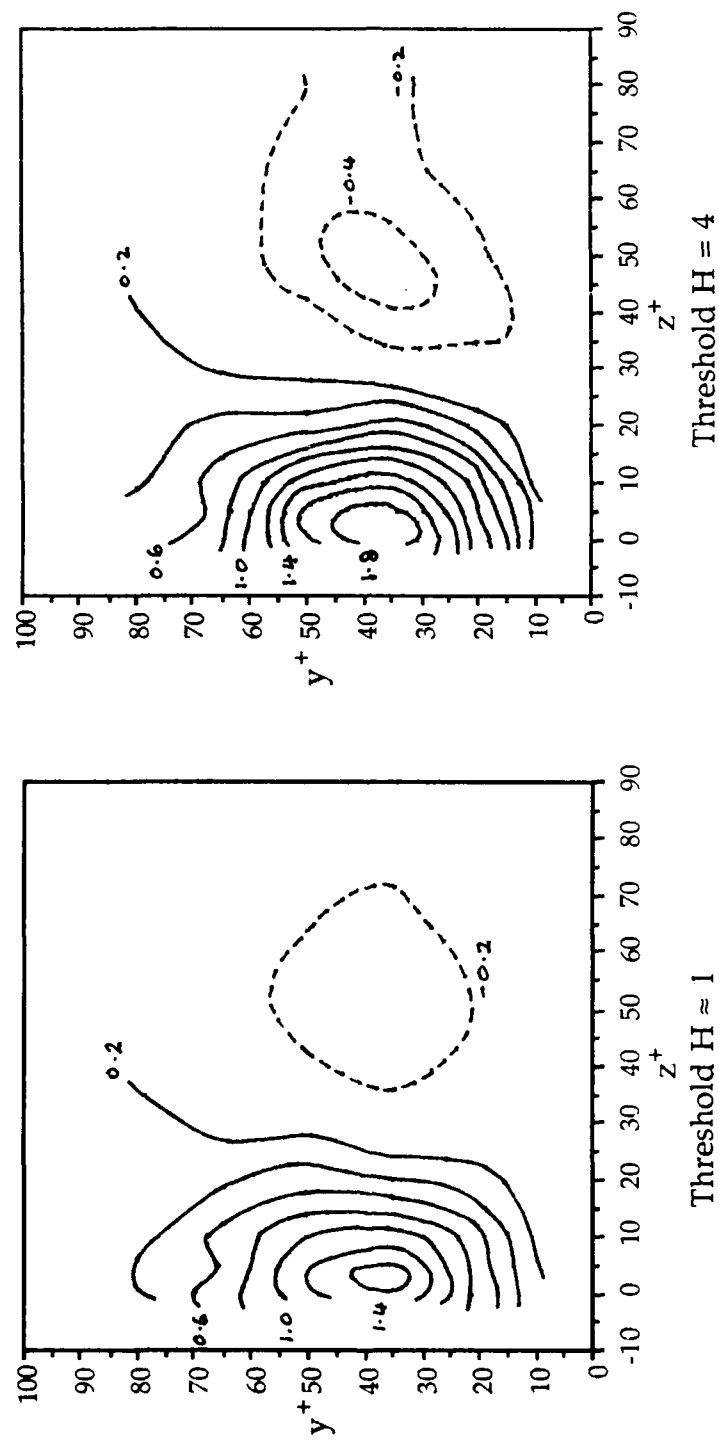


Figure 3.29 v velocity contours at $t^+ = -2$, and at different ejection thresholds. Contour increments of 0.2.

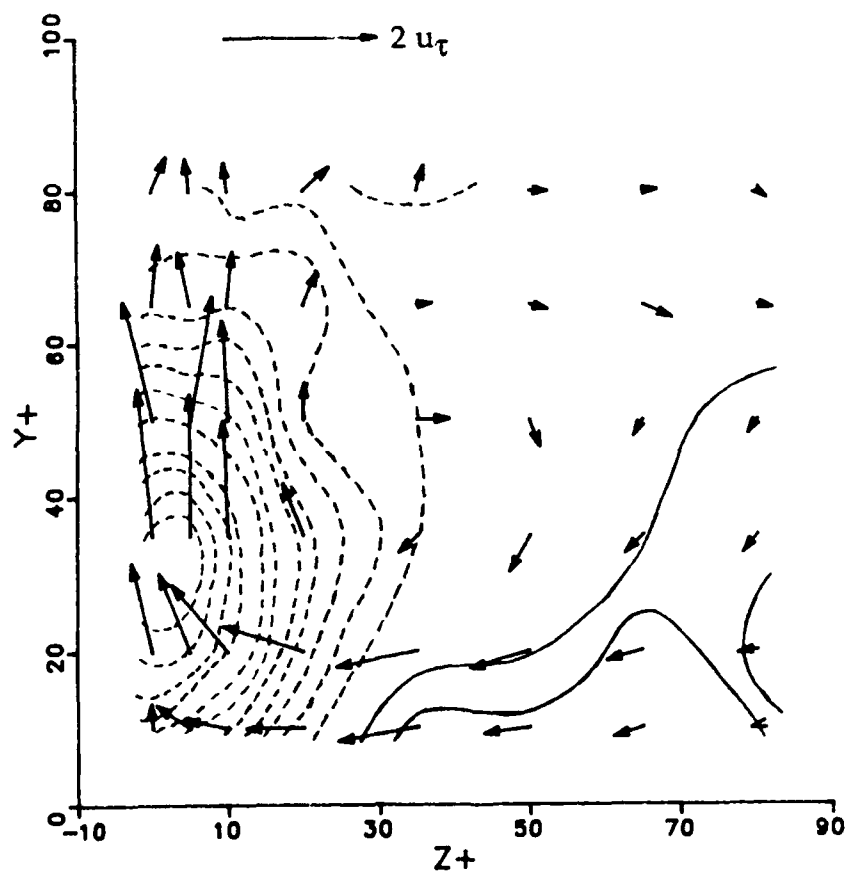


Figure 3.30 v - w velocity vectors and u velocity contours in the y - z plane at $t^+ = -2$, $H = 4$. Contours in increments of 0.4.

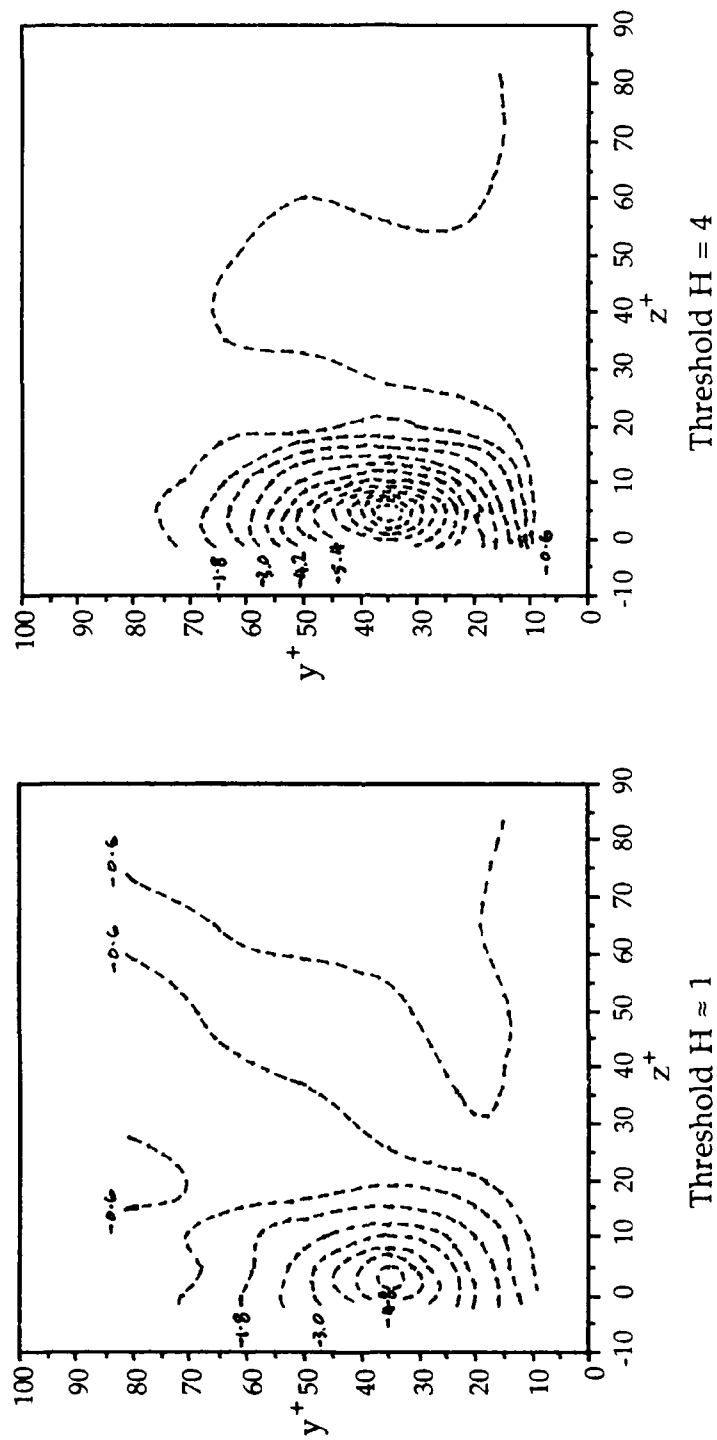


Figure 3.31 uv product contours at $t^+ = -2$, and at different ejection detection thresholds. Contour increments of 0.6.

Figures 3.32 to 3.34 show the u , v and uv contours in the x - y plane at $z^+ = 5$. Compared to the structures at the lower threshold in Figures 3.18, 3.21 and 3.22, respectively, not only have the levels increased, but the streamwise extent of the corresponding contour levels indicate that the structures are also longer by 1.5 to 2 times. The extent of the structures in the y direction has, however, remained the same.

Figures 3.35 and 3.36 show the u and v contours in the x - z plane at $y^+ = 20$ and 35. Both the burst structure and high speed region have increased in length and in intensity, but, as seen in the y - z plane, the spanwise extent is the same as that at the lower threshold. The difference in the physical size between the strong bursts and the weaker ones seems to be only in the streamwise direction.

3.4 Conditional sampling with phase alignment at the mapping point

The results in the previous sections were obtained from conditional samples phase-aligned with the maximum magnitude $(uv)_2$ of the burst at the detection point. In this section, results from conditional samples phase-aligned with the maximum magnitude uv at the mapping point during the burst are presented. Because of phase jitter, the characteristics of the conditionally sampled structures may be smeared, especially further away from the detection point. By phase-

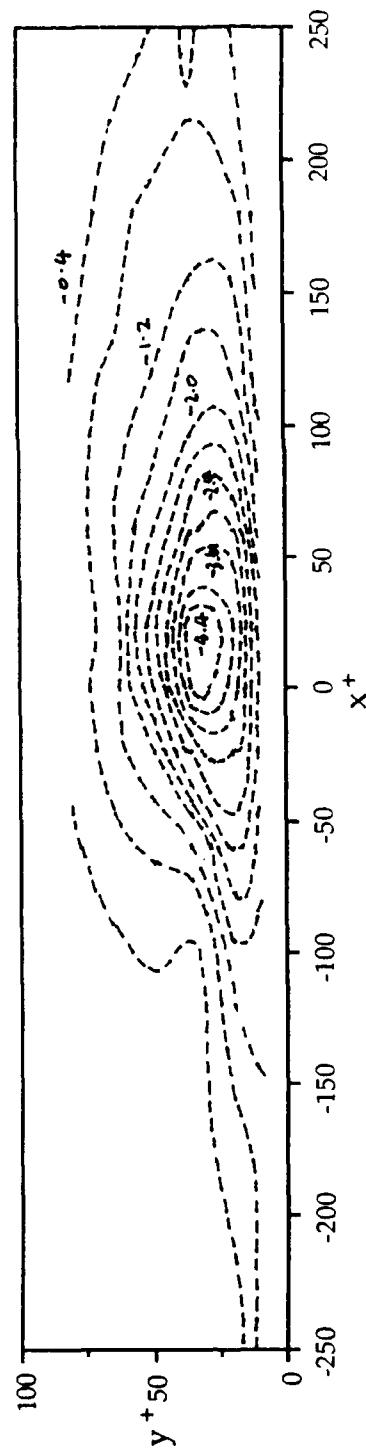


Figure 3.32 u velocity contours in the x - y plane at $z^+ = 5$ with $H = 4$, in increments of 0.4.

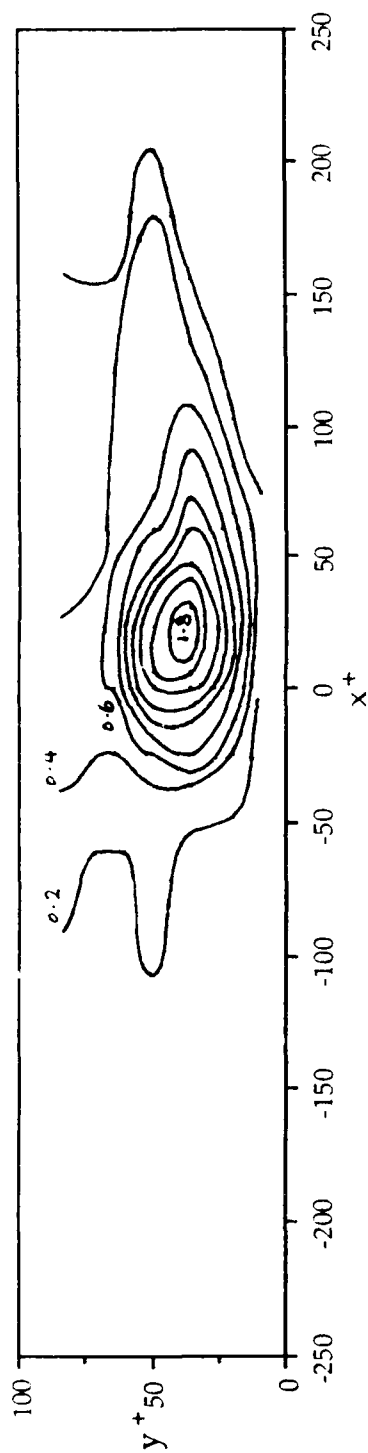


Figure 3.33 v velocity contours in the x - y plane at $z^+ = 5$ with $H = 4$, in increments of 0.2.

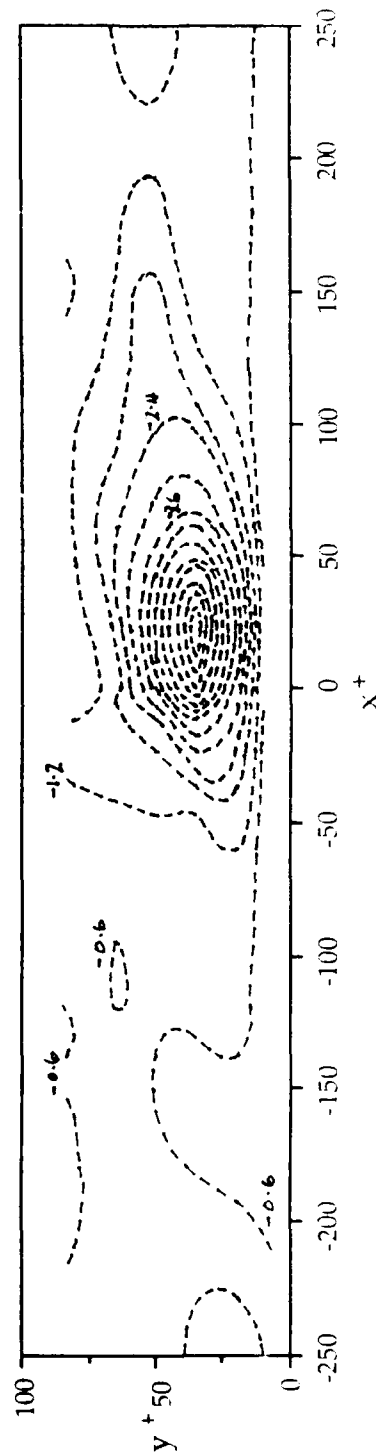


Figure 3.34 uv product contours in the x - y plane at $z^+ = 5$ with $H = 4$, in increments of 0.6.

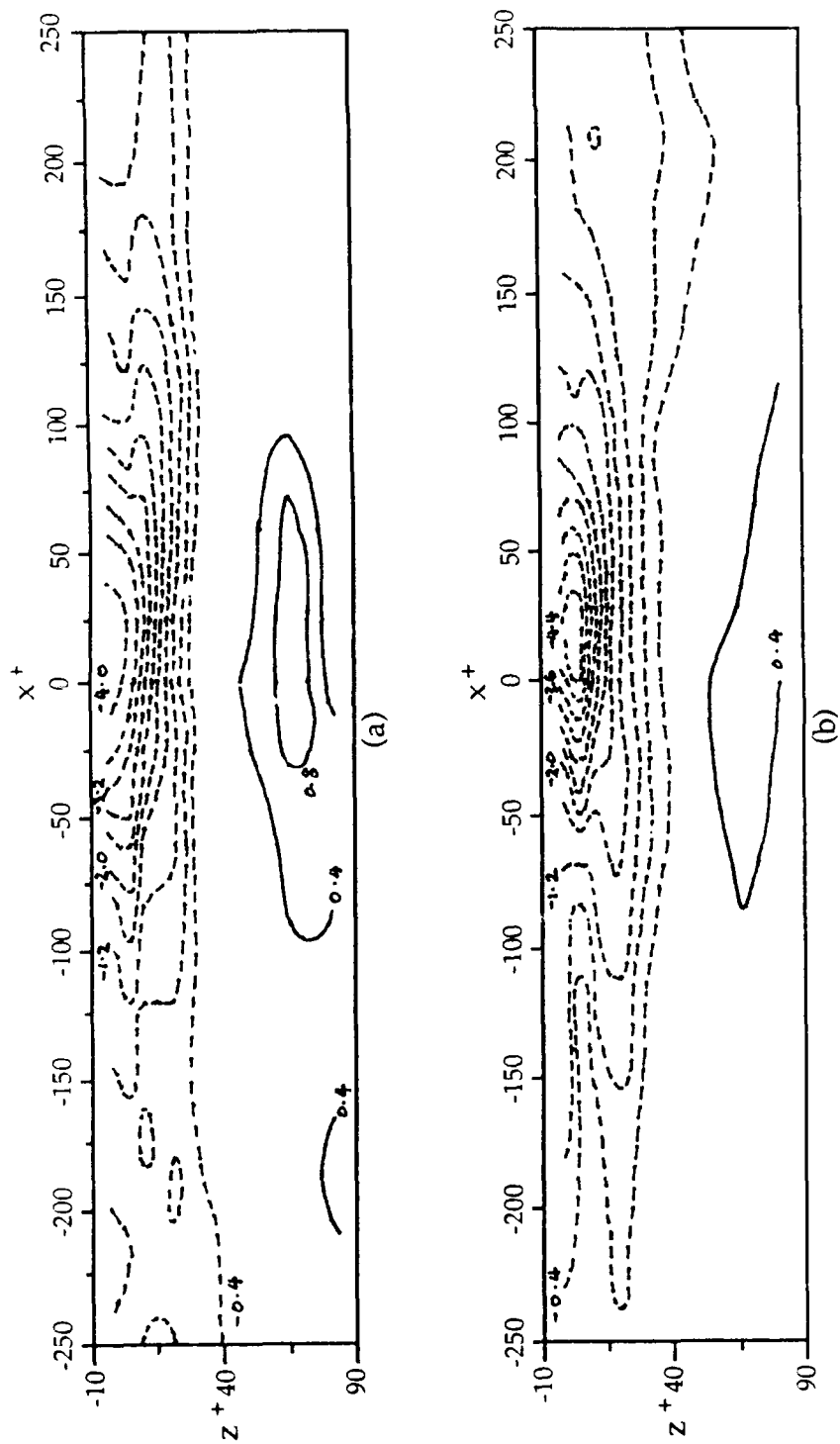
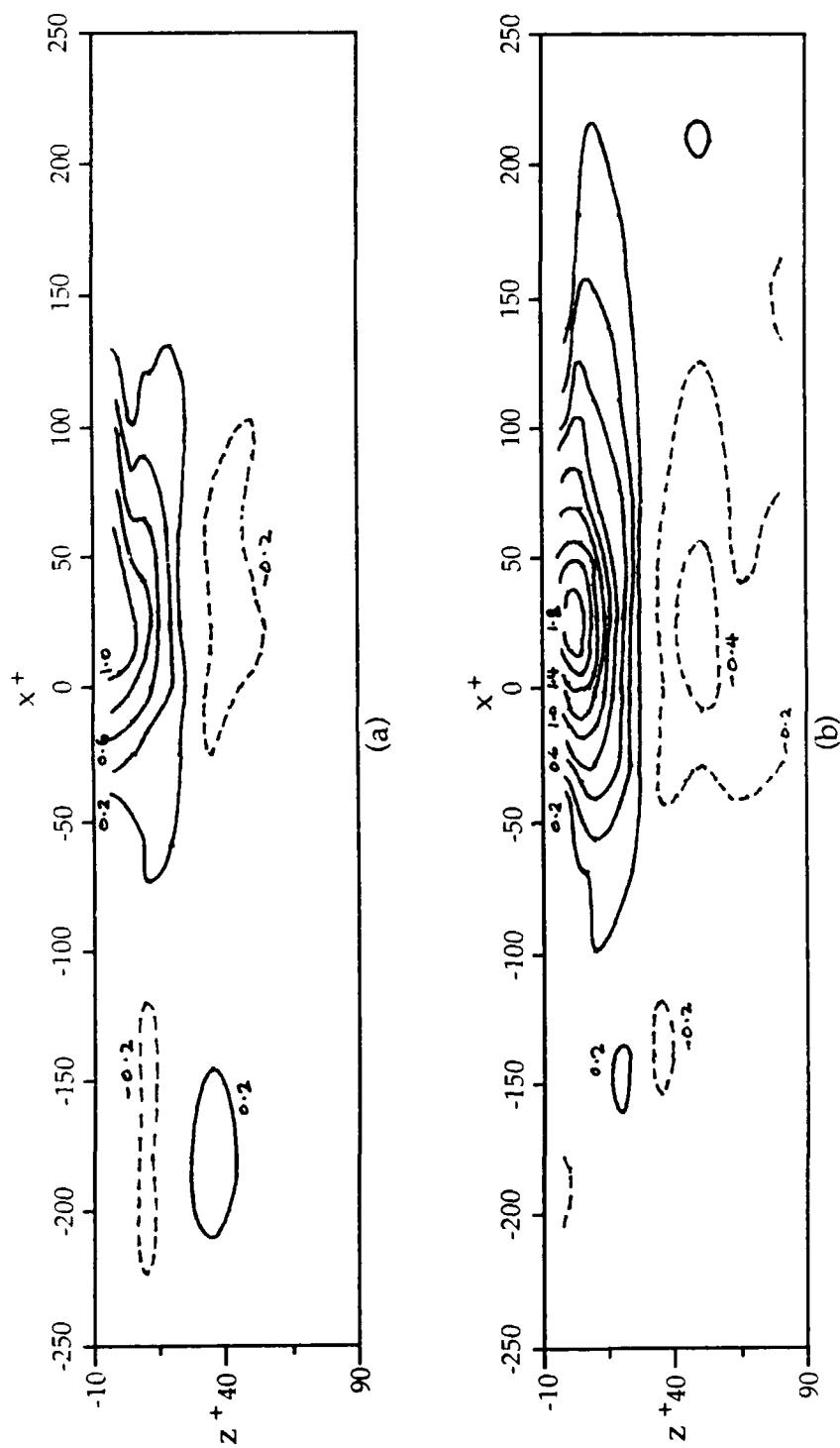


Figure 3.35 u velocity contours in the x - z plane at (a) $y^+ = 20$, and (b) $y^+ = 35$, with $H = 4$. Contour increments of 0.4.



aligning at the mapping point, the characteristics may be enhanced by reducing the effect of the phase jitter.

From the previous results, it was ascertained that the conditionally sampled peak uv magnitude at the mapping point occurred at $t^+ = -2$ with respect to the detection point. For the conditional sampling in this section, a time window was applied around $t^+ = -2$ and the maximum uv magnitude within the window, regardless of quadrant, was located. The conditional samples were then phase-aligned at the maximum uv.

The conditional sampling was done in the x-z plane at $y^+ = 35$ and in the x-y plane at $z^+ = 5$. The appropriate window size was determined by looking at how the size of the window affected the occurrence of the maximum uv in each of the four quadrants at (y^+, z^+) locations of (35,5) and (35,80). As Figure 3.37 shows, within the range of $\pm 2 t^+$ to $\pm 5 t^+$ the occurrence of the maximum uv in each of the quadrants is fairly constant, indicating that the occurrence is independent of the window size. Based on this, a window of $\pm 3 t^+$ was selected.

The effect of phase alignment at the mapping point as compared to phase alignment at the detection point may be seen in Figure 3.38(a)-(e). At each of the mapping locations shown in Figure 3.38, the uv signal shows a distinct peak when phase-aligned at the mapping point, but there is little difference in the u, v and w ensemble averaged

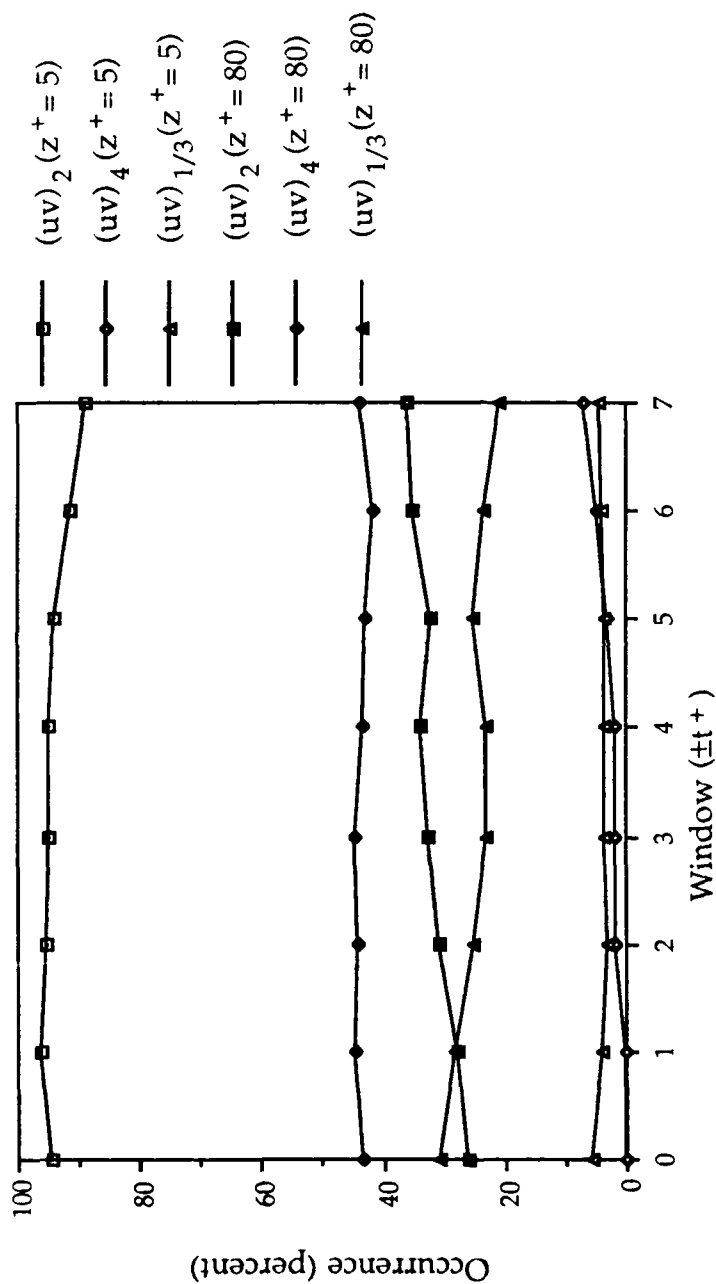


Figure 3.37 Dependence of quadrant detections on window size.

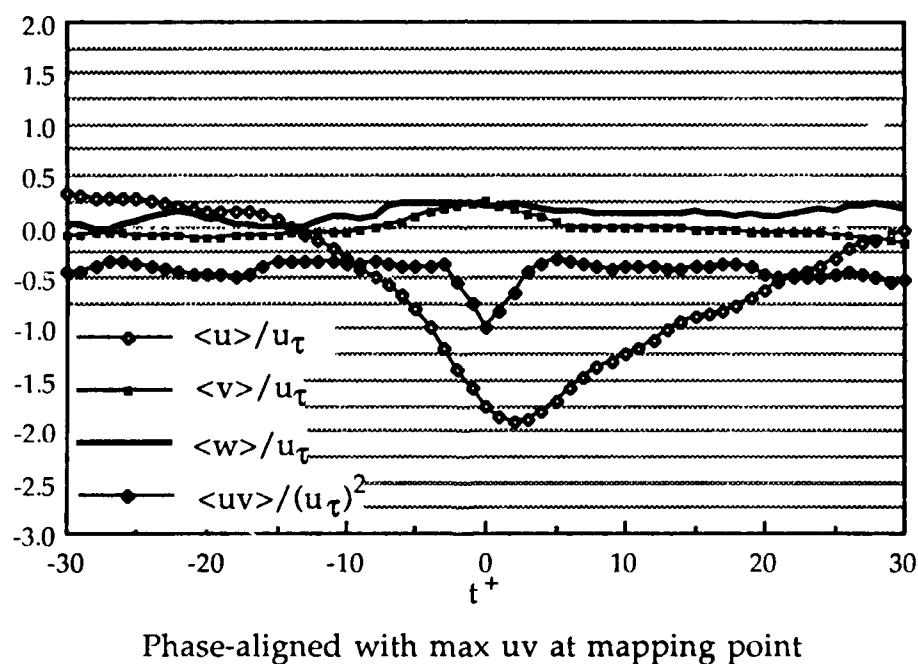
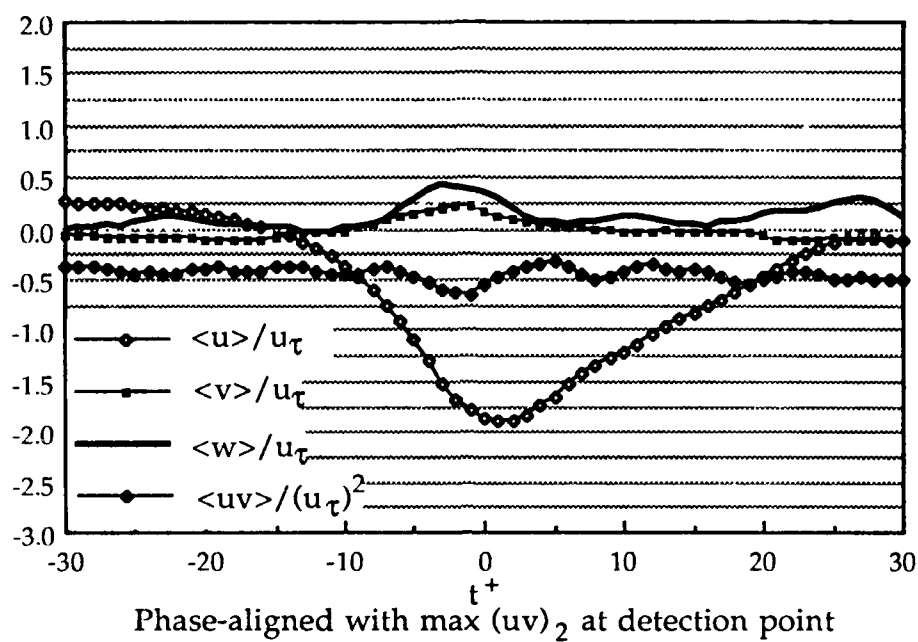
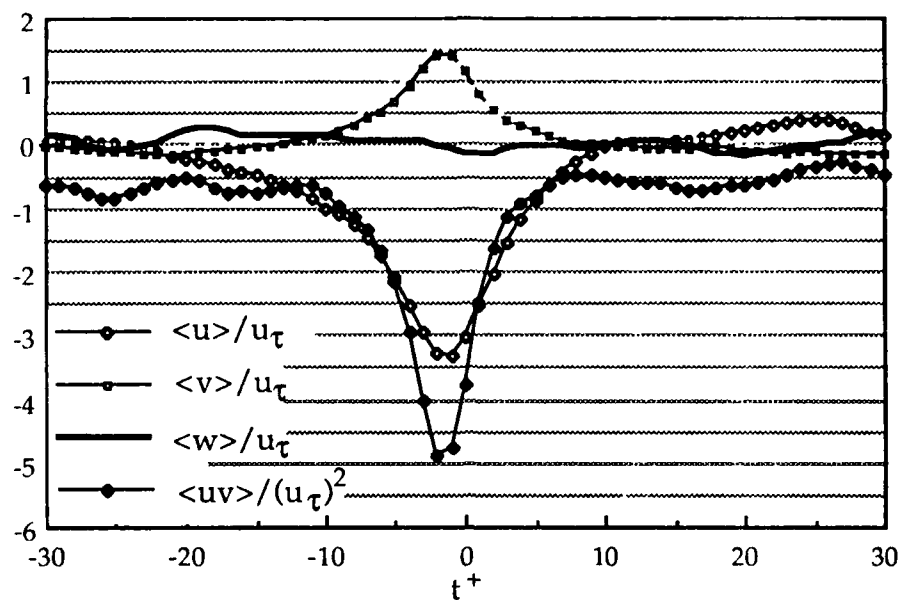
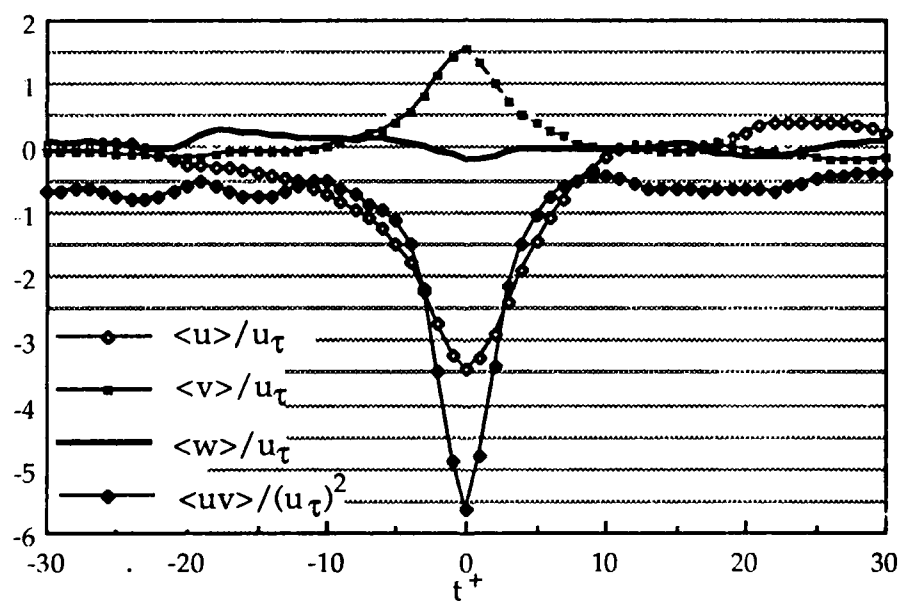


Figure 3.38(a) Ensemble averaged conditional samples at $y^+ = 10, z^+ = 5$.



Phase-aligned with $\max (uv)_2$ at detection point



Phase-aligned with $\max uv$ at mapping point

Figure 3.38(b) Ensemble averaged conditional samples at $y^+ = 35, z^+ = 5$.

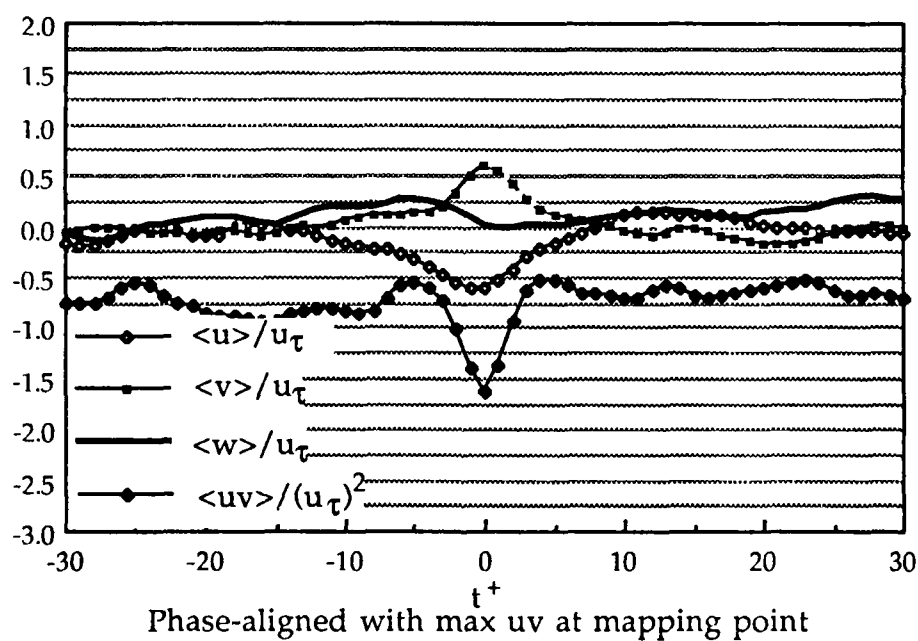
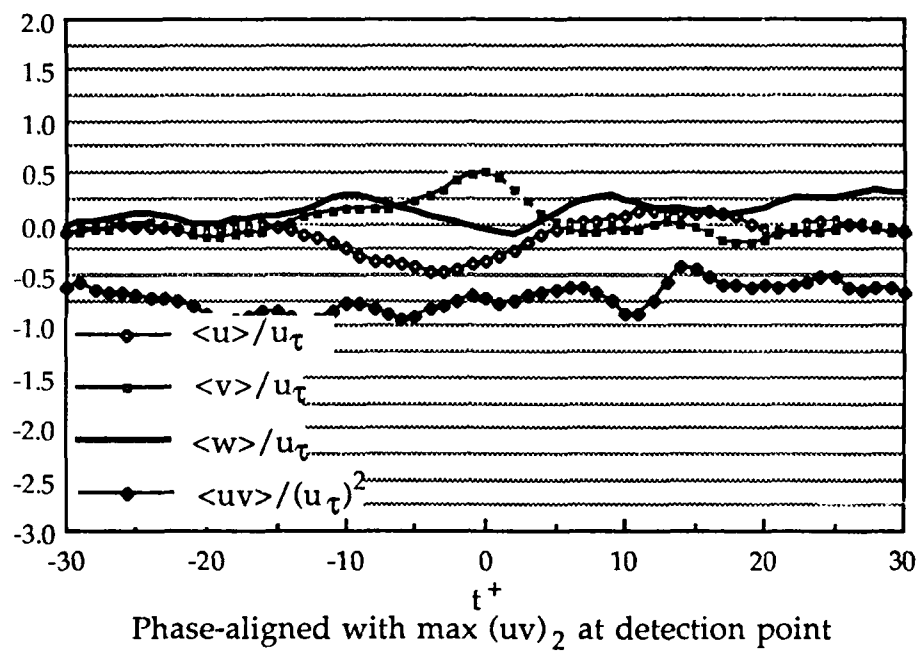


Figure 3.38(c) Ensemble averaged conditional samples at $y^+ = 80, z^+ = 5$.

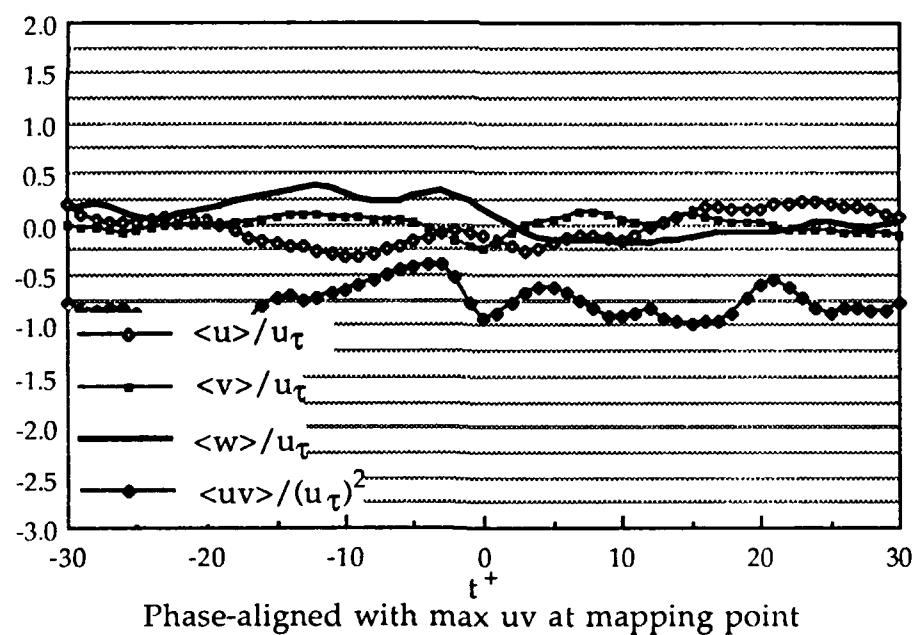
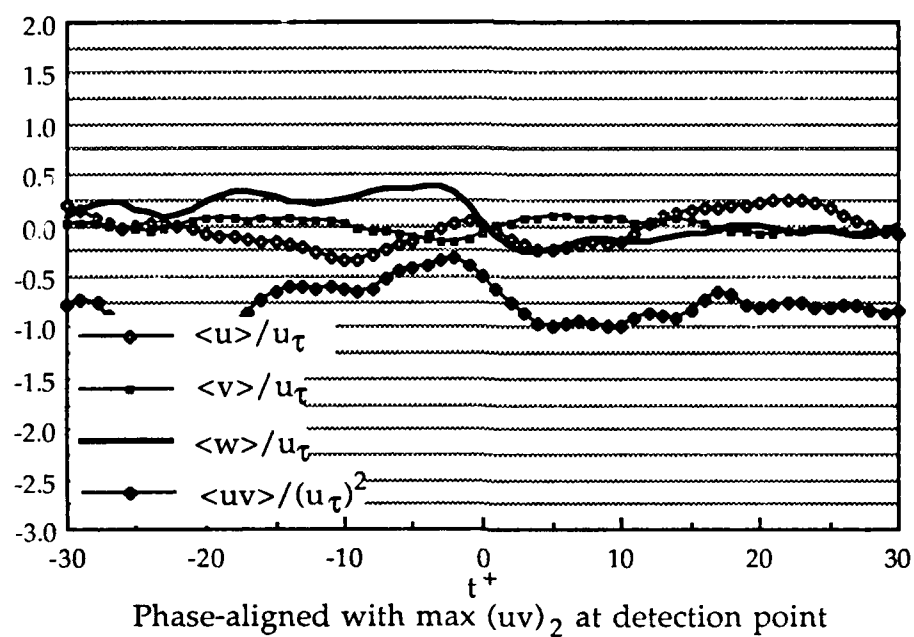


Figure 3.38(d) Ensemble averaged conditional samples at $y^+ = 35$, $z^+ = 35$.

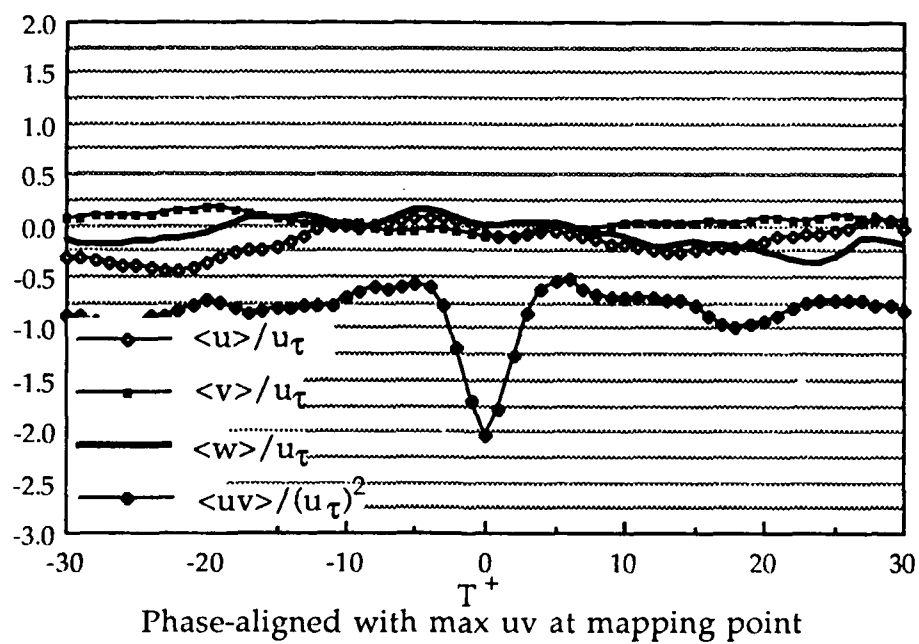
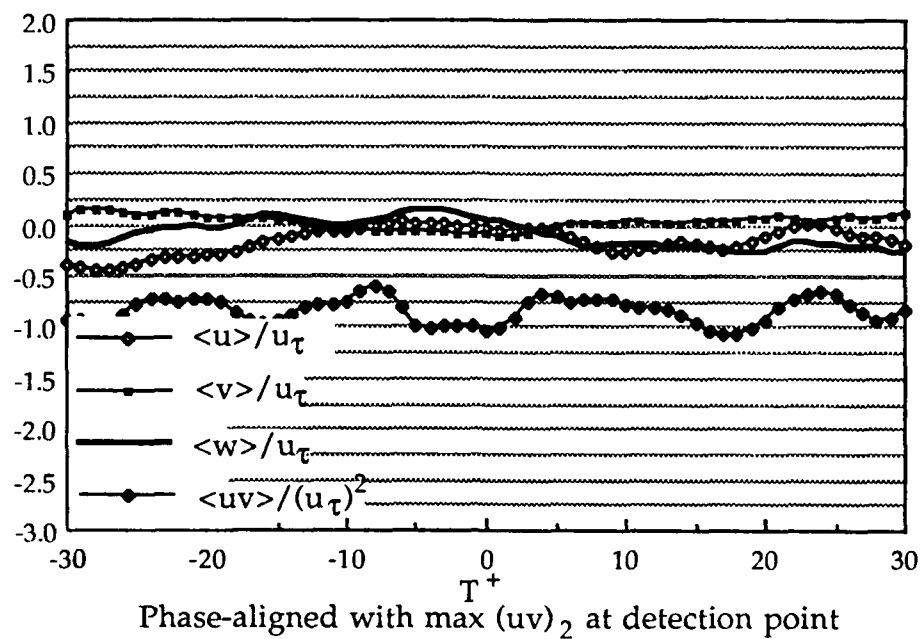


Figure 3.38(e) Ensemble averaged conditional samples at $y^+ = 35$, $z^+ = 80$.

conditional samples. This indicates that the structure is not significantly affected by phase jitter.

The percentage of discrete quadrant occurrences in the spanwise direction at $y^+ = 35$ and in the wall-normal direction at $z^+ = 5$ is shown in Figure 3.39. In the spanwise direction (Figure 3.39(a)), as z^+ increases, the percentage of $(uv)_2$ occurrences decreases from 95% to a minimum of 23% at $z^+ = 65$. The percentage of $(uv)_4$ occurrences increases from 0% to a maximum of 52% at $z^+ = 65$.

In the wall-normal direction (Figure 3.39(b)), the percentage of $(uv)_4$ occurrences, and first and third quadrant interactions increases with distance away from the detection point at $y^+ = 30$. However, the dominant detections were $(uv)_2$ occurrences. The maximum percentage of $(uv)_4$ occurrences detected is 22% at $y^+ = 65$ to 80.

3.5 Reynolds number dependence of the size of the vortical structure

Guezennec et al. (1987) obtained the length scale of the vortical structure by integrating the streamwise fluctuating velocity over the height of the structure to get a local fluctuating velocity "displacement thickness". This procedure was done at several spanwise locations and the length scale was taken as the distance from the detection point where the displacement thickness became zero.

Figure 3.40 shows the ensemble average displacement thickness as a function of spanwise location for the present data. The

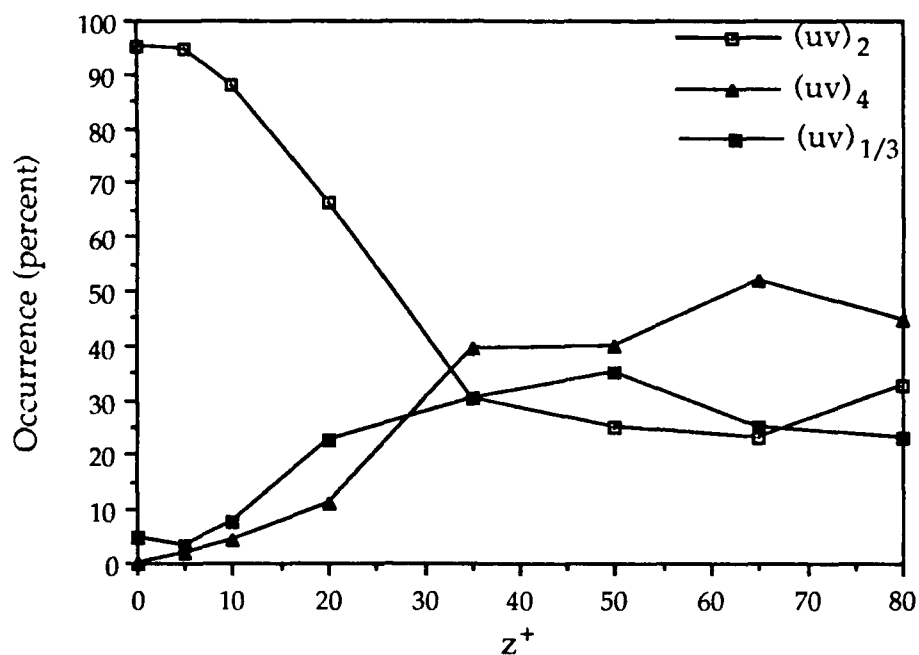


Figure 3.39(a) Quadrant detection in the spanwise direction at $y^+ = 35$.

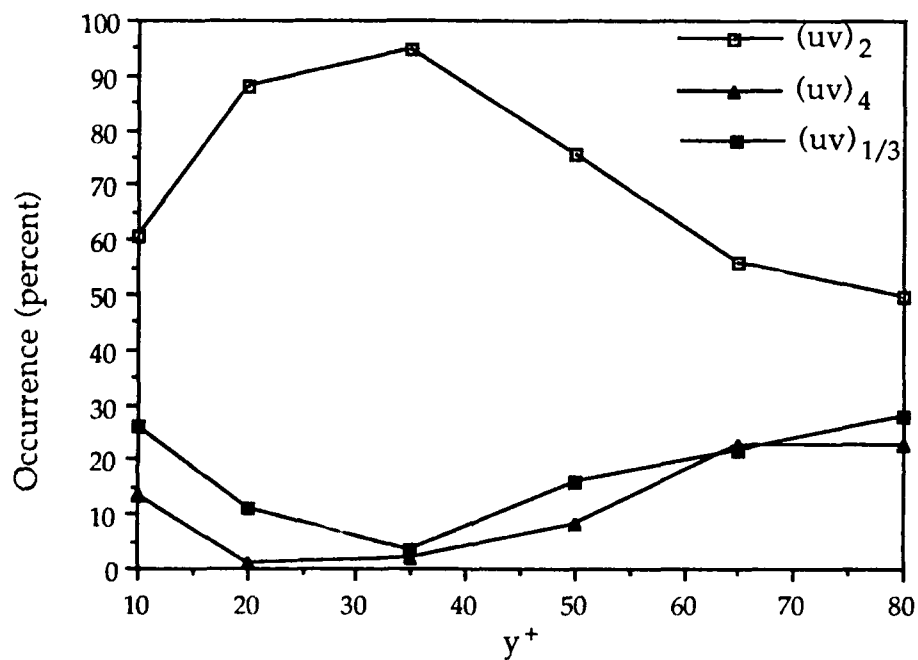


Figure 3.39(b) Quadrant detection in the wall-normal direction at $z^+ = 5$.

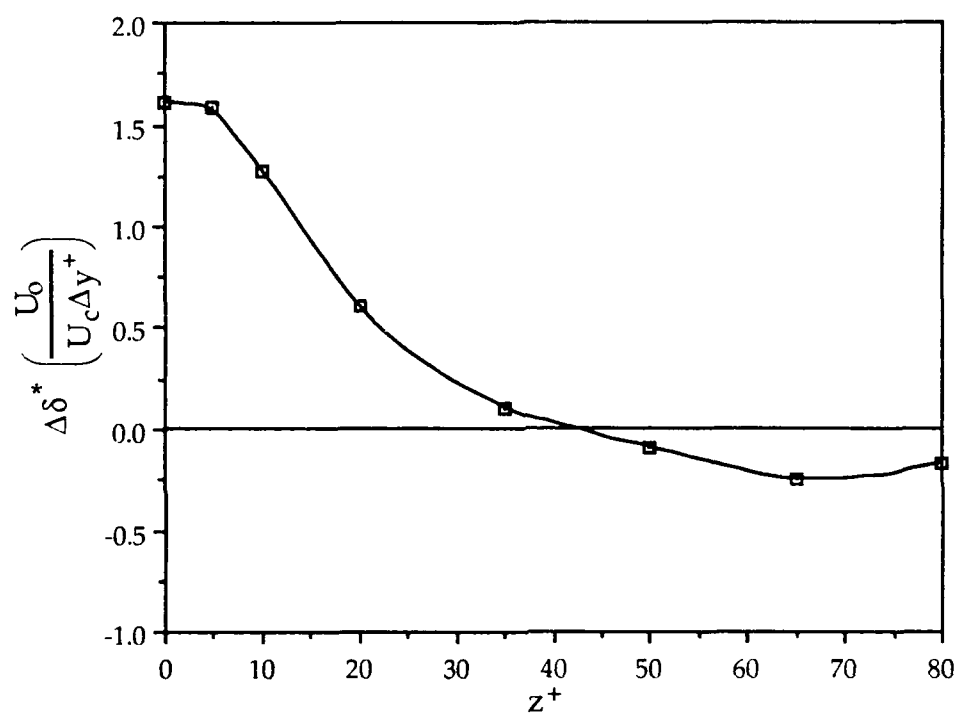


Figure 3.40 Variation of ensemble average displacement thickness as a function of spanwise location.

displacement thickness is equal to zero at $z^+ \approx 42$. Since the detection point was at $z^+ = 5$, the length scale of the vortical structure is $l^+ \approx 37$. This length scale is compared to the data of Guezennec et al. and Wark et al. in Figure 3.41. Guezennec et al. proposed that the size of the vortical structure increases with Reynolds number. The length scale of the vortical structure in the present data is about the same as that of their low Reynolds number data, and indicates an inconsistency with their proposal.

3.6 Probability distribution of w velocity near the wall

To determine the presence of a single dominant vortex associated with the burst, the distribution of w velocities near the wall at (y^+, z^+) locations of (10,35) and (20,35) were obtained. At these locations the ensemble averaged conditional samples showed a strong w velocity towards the detection point (-w). If a single dominant vortex was associated with the burst, a bimodal distribution of the w velocity would be expected. The two peaks would both be -w, with the peak at the more negative w corresponding to the dominant vortex, and the peak at the less negative w corresponding to the weak side vortex.

The w velocity distribution was obtained by determining the w velocity at $t^+ = -2$. To establish the significance of the distribution, a distribution of uncorrelated data was obtained. As Figure 3.42 shows,

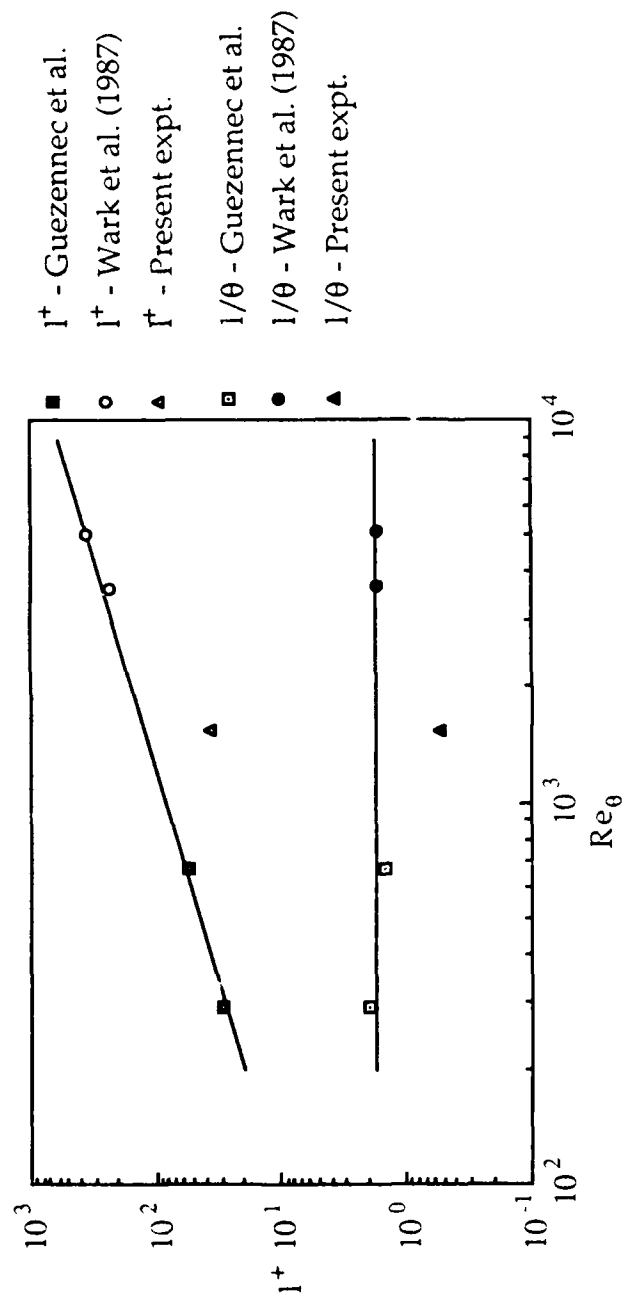


Figure 3.41 Reynolds number dependence of vortical structure size.

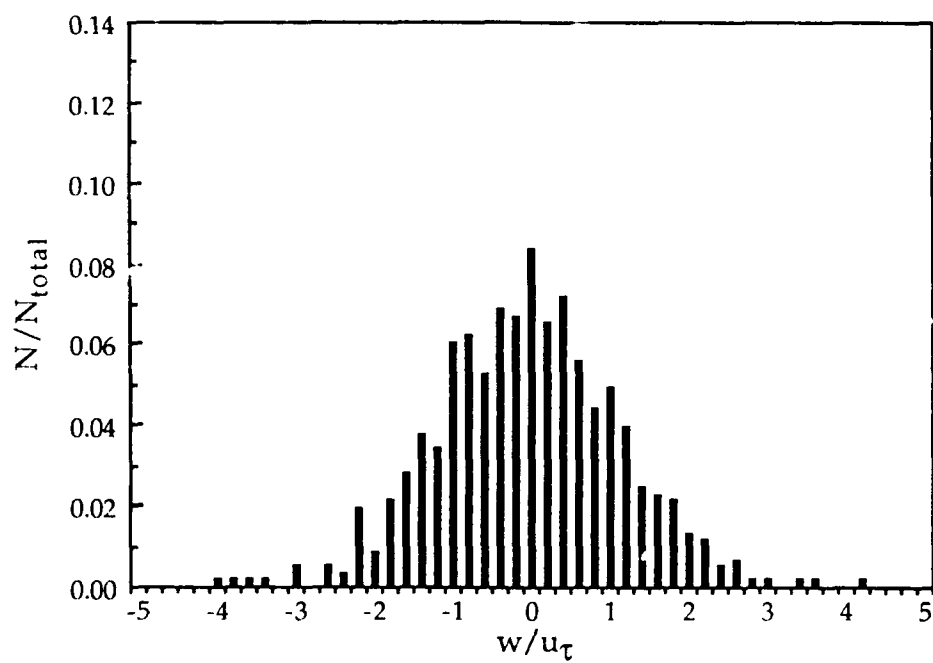


Figure 3.42 Distribution of w velocities at $y^+ = 10$ for uncorrelated data.

the distribution is symmetrical about $w = 0$. The distributions at the two locations are shown in Figure 3.43 and 3.44. Although the distributions are biased to the negative side, a distinct bimodal distribution on the negative side is not evident. A bimodal distribution would have indicated the presence of a dominant vortex, but the absence of such a distribution does not necessarily mean that the vortices are of equal strength because the instantaneous vortices occur in random locations and sizes. Since the conditional sampling was not phase-aligned in the spanwise direction, phase jitter may be responsible for the smearing of the distribution so that only one peak is present. Thus, a single peak in the probability distribution of w does not negate the possibility of there being a single dominant vortex.

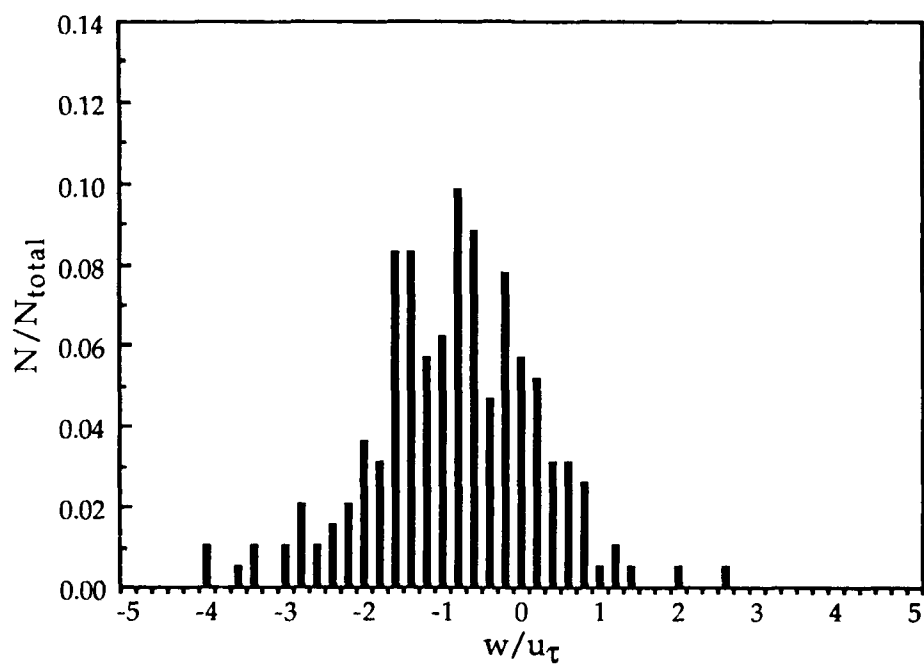


Figure 3.43 Distribution of w velocities at $y^+ = 10$, $z^+ = 35$.

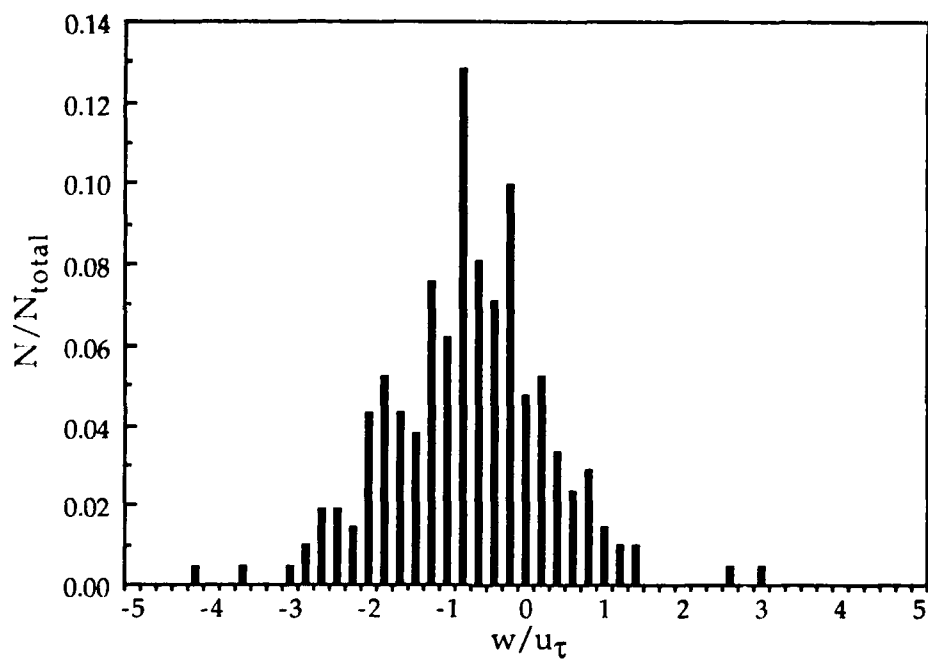


Figure 3.44 Distribution of w velocities at $y^+ = 20$, $z^+ = 35$.

CHAPTER 4

CONCLUSIONS

4.1 Summary and conclusions

The presence of a streamwise vortical structure associated with the burst has been verified by directly mapping the flow field. The vortical structure had a spanwise extent of $z^+ \approx 75$ with its center between $y^+ = 35$ and 50 during the strongest part of the burst. It was also found to be inclined to the wall.

In the x-y plane, the results showed a transverse rotational motion associated with the burst structure when viewed with a constant convection velocity. However, such a motion was not evident from the plot of the fluctuating velocity vectors. The conditional samples also showed an elongated structure with a steeper velocity gradient at the trailing edge than at the leading edge, and which was strongly uplifting between $y^+ = 20$ and 50.

The spanwise and wall-normal extents of both the vortical structure and the burst were found to be independent of the detection threshold used, although the magnitudes of the velocity components of the vortex and burst increased slightly, as would be expected. The

streamwise extent of the burst, however, increased with threshold. That is, stronger bursts are longer than weaker ones.

The results also indicated that the spanwise extent of the vortex is inconsistent with the proposal that it is dependent on Reynolds number.

Conditional sampling with phase alignment at the mapping point indicated that the ensemble averaged conditional samples were not significantly affected by phase jitter. Also, there were fourth quadrant occurrences side by side with bursts about 50 percent the time. The probability distribution of the w velocity in the near wall region and to the side of the burst detector was investigated to verify the existence of the dominant vortex, but the result was inconclusive.

Although the presence of bursts and streamwise vortices has been established together with their spatial relationships, a causal relationship between them still has yet to be determined.

4.2 Recommendations for future work

The analyses performed on the data acquired in this study constitutes only a part of what can be done with the data. The conditional sampling in this study was done using only one detection scheme and phase-alignment at one point in the burst. The data could be reanalyzed using other detection schemes such as VITA or u -level. Since different detection schemes base their detection on different

characteristics of the burst, the conditionally sampled flow field associated with the burst may show different characteristics.

Phase-alignment with different parts of the burst, both in the streamwise and spanwise directions, could also be done to get a better sense of how the flow field evolves during the burst. Investigating the vorticity in the flow field will also be helpful in understanding more about the interaction of the flow field with the burst.

A true 3-D mapping of the flow field is also recommended. The same spanwise mapping as this study should be done at other streamwise locations with respect to the detector. With these measurements a true 3-D picture of the burst and the associated vortex can then be obtained, rather than a pseudo 3-D one obtained by using a convection velocity.

A more detailed analysis of sweeps and their relationship with bursts should also be done. Studies by Nagib & Guezennec (1986) and Komori et al. (1989) indicate that bursts and sweeps occur in succession, while the work of Wark (1988) and Robinson et al. (1988) indicates they occur side by side. With a true 3-D mapping, this point could be resolved.

APPENDIX A

FIBEROPTIC LDV DEVELOPMENT AND LDV SETUP

A.1 Fiberoptic LDV development

Velocity measurements were made from below the water channel facility. Because of space constraints, a small compact LDV system was required to fit below the channel. A system of lenses and mirrors to transmit the laser to the LDV would have been cumbersome and difficult to align. Using optical fibers to transmit the laser light to and from the LDV was the logical alternative. Compared to a system of mirrors and lenses the fiberoptic system was compact, self-contained and portable.

The decision to build the FOLDV rather than to buy a commercial system was based on cost, on the flexibility in designing a system which met all our specifications, and on the possibility of building a traversing system from the cost savings. The cost of the FOLDV was \$6,000 and that of the traversing system was \$5,000, while the cost of a commercial system without any traversing system was \$13,000.

In designing the FOLDV there were two constraints to consider. These were:

- a) Existing TSI frequency shifting optics and photomultiplier (PM) tube were to be used.
- b) The probe volume was to be the same size as that of the existing TSI system.

Figure A.1 shows a schematic of the FOLDV. All the components were basically off-the-shelf items from Newport Corporation and Spindler-Hoyer Inc. The holes in the receiving lens were custom-drilled, however. The transmitting optical fiber was a polarization-preserving single mode fiber, and the receiving fiber was a multimode fiber which connected to the PM tube. The main problem was in launching the laser beam into the transmitting fiber because of its very small core diameter of 4 μm . The coupling efficiency was about 30%, which is about what can be expected for a single mode fiber.

A.2 LDV setup

Proper alignment of both LDV systems was essential owing to the data rates which had to be attained to get a continuous time history of the flow. Coincidence of the probe volumes was achieved by operating the LDV's in side scatter mode, using the receiving optics of one system to collect signal from the probe volume of the other system.

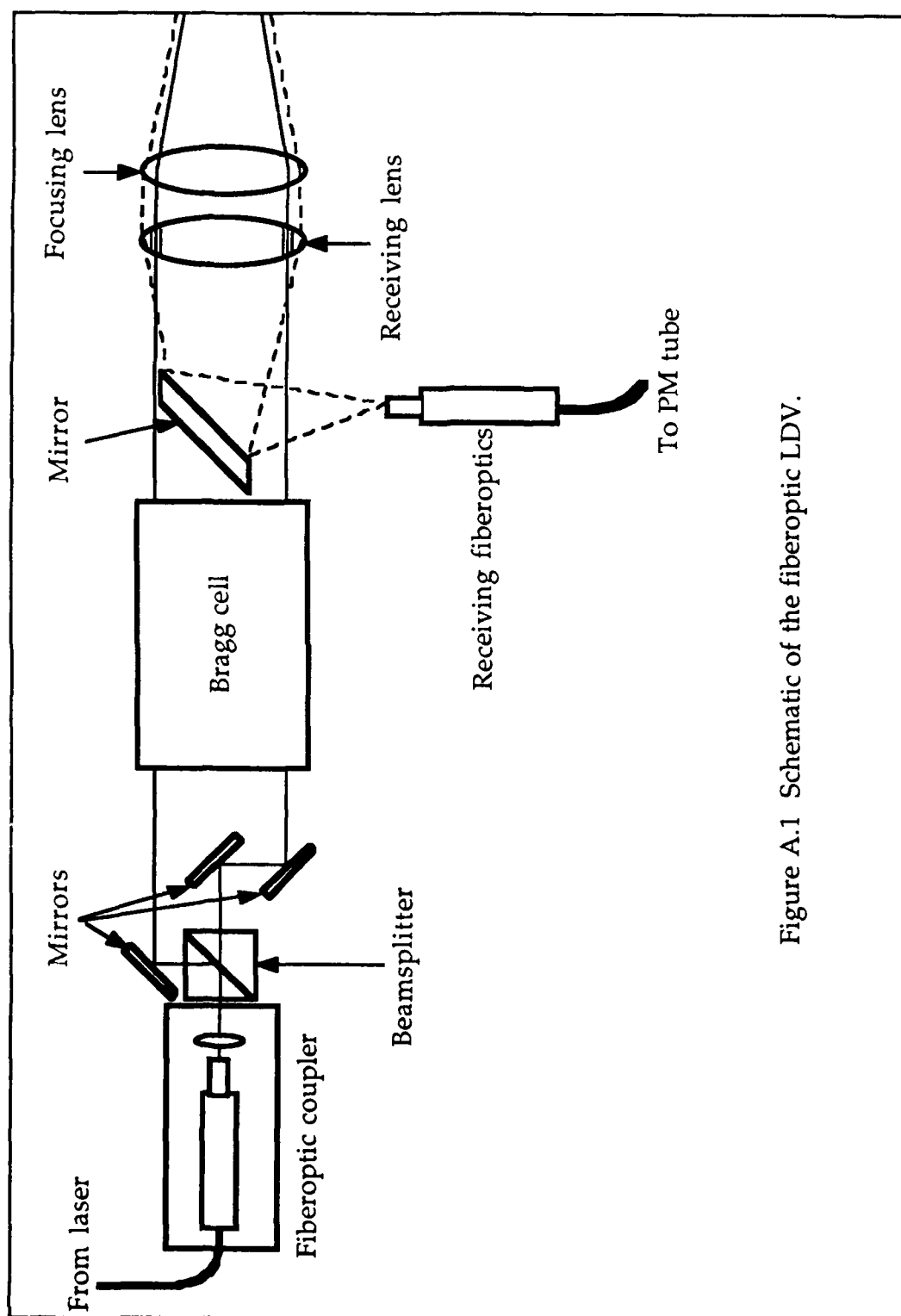


Figure A.1 Schematic of the fiber optic LDV.

The fringe spacing, which is needed in calculating the velocity, was determined from:

$$d_f = \frac{\lambda}{2\sin\psi} \quad (\text{A.1})$$

where λ is the laser beam wavelength, and ψ is the half-angle between the beams. The angle ψ was measured by marking the position of the beams on a sheet of paper placed flat on the water channel wall, and then traversing the LDV system normal to the paper to a different location, noting the distance traversed and marking the new position of the beams. For the beams which were in the plane normal to the tilt of the optics, ψ was calculated from:

$$\psi = \tan^{-1} \left(\frac{\frac{1}{2}(d_1 - d_2)}{x_2 - x_1} \cos \phi \right) \quad (\text{A.2})$$

where d_1 and d_2 are the distances between the beams of the first and second locations, $x_2 - x_1$ is the distance traversed, and ϕ is the angle of tilt of the optics. For the beams which were in the plane of the tilt, ψ was calculated iteratively from:

$$\tan(\phi + \psi) - \tan(\phi - \psi) = \frac{d_1 - d_2}{x_2 - x_1} \quad (\text{A.3})$$

This procedure was repeated to obtain a set of 30 discrete measurements of ψ . The mean value was obtained with an uncertainty of 0.28% for the TSI system and 0.55% for the FOLDV. The procedure for estimating the uncertainty is discussed in Appendix E.

APPENDIX B

CALIBRATION OF HOT-FILM PROBE

B.1 Procedure

Calibration of the X-type hot-film probe was done in the freestream of the water channel just before, during and immediately after the experiment. As mentioned in Section 2.3, the voltage output of the sensors were recorded for a range of velocities which were measured simultaneously by the LDV. Seven calibration velocity values in the range 0.05 m/s to 0.19 m/s were used.

During the first calibration, the probe was pitched at seven angles over a range of $\pm 24^\circ$ from vertical at the calibration velocity closest to the local mean velocity at $y^+ = 30$. This was done to obtain a "yaw constant" which was used to correct for variations due to different angles of attack of the velocity vectors in the boundary layer. Determination of the yaw constant is discussed in Section B.2.

About 100 seconds of calibration data was taken at each velocity or pitch angle. Such a long calibration time was necessary to obtain consistent mean velocity measurements (Coughran, 1988). To further ensure consistent readings, two readings were obtained at each

calibration velocity or angle. The temperature of the water was also controlled to within $\pm 0.05^\circ\text{C}$.

B.2 Calibration curve and yaw constant

The expression used to relate velocity to the voltage output of a hot-film sensor is given by the fourth-order polynomial:

$$U_e^{1/2} = A + BE^2 + CE^4 \quad (\text{B.1})$$

where U_e is the effective cooling velocity. E is the sensor voltage output, and A , B and C are the calibration constants which are to be determined. Coughran & Bogard (1986) reported that equation B.1 gave a better fit than King's Law. For inclined sensors, the calibration velocity and the effective velocity are related by:

$$U_e^2 = (U_{\text{calib}})^2 (\cos^2 \alpha + k^2 \sin^2 \alpha) \quad (\text{B.2})$$

where U_e is the effective velocity, U_{calib} is the calibration velocity in the mean flow direction, k is the yaw constant, and α is the angle between the normal to the sensor and the mean flow direction. Thus, the calibration velocity is related to the voltage output of an inclined sensor by:

$$(U_{\text{calib}}(\cos^2 \alpha + k^2 \sin^2 \alpha)^{1/2})^{1/2} = A + BE^2 + CE^4 \quad (\text{B.3})$$

For an X-type hot-film probe, the sensors are nominally inclined at 45° to the mean flow direction. A, B and C for each sensor can be solved by using equation B.3 with $\alpha = 45^\circ$, a given value for k , and the data from the seven calibration velocities. A typical calibration curve is shown in Figure B.1. The mean deviation of the curve from the calibration velocities was $\pm 0.4\%$.

A different set of calibration constants was obtained for each value of k which was assumed over a range of k values. The different sets of calibration constants were then plugged in to equation B.1 with the voltage outputs from the seven pitch angles to obtain the effective velocity at those angles. The velocity in the mean flow direction was then obtained from equation B.2, where U_c , k and α were known. The calculated mean flow velocity over the range of pitch angles for the different k values was then compared to the known calibration velocity.

The value of k which gave the minimum sum of squared residuals was taken as the appropriate value for that sensor. Figure B.2 shows the variation of the calculated velocity over the range of pitch angles for different k values. The values of k for each sensor were 0.26 and 0.20 respectively. Figure B.3 shows the variation of the calculated velocity using the appropriate k values for each sensor. At $y^+ = 30$, only about 0.1% of the velocity measurements have angles greater than 20° from the mean flow direction ($\alpha < 25^\circ$, $\alpha > 65^\circ$). Excluding the extreme angles, the deviations of the calculated velocity are less than 2% over

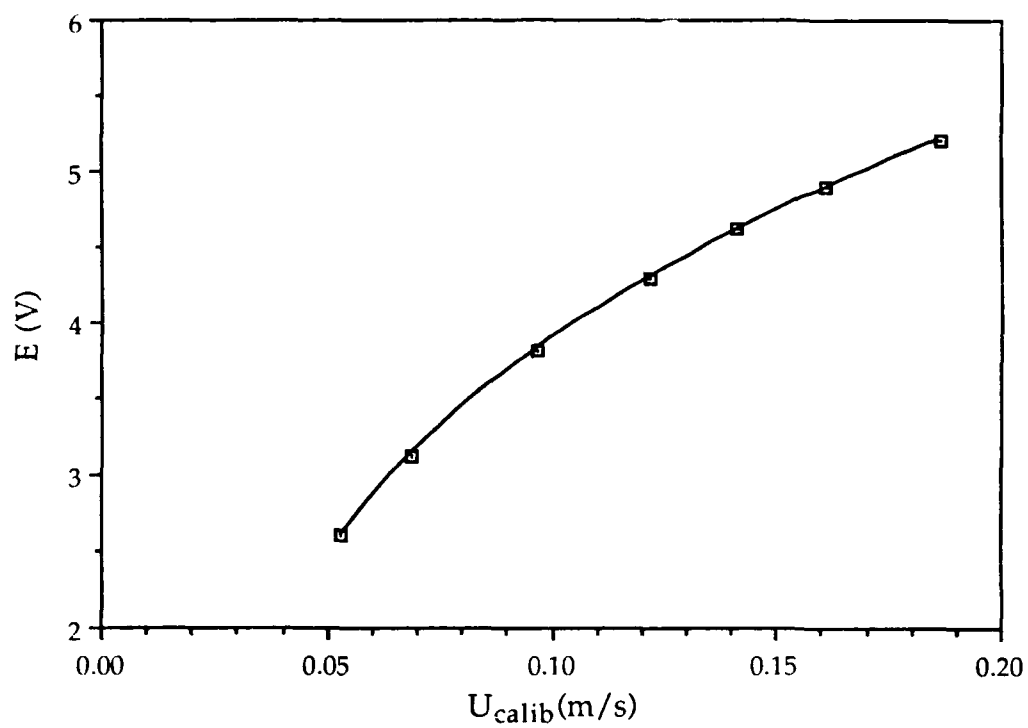


Figure B.1 Typical calibration curve for hot-film sensor.

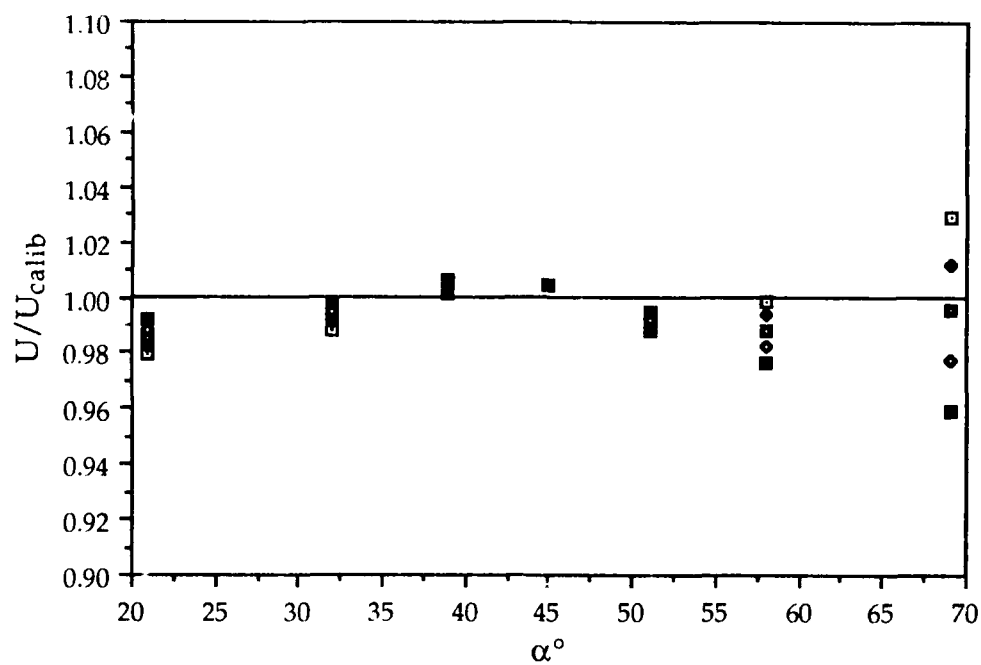


Figure B.2 Calculated velocity at different pitch angles for different yaw constants.

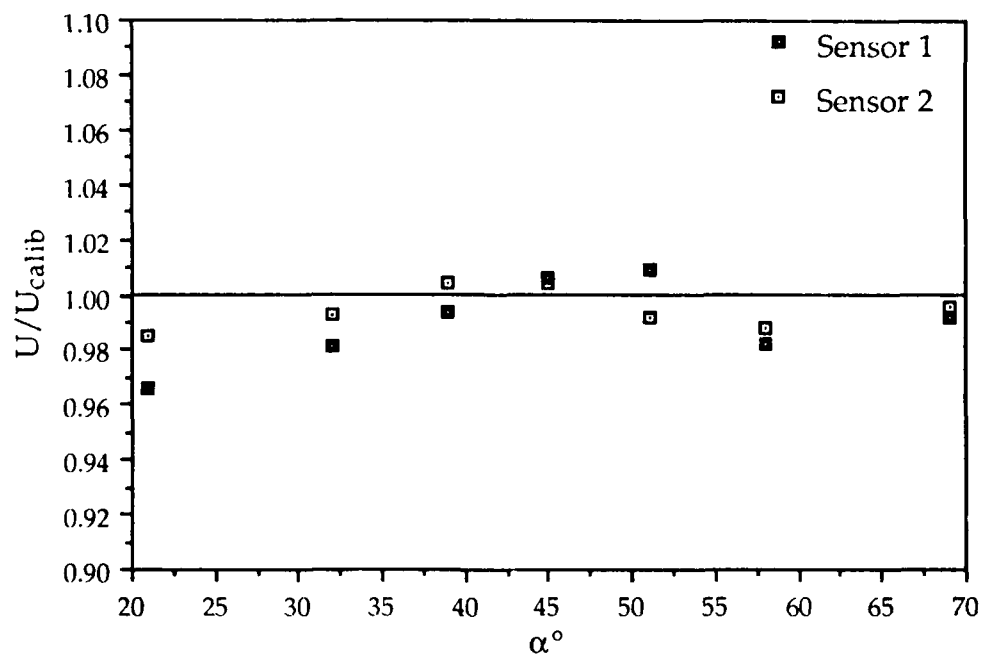


Figure B.3 Calculated velocity using yaw constants which give the minimum sum of squared residuals.

the range $25^\circ \leq \alpha \leq 65^\circ$. Since k does not change, it was only necessary to determine its value during the first calibration.

Once k , A , B and C are known, each sensor voltage pair is converted to U and V velocity components by firstly obtaining the effective cooling velocity of each sensor from equation B.1. The effective velocities are related to U and V by:

$$(U_{e1})^2 = P_1(U^2 + V^2) + Q_1UV \quad (B.4)$$

and
$$(U_{e2})^2 = P_2(U^2 + V^2) + Q_2UV \quad (B.5)$$

where
$$P_1 = \frac{1}{2}(1 + (k_1)^2) \quad (B.6)$$

$$Q_1 = 1 - (k_1)^2 \quad (B.7)$$

$$P_2 = \frac{1}{2}(1 + (k_2)^2) \quad (B.8)$$

and
$$Q_2 = -(1 - (k_2)^2) \quad (B.9)$$

Equations B.4 and B.5 are solved simultaneously to get U and V :

$$U = \left(\frac{-Y + \sqrt{Y^2 - 4X^2}}{2C} \right)^{1/2} \quad (B.10)$$

and
$$V = \frac{X}{CU} \quad (B.11)$$

where
$$X = P_2(U_{e1})^2 - P_1(U_{e2})^2 \quad (B.12)$$

$$Y = Q_2(U_{e1})^2 - Q_1(U_{e2})^2 \quad (B.13)$$

and
$$C = P_2 Q_1 - P_1 Q_2 \quad (B.14)$$

B.3 Look-up table calibration method

Before the decision was made to use the yaw factor method to calibrate the hot-film probe in this experiment, the look-up table calibration method was also evaluated. This method was proposed by Lueptow et al. (1988).

In this method, the probe was pitched at the seven angles at each of the seven calibration velocities so that a set of calibration data consisting of the sensor voltage pairs and their corresponding velocity/angle pairs was generated. The look-up table was generated by the following three steps:

- 1) Cubic spline or polynomial regression fits along each pitch angle α were used to find sensor voltage E_2 and the calibration velocity U_{calib} each as functions of E_1 . This provided the functions $E_2(E_1)|_{\alpha}$ and $U_{\text{calib}}(E_1)|_{\alpha}$.
- 2) The spline or polynomial fits determined in (1) were used to evaluate E_2 and U_{calib} for each angle α at regular intervals of E_1 . From these values, spline or polynomial fits were used to obtain functions of $\alpha(E_2)|_{E_1}$ and $U_{\text{calib}}(E_2)|_{E_1}$.
- 3) The spline or polynomial fits determined in (2) were used to evaluate α and U_{calib} for each interval of E_1 at regular

intervals of E_2 . This last step results in each (E_1, E_2) pair corresponding to a unique $(U_{\text{calib}}, \alpha)$ pair.

The U and V velocity components were then obtained from $U = U_{\text{calib}} \cos \alpha$ and $V = U_{\text{calib}} \sin \alpha$.

With this method a direct one-to-one conversion was achieved without having to make assumptions with respect to King's law constants or correction factors. However, this method required much more time than the yaw factor method, and was not significantly better in improving the uv correlation coefficient.

APPENDIX C

DETERMINATION OF MINIMUM LDV DATA RATE

In order to resolve the ejection structure and to achieve an essentially continuous time history, a data rate was needed such that the time between data (TBD) measurements was much smaller than the duration of the ejection. Coughran (1988) measured a mean duration of about $9 t^+$ at $y^+ = 30$ for $1200 \leq Re_\theta \leq 2900$. A maximum TBD of $t^+ = 1$ was considered to be adequate to resolve the ejection structure and to provide a continuous time history in this study.

The distribution of the TBD's approaches an exponential distribution, as shown in Figure C.1. The mean TBD necessary for 99% of all TBD's to be less than $1 t^+$ may be determined from the cumulative exponential distribution function:

$$F(t^+ = 1) = 1 - e^{-1/\mu} \quad (C.1)$$

where μ is the mean. For $F(t^+ = 1) = 0.99$, the mean is $0.217 t^+$ which is equal to 3 ms for the conditions of the experiment. This gives a mean data rate of 330/s. The theoretical maximum data rate attainable, assuming that the LDV system has been optimally aligned and set-up, is established by the volume flowrate through the LDV probe volume

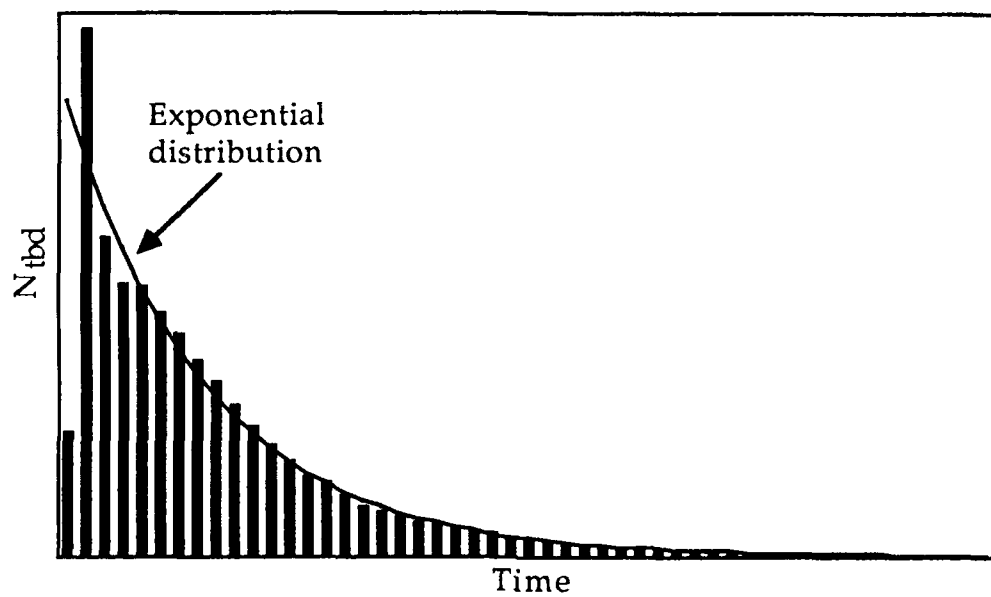


Figure C.1 Distribution of time between data measurements of LDV.

and ideally having one seed particle in the probe volume at any one time. At $y^+ = 10$, the maximum data rate was estimated to be about 1300/s, and about 2400/s at $y^+ = 80$.

In practice, however, it is impossible to get one seed particle in the probe volume at any one time. With the signal processors operated independently of each other (random mode), the maximum data rate attainable was about 1000/s near the wall. In this experiment, three-component velocity measurements were required, and this entailed operating the signal processors in coincidence mode, which means that a measurement is valid only if the same seed particle is in all three component probe volumes within a specified "coincidence" time window. This further reduced the data rate because of the criterion for coincidence.

At $y^+ = 10$, the maximum mean data rate which could be attained in coincidence mode was 300/s. Further away from the wall, the maximum mean data rate was 400/s. Near the wall, since the local mean velocity is lower than that further away, the volume flowrate through the probe volume is lower and thus results in a lower data rate. Furthermore, the probe volume was physically very close to the wall and there was a problem with flare which made the signal noisier. Consequently, the signal processors had to be operated at a lower gain setting. With the lower data rate, the mean TBD was $0.25 t^+$ and 98.5% of all TBD's were estimated to be less than $1 t^+$ using equation C.1.

APPENDIX D

CHARACTERISTICS OF THE FLOW FIELD AT DIFFERENT CONVECTION VELOCITIES

As mentioned in Section 3.2.3, an observer following the burst can reasonably be expected to only follow the structure at one convection velocity. To see the effect the convection velocity has on the velocity vector representation of the flow field, u_c - v velocity vectors in the x - y plane were plotted using several different convection velocities. Figure D.1(a)-(b) shows the u_c - v velocity vectors using the different convection velocities in the x - y plane at $z^+ = 5$, which is the plane passing through the burst detection point.

It can be noted from these vector plots that although the magnitudes of the vectors change, the overall structure of the burst does not qualitatively change significantly. The streamwise extent changes since the x^+ values were obtained from the convection velocity and the time. From these plots, it appears that the characteristics of the burst deduced from the vector plots in the x - y plane are not very sensitive to the convection velocity used.

Figure D.2(a)-(b) shows the u_c - w velocity vectors in the x - z plane at $y^+ = 20$, which is below the detection point. These plots show that

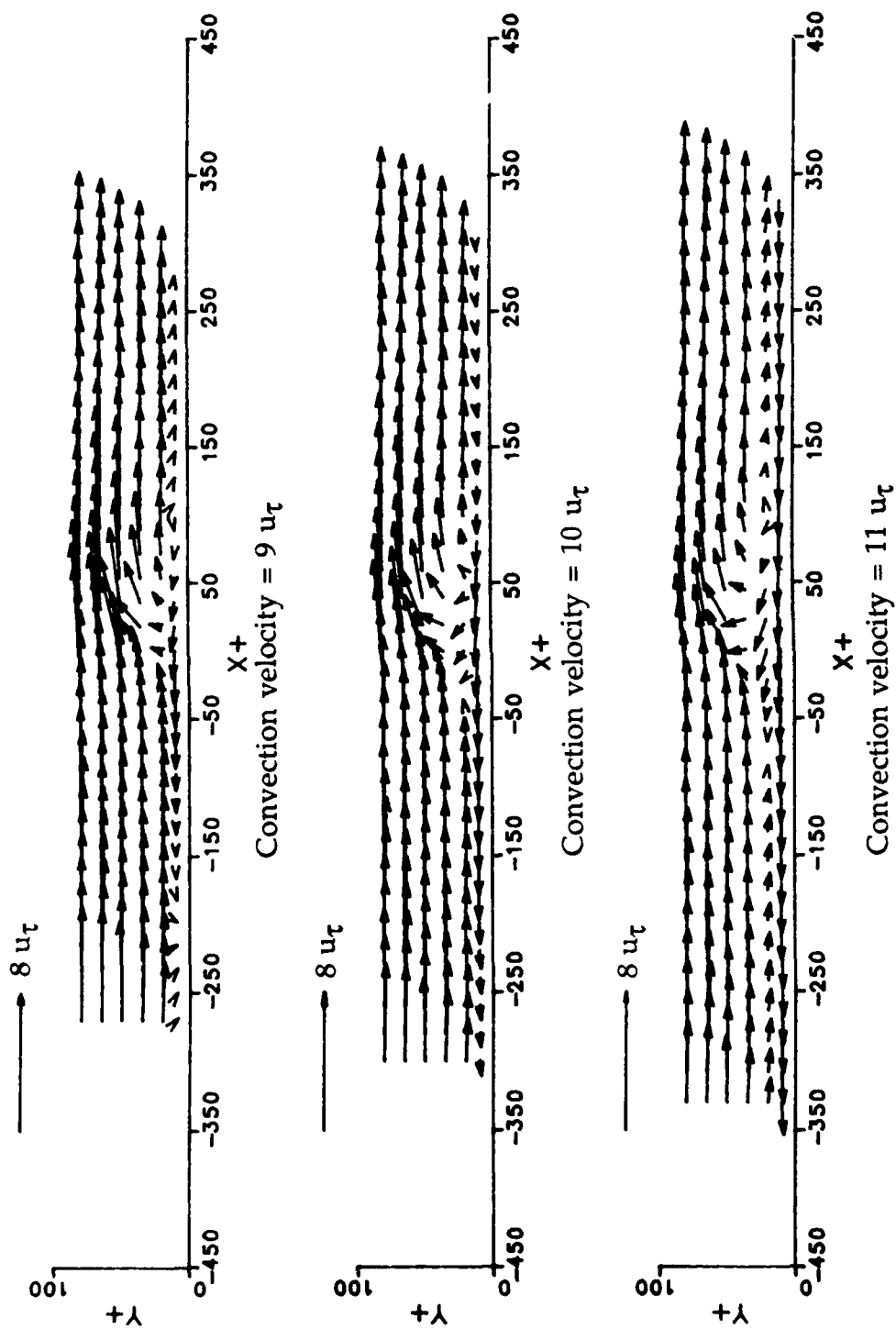


Figure D.1(a) $u_c - v$ velocity vectors in the $x-y$ plane at $z^+ = 5$ at different convection velocities.

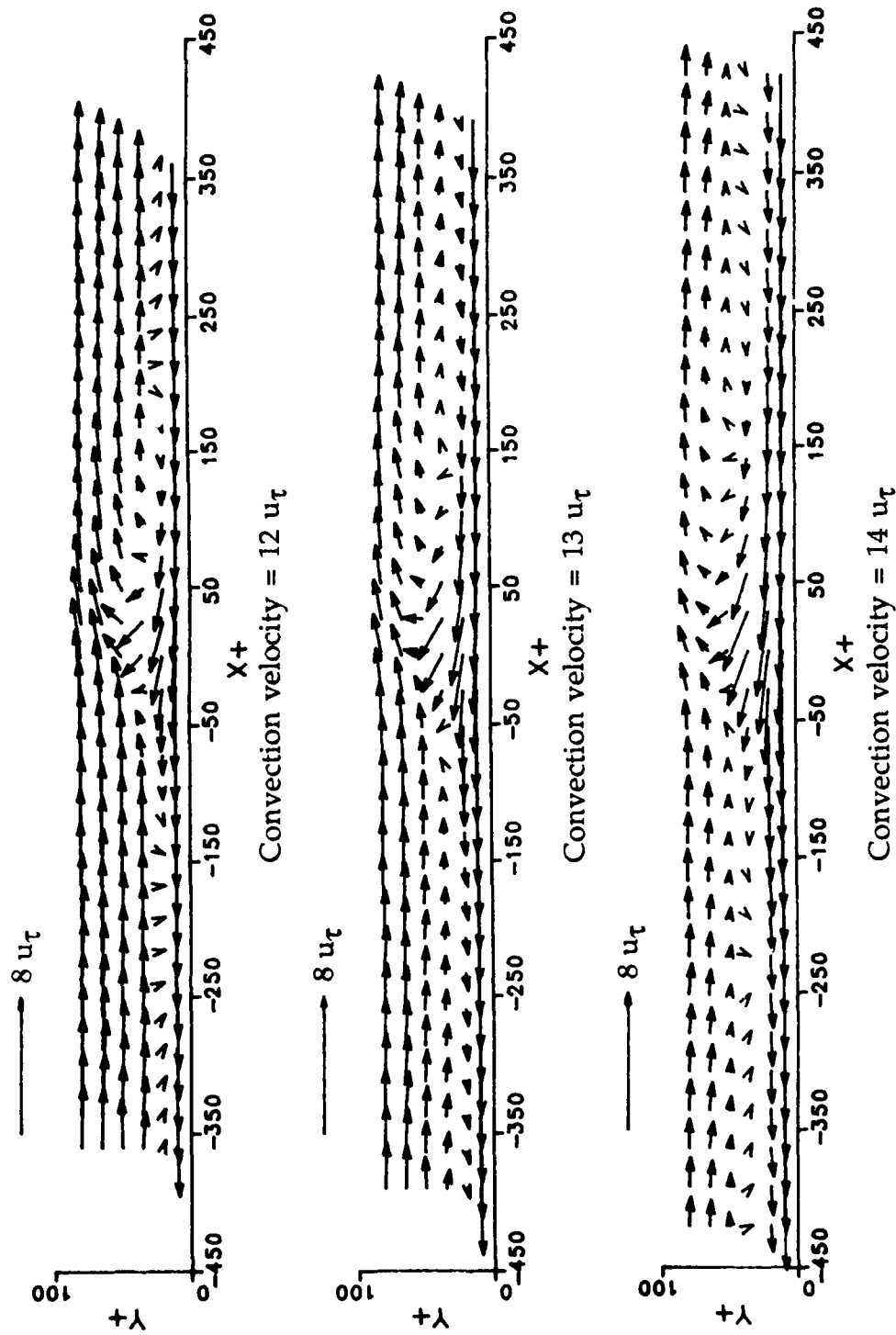


Figure D.1(b) $u_c - v$ velocity vectors in the $x-y$ plane at $z^+ = 5$ at different convection velocities.

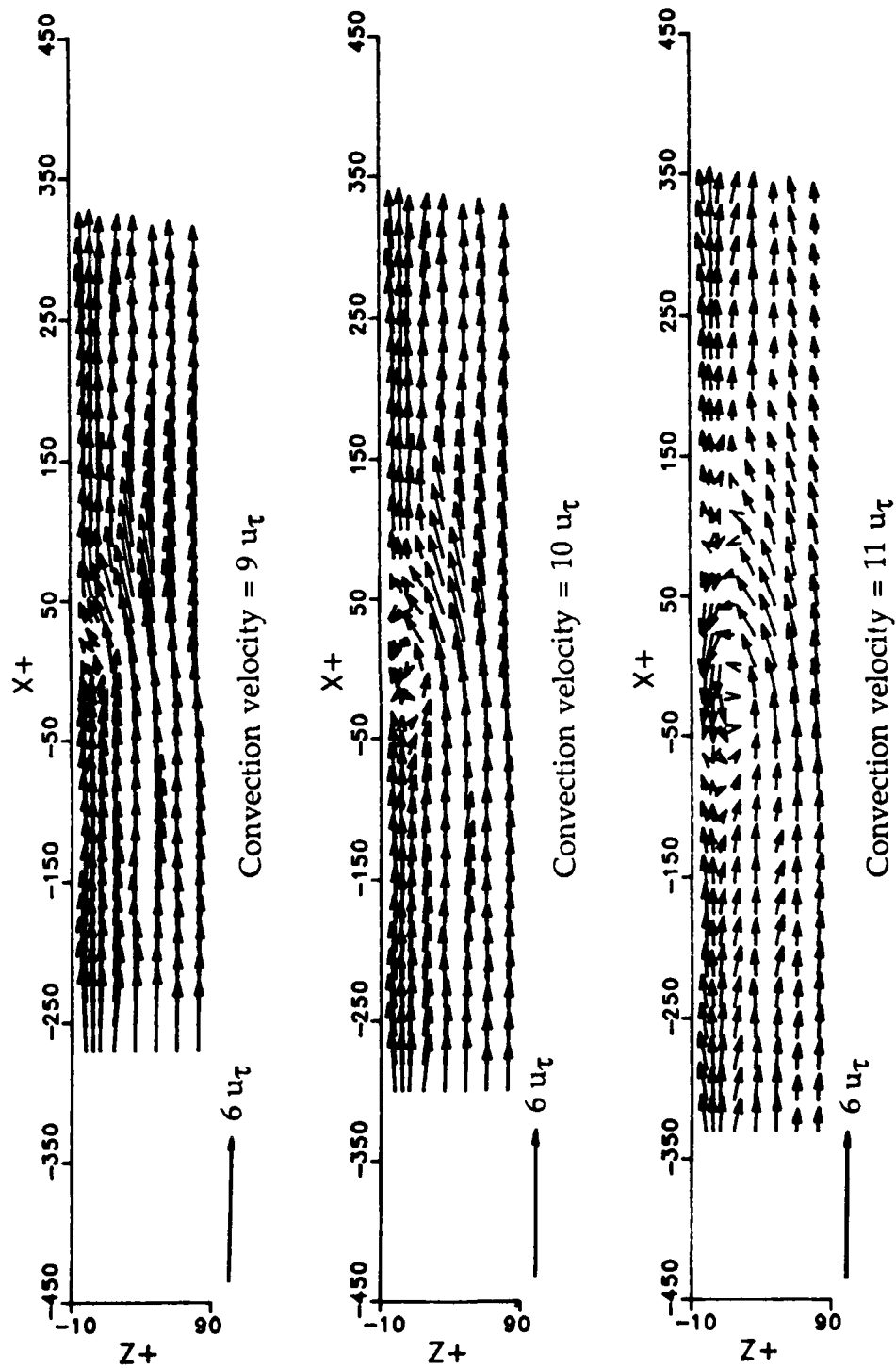


Figure D.2(a) $u_c - w$ velocity vectors in the $x-z$ plane at $y^+ = 20$ at different convection velocities.

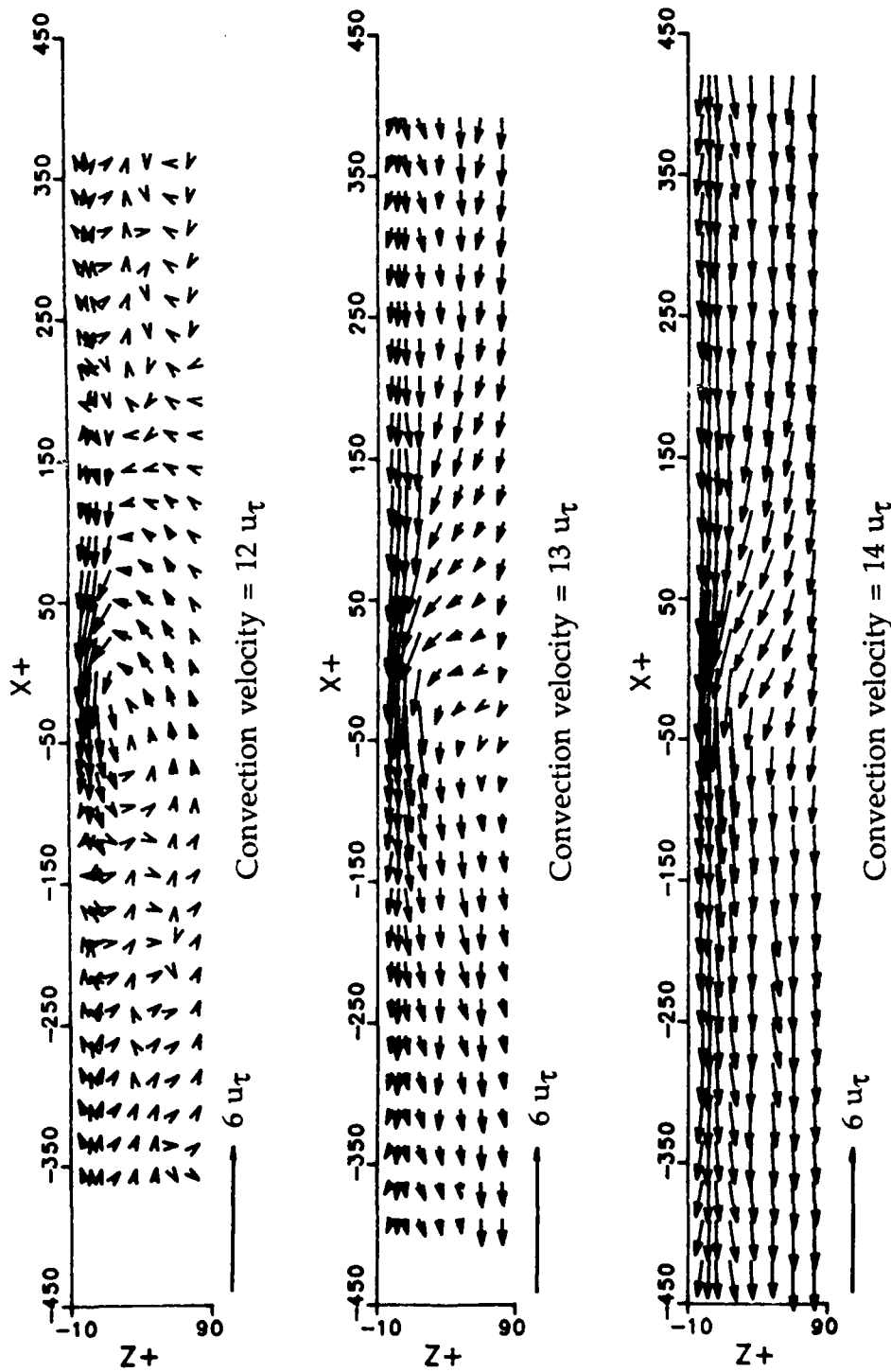


Figure D.2(b) $u_c - w$ velocity vectors in the x - z plane at $y^+ = 20$ at different convection velocities.

the characteristics of the structure change significantly with the convection velocity used. At the two lowest convection velocities of $9 u_\tau$ and $10 u_\tau$, the vectors show high speed fluid flowing around a region of low speed fluid. The center of the low speed region is essentially at zero velocity, indicating that the low speed region is moving at the convection velocity. Just downstream of the low speed region, the vectors show high speed fluid curving around the back of the low speed region.

At the convection velocity of $11 u_\tau$, which is the velocity determined by the area integration, the vectors show a vortical structure with the center close to zero velocity indicating that the vortical structure is moving at the convection velocity. The vortical structure is also evident when viewing the flow field at the local mean velocity of $12 u_\tau$. At the two highest convection velocities of $13 u_\tau$ and $14 u_\tau$ the vectors show a backrush of fluid indicating the convection velocities are faster than any structure in the flow.

Figure D.3 shows the u_c - w velocity vectors in the x - z plane at $y^+ = 35$, which is above the detection point. As at $y^+ = 20$, the characteristics of the structure shown by the vector plots depend on the convection velocity. The vortical structure can be seen at the convection velocities of $13 u_\tau$ and $14 u_\tau$, the latter being the local mean velocity.

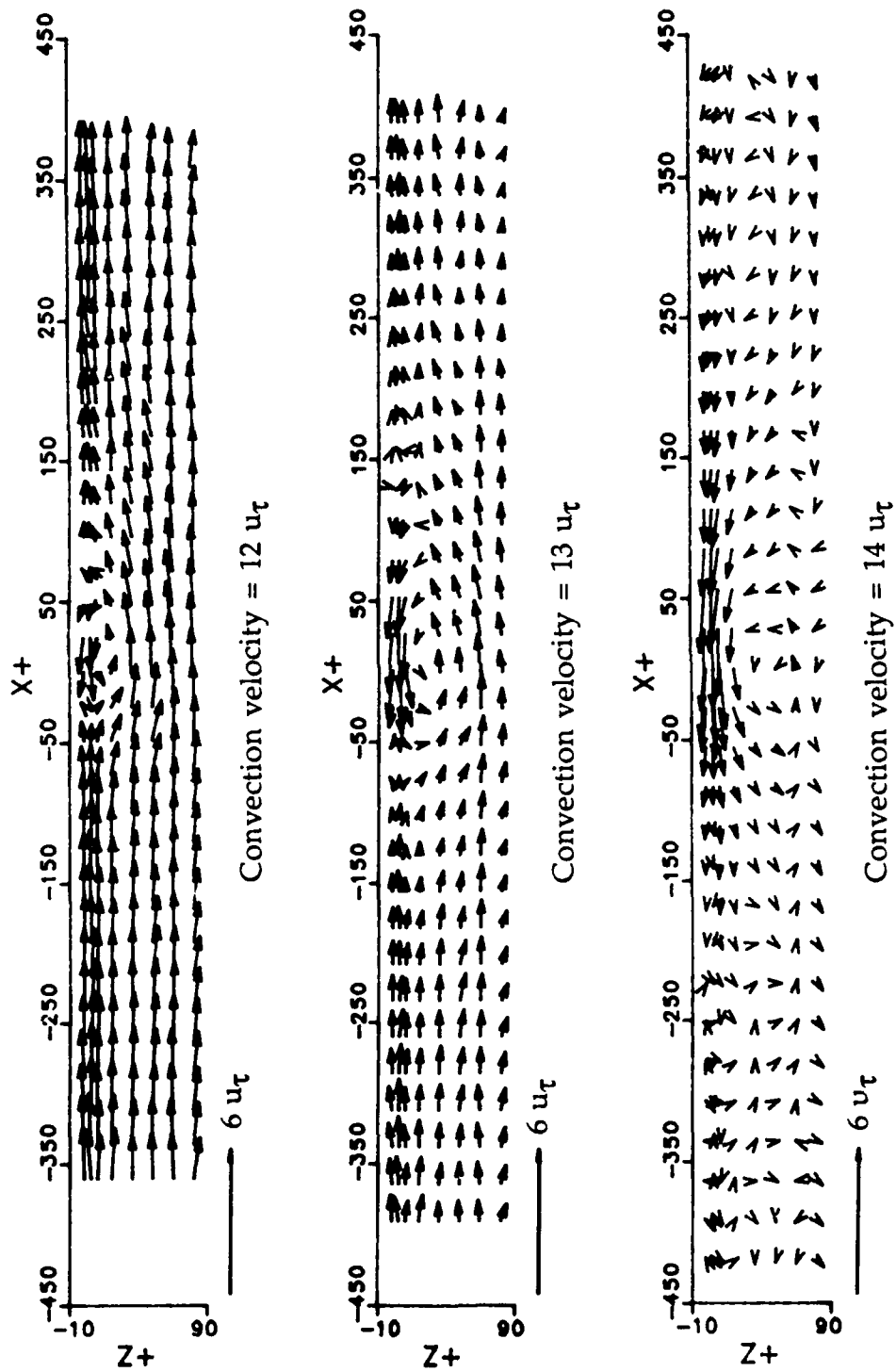


Figure D.3 $u_c - w$ velocity vectors in the $x-z$ plane at $y^+ = 35$ at different convection velocities.

APPENDIX E

UNCERTAINTY ANALYSIS

In this appendix, the uncertainties in the velocity measurements made by both the LDV and hot-film, as well as the uncertainties of the ensemble averaged conditional samples are estimated.

The Central Limit Theorem (Barnes, 1988) states that if a variable x is distributed with mean μ and standard deviation σ , then the sample mean x_m obtained from a random sample of size n will have a distribution that approaches a Normal distribution N :

$$x_m \rightarrow N(\mu, \frac{\sigma}{\sqrt{n}}) \quad \text{as } n \rightarrow \infty \quad (\text{E.1})$$

The uncertainty of x_m is taken as $\frac{2\sigma}{\sqrt{n}}$ which gives a 95% confidence interval. The percentage uncertainty is then:

$$\frac{\delta x_m}{x_m} = \frac{2\sigma}{x_m \sqrt{n}} \quad (\text{E.2})$$

E.1 LDV velocity measurements

The velocity is obtained from the expression:

$$v = d_f f_s \quad (E.3)$$

where d_f is the fringe spacing in the probe volume and f_s is the signal frequency. The calculation of fringe spacing depends on the measurement of the laser beam angle which was discussed in Appendix A. For small angles of ψ , the percentage change in $\sin\psi$ is approximately the same as the percentage change in ψ . Thus, the uncertainty of d_f corresponds directly with the uncertainty in ψ . Using equation E.2, the precision uncertainty for the TSI LDV system was

$\left(\frac{\delta d_f}{d_f}\right)_p = 0.28\%$, and for the FOLDV $\left(\frac{\delta d_f}{d_f}\right)_p = 0.55\%$. Because the wall of the water channel is not optically flat, a bias error due to the wall curvature is introduced. This bias error was estimated to be less than 1%. The total uncertainty of the fringe spacing, $\frac{\delta d_f}{d_f}$, is obtained from the Pythagorean summation of the individual uncertainties and is $\pm 1.1\%$.

The precision uncertainty in measuring the signal frequency was estimated to be 1.1%, using the procedure by Bogard & Gan (1987) for counter signal processors. The bias error on the signal frequency measurement was considered to be negligible. The total uncertainty of

the velocity measurement is obtained from the Pythagorean summation:

$$\frac{\delta v}{v} = \pm \sqrt{\left(\frac{\delta d_f}{d_f}\right)^2 + \left(\frac{\delta f_s}{f_s}\right)^2} \quad (\text{E.4})$$

Using equation E.4, the total uncertainty of the velocity measurements is $\pm 1.6\%$. The uncertainty was not affected by velocity biasing since the velocity measurements in this study were individual discrete measurements, and not statistical averages.

E.2 Hot-film velocity measurements

The uncertainty in the velocity measurements come from two main sources: the bias error from the calibration and the uncertainty in determining the yaw constant. Uncertainty from electronic noise was considered to be insignificant.

E.2.1 Bias error from the calibration

The calibration of the hot-film probe was discussed in Appendix B. It was determined that the deviation of the calculated velocity was not more than 2% from the calibration velocity. The bias errors in the U and V velocity measurements relative to the probe were determined from the calibration measurements at the various pitch angles.

Figure E.1 shows the variation in U and V over the range of pitch angles of the probe. The angle ϕ is the angle of the probe body to the mean flow direction. The bias errors of the U velocity are within 3%. Except for the one point at $\phi = -13^\circ$ where the error in V is 6%, the bias errors of V are also within 3%.

E.2.2 Uncertainty in U and V due to uncertainty of k

The procedure for determining the yaw constant k for each sensor was discussed in Appendix B. For each iteration, k was changed by steps of 0.02. This represents a percentage change of 10% based on the final value of k . The uncertainty in the "true" k value is taken as half the step change, or $\pm 5\%$.

The method of sequential perturbation was used to determine the uncertainty of U and V . In this method, a perturbed value of k and the corresponding perturbed values of A , B and C were put in to the equations for determining U and V . The uncertainties of U and V were taken as the change in U and V because of the change in k , and were found to be $\pm 0.03\%$ and $\pm 0.57\%$ respectively for the $\pm 5\%$ uncertainty in k .

Thus, the uncertainty in U and V due to the uncertainty in k is small compared to the bias errors from the calibration.

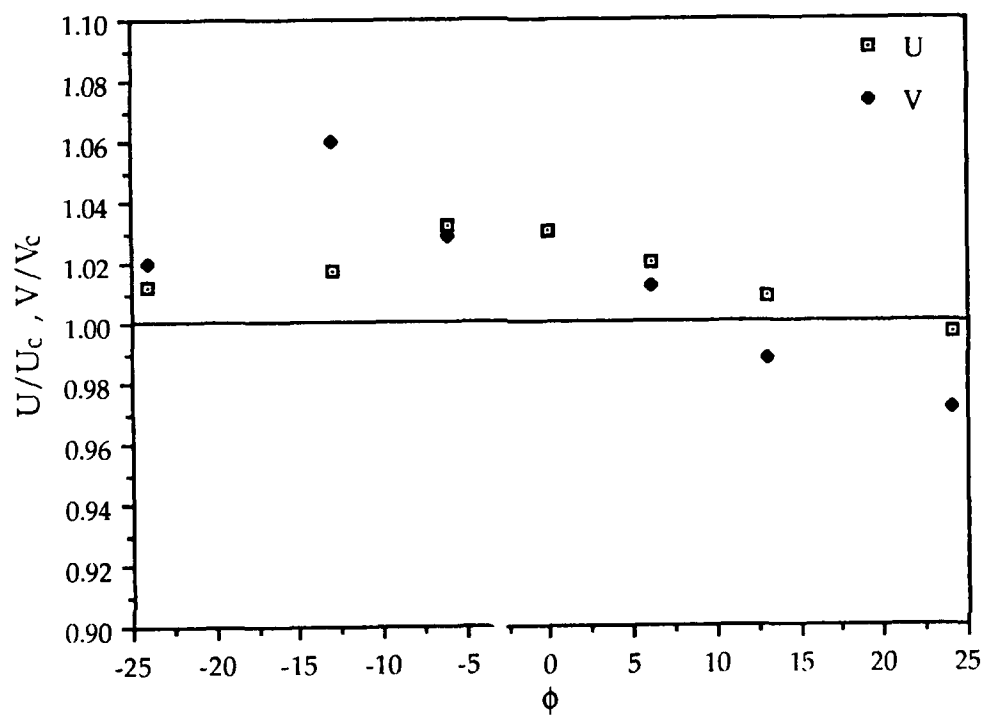


Figure E.1 Errors in U and V due to calibration.

E.3 Ensemble averaged conditional samples

The ensemble averaged conditional samples were based on an average of 200 events at the ejection detection threshold of $H \approx 1$, and 50 events at the higher threshold of $H = 4$. To determine if these sample sizes were large enough to give a representative ensemble average, variation of the peak values were investigated. This was done by comparing subsets of 50 and 100 samples to the ensemble average of 200 samples.

Figure E.2 shows the conditional samples at $(y^+, z^+) = (35, 5)$. Even with 50 samples, the ensemble averages are very similar to those with 200 samples. Table E.1 gives a tabulation of the peak values of the u , v , w and uv signals for the different sample sizes. In each case, the peak values of the 50 and 100-sample ensemble averages fall within the uncertainty bands of the 200-sample ensemble average.

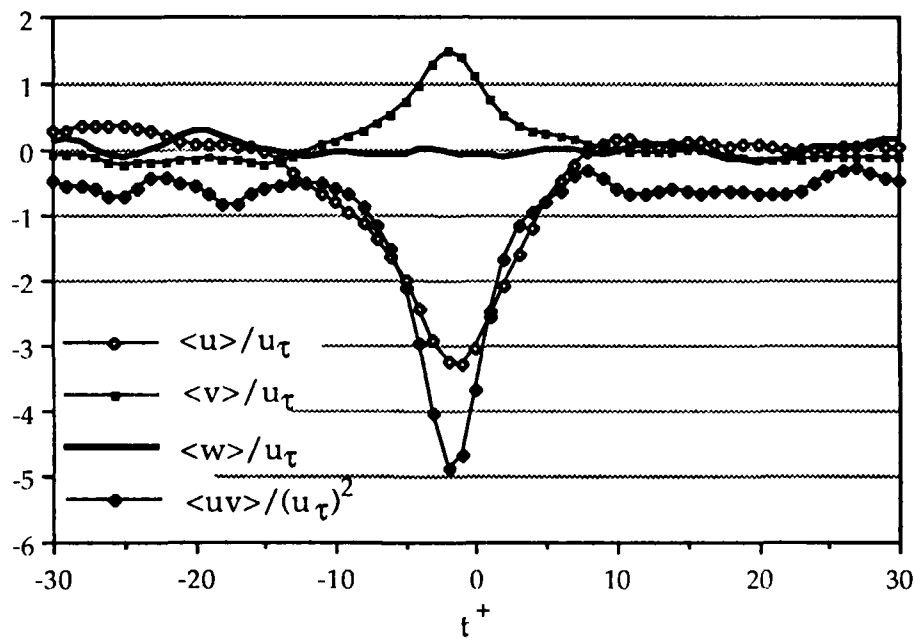
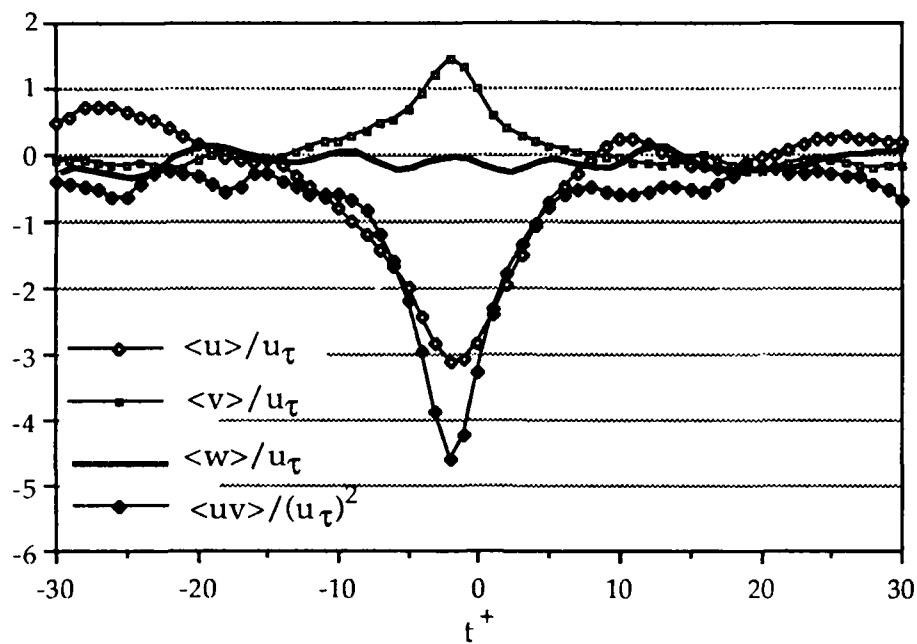
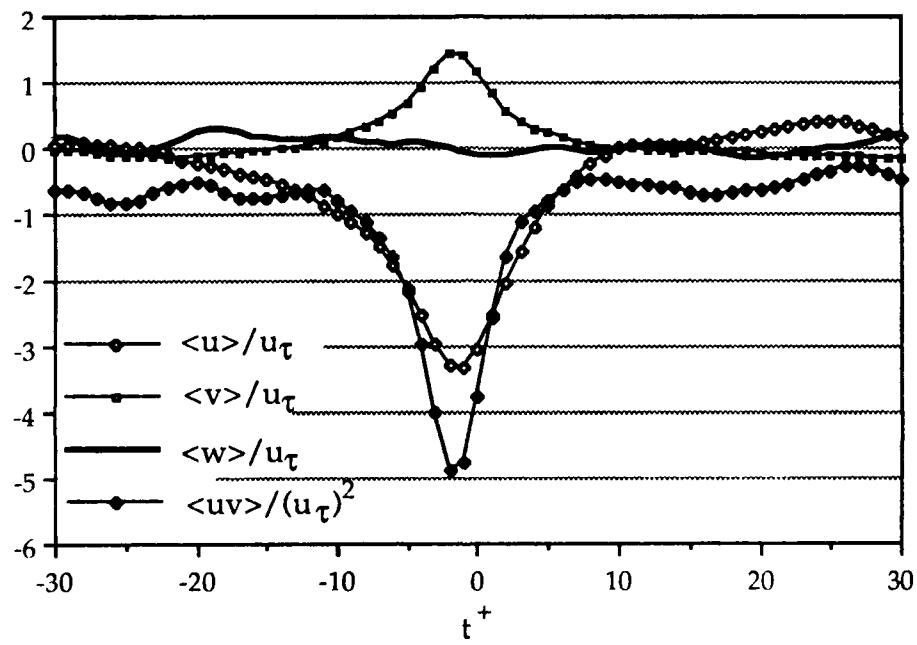


Figure E.2 Ensemble averages from (a) 50 samples, (b) 100 samples and (c) 200 samples.



(c) 200 sample ensemble average.

Sample size	200	100	50
Mean	-3.28	-3.22	-3.13
Rms	1.72		
Uncertainty	± 0.24		

(a) Ensemble averaged u/u_τ .

Sample size	200	100	50
Mean	1.43	1.47	1.42
Rms	0.64		
Uncertainty	0.09		

(b) Ensemble averaged v/u_τ .

Sample size	200	100	50
Mean	-0.01	0.04	-0.03
Rms	1.31		
Uncertainty	0.18		

(c) Ensemble averaged w/u_τ .

Sample size	200	100	50
Mean	-4.88	-4.60	-4.88
Rms	3.51		
Uncertainty	0.49		

(d) Ensemble averaged $uv/(u_\tau)^2$.Table E.1 Peak values of u , v , w and uv signals for different ensemble averaged conditional sample sizes.

NOMENCLATURE

C_f	Skin friction coefficient
H	Quadrant ejection detection threshold
k	Hot-film calibration yaw constant
Re_θ	Reynolds number based on momentum thickness
R_{uv}	Correlation coefficient of the uv product
t^+	Time normalized by inner scales v, u_τ
T_b	Time between bursts
T_e	Time between ejections
U, V, W	Absolute velocities in the streamwise, wall-normal and spanwise directions
u, v, w	Fluctuating velocities of U, V and W
u', v', w'	Rms velocities of U, V and W
u_∞	Freestream velocity
u_c	U minus the convection velocity
U_m	Local mean U velocity
u_τ	Shear velocity
$(uv)_2$	Second quadrant uv product ($u < 0, v > 0$)
$(uv)_4$	Fourth quadrant uv product ($u > 0, v < 0$)
x, y, z	Streamwise, wall-normal and spanwise coordinates
x^+, y^+, z^+	x, y, z coordinates normalized by inner scales v, u_τ

Greek symbols

δ	Boundary layer thickness (y distance where $U = 0.99 u_{\infty}$)
κ	von Karman constant
ν	Kinematic viscosity
θ	Momentum thickness
τ_{\max}	Cut-off time for grouping ejections into bursts

REFERENCES

- Bakewell, H.P. and Lumley, J.L. 1967 Viscous sublayer and adjacent wall region in turbulent pipe flow. *Phys. Fluids* 10 (9), 1880.
- Barlow, R.S. and Johnston, J.P. 1985 Structure of turbulent boundary layers on a concave surface. *Report MD-47 under contract AFOSR-F49620-84-K-0004*, Stanford University.
- Barnes, J.W. 1988 *Statistical Analysis for Engineers - A Computer-Based Approach*. Prentice Hall, New Jersey.
- Blackwelder, R.F. and Eckelmann, H. 1979 Streamwise vortices associated with the bursting phenomenon. *J. Fluid Mech.* 94, 577.
- Blanton, J.N. 1986 An experimental investigation of large eddy breakup devices in a water channel facility. *M.S. Thesis*, The University of Texas at Austin.
- Bogard, D.G. and Gan, C.L. 1987 An evaluation of the accuracy of an LDV counter. *Third International Symposium on Laser Anemometry*, Boston.
- Bogard, D.G. and Tiederman, W.G. 1986 Burst detection with single-point velocity measurements. *J. Fluid Mech.* 162, 389.
- Bogard, D.G. and Tiederman, W.G. 1987 Characteristics of ejections in turbulent channel flow. *J. Fluid Mech.* 179, 1.
- Coles, D.E. and Hirst, E.A. (Eds.) 1969 Computation of turbulent boundary layers. *Proc. 1968 AFOSR-IFP-Stanford Conference*, Stanford University.
- Comte-Bellot, G., Sabot, J. and Saleh, I. 1978 Detection of intermittent events maintaining Reynolds stress. *Proc. Dynamic Flow Conf. - Dynamic Measurements in Unsteady Flows*, p. 213, Marseille, France.

- Coughran, M.T. 1988 Interdependence of large and small scale structures in a turbulent boundary layer. *PhD Dissertation*, The University of Texas at Austin.
- Coughran, M.T. and Bogard, D.G. 1986 An experimental study of the burst structure in a LEBU-modified boundary layer. *Tenth Symposium on Turbulence*, Rolla, Missouri.
- Guezennec, Y., Piomelli, U. and Kim, J. 1987 Conditionally-averaged structures in wall-bounded turbulent flows. *Proc. Summer Program, Center for Turbulence Research, Stanford University/NASA Ames*.
- Johansson, A.V., Alfredsson, P.H. and Eckelmann, H. 1987 On the evolution of shear-layer structures in near-wall turbulence. *Advances in Turbulence - Proc. 1st. European Turbulence Conference*, p. 383, Springer-Verlag, Berlin.
- Johansson, A.V., Alfredsson, P.H. and Kim, J. 1987 Shear-layer structures in near-wall turbulence. *Proc. Summer Program, Center for Turbulence Research, Stanford University/NASA Ames*.
- Kasagi, N., Hirata, M. and Nishino, K. 1986 Streamwise pseudo-vortical structures and associated vorticity in the near-wall region of a wall-bounded turbulent shear flow. *Expt. Fluids* 4, 309.
- Kim, J. 1985 Turbulence structures associated with the bursting event. *Phys. Fluids* 28 (1), 52.
- Klebanoff, P. S. 1955 Characteristics of turbulence in a boundary layer with zero pressure gradient. *NACA Report* 1247.
- Kline, S. J., Reynolds, W. C., Schraub, F. A. and Runstadler, P. W. 1967 The structure of turbulent boundary layers. *J. Fluid Mech.* 30, 741.

- Komori, S., Murakami, Y. and Ueda, H. 1989 Detection of coherent structures associated with bursting events in an open-channel flow by a two-point measuring technique using two laser-Doppler velocimeters. *Phys. Fluids A* **1** (2), 339.
- Kreplin, H.P. and Eckelmann, H. 1979 Propagation of perturbations in the viscous sublayer and adjacent wall region. *J. Fluid Mech.* **95**, 305.
- Lee, M.K., Eckelman, L.D. and Hanratty, T.J. 1974 Identification of turbulent wall eddies through the phase relation of the components of the fluctuating velocity gradient. *J. Fluid Mech.* **66**, 17.
- Lu, S.S. and Willmarth, W.W. 1973 Measurements of the structure of the Reynolds stress in a turbulent boundary layer. *J. Fluid Mech.* **60**, 481.
- Luchik, T.S. and Tiederman, W.G. 1987 Timescale and structure of ejections and bursts in turbulent channel flows. *J. Fluid Mech.* **174**, 529.
- Lueptow, R.M., Breuer, K.S. and Haritonidis, J.H. 1988 Computer-aided calibration of X-probes using a look-up table. *Expt. Fluids* **6**, 115.
- Nagib, H.M. and Guezennec, Y.G. 1986 On the structure of turbulent boundary layers. *Tenth Symposium on Turbulence*, Rolla, Missouri.
- Nychas, S.G., Hershey, H.C. and Brodkey, R.S. 1973 A visual study of turbulent shear flow. *J. Fluid Mech.* **63** (3), 513.
- Praturi, A.K. and Brodkey, R.S. 1978 A stereoscopic visual study of coherent structures in turbulent shear flow. *J. Fluid Mech.* **89**, 251.
- Purtell, L.P., Klebanoff, P.S. and Buckley, F.T. 1981 Turbulent boundary layer at low Reynolds number. *Phys. Fluids* **24** (5), 802.

- Robinson, S.K., Kline, S.J. and Spalart, P.R. 1988 Quasi-coherent structures in the turbulent boundary layer: Part II. Verification and new information from numerically simulated flat-plate layer. *Zoran P. Zaric Memorial International Seminar on Near-wall Turbulence*, Dubrovnik, Yugoslavia.
- Smith, C. R. and Metzler, S.P. 1983 The characteristics of low-speed streaks in the near-wall region of a turbulent boundary layer. *J. Fluid Mech.* **129**, 27.
- Smith, C.R. and Schwartz, S.P. 1983 Observation of streamwise rotation in the near-wall region of a turbulent boundary layer. *Phys. Fluids* **26** (3), 641.
- Spalding, D.B. 1961 A single formula for the "law of the wall". *J. Appl. Mech.* **28** E(3), 455.
- Wallace, J.M., Eckelmann, H. and Brodkey, R.S. 1972 The wall region in turbulent shear flow. *J. Fluid Mech.* **54** (1), 39.
- Wark, C.E. 1988 Experimental investigation of coherent structures in turbulent boundary layers. *PhD Dissertation*, Illinois Institute of Technology.

INDEX OF REPORTS

1. Annual ONR Project Review, 1987
2. Summary Annual Report, 1987
3. Annual ONR Project Review, 1988
4. Summary Annual Report, 1988
5. Annual ONR Project Review, 1989
6. Summary Annual Report, 1989

INDEX OF PUBLICATIONS

1. Bogard, D.G. and Coughran, M.T. 1987 Bursts and ejections in a LEBU-modified boundary layer. *Sixth Symposium on Turbulent Shear Flows*, Toulouse, France.
2. Ciancarelli, C.R., Bogard, D.G. and Gan, C.L. 1988 Measurement precision of an LDV scanning system. *AIAA 26th Aerospace Sciences Meeting*, Reno, Nevada.
3. Ciancarelli, C.R. 1988 Development of a scanner and signal processing system for laser anemometry. *M.S. Thesis*, The University of Texas at Austin.
4. Coughran, M.T. 1988 Interdependence of large and small scale structures in a turbulent boundary layer. *PhD Dissertation*, The University of Texas at Austin.
5. Gan, C.L. 1989 The burst structure and its associated flow field in a turbulent boundary layer. *M.S. Thesis*, The University of Texas at Austin.

DISTRIBUTION LIST

Dr. Michael M. Reichman
Code 1132F
Office of Naval Research
800 North Quincy Street
Arlington, VA 22217

Director
Naval Research Laboratory
Attn: Code 2627
Washington, DC 20375
(6 copies)

Office of Naval Research
Resident Representative
Federal Building, Room 582
300 East 8th Street
Austin, TX 78701-3273

Defence Technical Information Center
Building 5, Cameron Station
Alexandria, VA 22314
(12 copies)

Professor Ronald F. Blackwelder
University of Southern California
Dept. of Aerospace Engineering
University Park
Los Angeles, CA 90089-1191

Dr. Steven K. Robinson
MS 163
NASA Langley Research Center
Hampton, VA 23665-5225

Professor Thomas J. Hanratty
Dept. of Chemical Engineering
1209 West California Street
Box C-3
Urbana, IL 61801

Professor William G. Tiederman
Purdue University
School of Mechanical Engineering
Mechanical Engineering Building
West Lafayette, IN 47907

Dr. Joseph H. Haritonidis
Room 37-461
Massachusetts Institute of Technology
Cambridge, MA 02139

Professor Steven J. Kline
Thermosciences Division
Dept. of Mechanical Engineering
Stanford University
Stanford, CA 94305